Politecnico di Torino

Corso di Laurea Automotive Engineering
A.a. 2022/2023
Sessione di Laurea Ottobre 2023

Development of Virtual Methodology to Evaluate Electric Motor Losses

Relatori:
Prof. Gianmario Pellegrino
Dott.ssa Ofelia A. Jianu
Dott. Narayan Kar
Supervisore aziendale Stellantis:
Ing. Raffaele Bonavolontà

Candidato:
Giovanni Ricciardi

Development of Virtual Methodology to Evaluate Electric Motor Losses

by

Giovanni Ricciardi

APPROVED BY:

B. Balasingam
Department of Electrical and Computer Engineering

G. Rankin
Department of Mechanical, Automotive & Materials Engineering

N. Kar, Advisor
Department of Electrical and Computer Engineering

O. Jianu, Advisor
Department of Mechanical, Automotive & Materials Engineering

August 9th 2023

DECLARATION OF ORIGINALITY

I hereby certify that I am the sole author of this thesis and that no part of this thesis has been published or submitted for publication.

I certify that, to the best of my knowledge, my thesis does not infringe upon anyone's copyright nor violate any proprietary rights and that any ideas, techniques, quotations, or any other material from the work of other people included in my thesis, published or otherwise, are fully acknowledged in accordance with the standard referencing practices. Furthermore, to the extent that I have included copyrighted material that surpasses the bounds of fair dealing within the meaning of the Canada Copyright Act, I certify that I have obtained a written permission from the copyright owner(s) to include such material(s) in my thesis and have included copies of such copyright clearances to my appendix.

I declare that this is a true copy of my thesis, including any final revisions, as approved by my thesis committee and the Graduate Studies office, and that this thesis has not been submitted for a higher degree to any other University or Institution.

ABSTRACT

Electric motors represent one of the most efficient and performant devices to convert electrochemical energy into mechanical energy. The permanent magnet synchronous machines (PMSMs) are the most commonly employed solutions for electric propulsion in the automotive field, thanks to their high torque capability and high efficiency, compared to other solutions as the induction machines. Nevertheless, reducing the losses in electric motors is one of the major targets in the automotive industry and to model them, the major tool employed is finite element analysis (FEA). The scope of this research activity is to accurately model and predict the electric motor losses and efficiency, exploiting the case study of the internal permanent magnet employed in the Fiat 500 battery electric vehicle (BEV). An estimation method is provided for each of the motor losses, namely joule, core and mechanical losses, prior to running the simulations. The motor is implemented into two software environments and its behavior simulated.

The outcomes of the simulation are provided to a code developed in MATLAB™ to assess the losses and the efficiency for each operative point and then allocate the results into maps. Afterwards, the simulation results are compared to the experimental behavior.

Lastly, some considerations about the motor model implementation, loss models development and efficiency map evaluation are presented.

To my grandparents, my family and all my beloved ones.

ACKNOWLEDGEMENTS

Foremost, I would like to express my deepest gratitude to my advisors Dr. Jianu, Dr. Kar, and Dr. Pellegrino for their unwavering motivation, enthusiasm, and continuous support throughout this research activity. Their invaluable knowledge in the field has been fundamental to the development of this thesis. Additionally, I want to thank Dr. Kar for welcoming me into his CHARGE lab, where I have gained invaluable experiences and knowledge over the year.

Besides my advisors, I would like to thank the rest of my thesis committee, Dr. Rankin and Dr. Balasingam for the suggestions and very usefull insight comments.

My sincere thanks go to Ms. Marie Mills for offering me the incredible opportunity to be involved in a project with Stellantis. I am deeply grateful to Eng. Raffaele Bonavolontà and Eng. Pradeep Attibele for their continuous support. Their dedication and technical expertise have played a crucial role in this research.

Furthermore, I would like to extend my heartfelt thanks to Prof. Maria Pia Cavatorta, DIMD program coordinator, for granting me the chance to participate in this project and take part to this amazing experience in North America. It has been a pivotal journey for my personal and professional growth.

I am deeply grateful to my family. Mom and dad, thank you for always being there and supporting me in every decision I make. To my brother, thank you for believing in me. A special thank you goes to my sister Rosalba, for her advices throughout my years of study and for being the wonderful person she is.

To my girlfriend Marialucia, you are truly special to me. Thank you for standing by my side, no matter what. You have always been close to me throughout this year, despite the distance.

I would like to thank Natalia, Luca, Mike, Matteo, Daniele, Gaetano and all the amazing people I have had the pleasure of meeting during this experience. I am also grateful to all the members of the CHARGE lab, both from a technical and personal standpoint. Lastly, to all my friends from Italy, which have always been there, even though the distance. You all are amazing people and I wish you the best.

TABLE OF CONTENTS

LIST OF TABLES

LIST OF FIGURES

NOMENCLATURE

A	Magnetic vector potential
A_1	Stator resistance model quadratic term coefficient
α	Hysteresis loss exponent
α_3	Core loss corrective coefficient for material saturation
α_4	Core loss corrective exponent for material saturation
α_e	Coefficient of thermal expansion
β	Peak magnetic induction
b	Conductor's width
b-emf	Back electromotive force
BEV	Battery electric vehicle
$2D$	Bidimensional
$3D$	Tridimensional
C_1	Stator resistance model constant term coefficient
CFD	Computation fluid dynamics
D_b	Bore diameter of the bearing
d	Lamination thickness
d_c	Cut-edge deformation depth
d_{eq}	Equivalent cut depth
E	Electric field
η_{mot}	Experimental motor efficiency
$\eta_{mot,sim}$	Simulated motor efficiency
F_b	Equivalent dynamic bearing load
FEA	Finite element analysis
G	Proximity effect factor for rectangular conductors
γ	Eddy current loss exponent
γ_{lam}	Material lamination factor

h	Conductor's height
H_c	Coercivity of the permanent magnets
H_e	Peak value of the magnetic field
i_a	Phase a current
i_b	Phase b current
i_c	Phase c current
i_α	α component of the stator winding current in $\alpha\beta$ reference frame
i_β	β component of the stator winding current in $\alpha\beta$ reference frame
IPM	Internal permanent magnet
$IPMSM$	Internal permanent magnet synchronous machine
J_{mot}	Motor inertia
K_1	Core loss model linear term coefficient
K_1	Coefficient of thermal expansion
K_2	Core loss model quadratic term coefficient
K_{AC}	AC effect corrective factor
K_c	Eddy current loss coefficient
K_e	Experimental back electromotive force coefficient
$K_{e\_simulation}$	Simulated back electromotive force coefficient
K_h	Excess loss coefficient
K_h	Hysteresis loss coefficient
K'_r	Corrected average resistance increase
l_i	Slot's length
l_s	End winding's length
M_{UT}	Motor under test
MUT	Motor under test
N_n	Number of conductors per slot
ω	Angular speed
P_{AC}	Alternate current ohmic loss
P_{class}	Classical eddy current loss
P_{core}	Core losses
P_{DC}	Direct current ohmic loss
$P_{experimental}$	Experimental loss
P_{exc}	Excess loss
P_{input}	Input power

$P_{input,sim}$	Simulated input power
$P_{L,co}$	Copper power loss
$P_{L,iron}$	Iron power loss
$P_{L,total}$	Total power loss
P_{mech}	Mechanical losses
P_{model}	Modeled loss
P_{output}	Output power
$P_{output,avg}$	Average output power
$P_{output,sim}$	Simulated output power
$P_{RMS\_simulation}$	Simulated RMS value of the voltage
P_{total}	Total power loss
pu	Per unit
R	Resistance
R_0	Resistance at a reference temperature
R_{stator}	Stator resistance
$R_{stator,avg}$	Average stator resistance
RE	Rare-earth
SiFe	Iron Silicate
SPM	Superficial permanent magnet
T	Time
T_{EM}	Electromagnetic torque
$T_{m,avg}$	Average electromagnetic torque
T_{mot}	Torque
$T_{mot,avg}$	Average torque
$T_{output,sim}$	Simulated output torque
T_R	Resistance torque
θ	Second order derivative of the angle swept by the motor
V	Electric potential
$V_{ll,rms}$	Line to line RMS motor voltage
$V_{LL\_RMS\_experimental}$	Line to line experimental RMS value of the voltage
$V_{LL\_RMS\_simulation}$	Line to line simulated RMS value of the voltage
$V_{RMS\_simulation}$	Simulated RMS value of the voltage
V_T	Terminal voltage
V_α	α component of the stator winding voltage in α - β reference frame
V_β	β component of the stator winding voltage in α - β reference frame
ω	Angular speed

Chapter 1

Introduction

In recent years, the global energy crisis and environmental challenges have led governments and industries to seek more efficient solutions for converting chemical or electrochemical energy into mechanical motion. Among the various alternatives available, electric motors represent a category of considerable interest and prospects, given their widespread use in the industrial sector and many other criteria including high efficiency, high torque and acceleration capability. Electric motors operate based on the principles of electromagnetism, utilizing the interaction of winding currents and magnetic fields. PMSMs are widely employed in electric vehicles due to their remarkable features. These motors utilize permanent magnets to generate a magnetic field without the need for an external energy source. This inherent ability, combined with their reduced losses, positions PMSMs as one of the most favored solutions for electric vehicle propulsion.

Despite their high efficiency over a wide range of torque and speed, electric motors are still influenced by losses, which impact their performance. Various strategies exist to minimize motor losses and enhance efficiency, including size reduction, different stator winding configurations, and the implementation of cooling systems to maintain performance without sacrificing efficiency. Implementing and testing motor layout changes, as changing the stator windings configuration, on physical electric machines would be a time-consuming and costly endeavor.

To address this challenge, virtual models are commonly used to analyze the performance of electric motors in a simulated environment. Modeling of an electric motor involves multiple engineering domains, from the electro-magnetic, to the thermal and structural analysis. FEA is a widely used tool for evaluating losses during the design phase, allowing for layout modifications and analysis of their effects. The time-domain FEA approach offers greater simulation accuracy by capturing temporal and spatial harmonics and small geometric details, although it comes with a tradeoff of increased simulation time compared to static solutions.

The target of this research activity is to develop an accurate virtual model to predict the iron, Joule and mechanical losses for an interior permanent magnet synchronous motor (IPMSM) provided by Stellantis and at the moment employed in the FIAT 500 battery electric vehicle. By exploiting the two finite element analysis software Altair Flux™ and ANSYS Maxwell™ it is possible to simulate the motor performance and analyze its efficiency-reducing factors.

To replicate an experimental efficiency map, a comprehensive evaluation of losses is conducted at various torque/speed points. Iron loss, torque, and current data are collected from the software environment. A post-processing code, developed in MATLAB™, is then utilized to calculate the Joule and mechanical losses, enabling the creation of efficiency, loss and error maps. Additionally, loss maps and the percentage distribution of each loss at each operating point are generated.

The developed method aims to create an adaptable code that can accurately predict losses in various types of electric motors, given that all the necessary input data is available. This approach allows for the construction of a virtual model that closely represents the actual behavior of the motor. By incorporating more reliable data into the design stage, the motor can be optimized to achieve the desired performance and efficiency targets.

1.1 Objectives

The objectives of this project can be distinguished between research and company side. From the research perspective, these are listed below:

- Achieving a high-fidelity replication of the motor model.
- Developing a method to simulate and predict the electric motor losses.

On the other hand, the major targets for the company are:

- Investigating the potentialities of both the software in terms of virtual modeling and electromagnetic simulation.
- Performance comparison between the two software, in terms of accuracy in the results, operability and modularity.

1.2 Overview

The following chapters delve into the details of the electric motor losses and their modeling, the electric motor model implementation in the two software environments and the analysis of the simulation results. The first chapter is dedicated to the introduction of this work. The following one entitled literature review, offers a comprehensive analysis of the PMSM electric motors and the electric motor losses. It provides a clear insight of each of the losses, also accounting for the manufacturing and temperature effects, before describing the most common approach to model these in a virtual environment. Afterwards, the efficiency map evaluation, both experimentally and virtually, is presented. Chapter three illustrates the methodology, i.e. the overall procedure to develop the motor loss models and run the simulations with the two software tools. Each stage, from the implementation of the motor model to the post processing of the simulation results in MATLAB™, are treated. The outcomes of the simulations, more specifically of the back electromotive test and of the steady state performance test are reported in the 'Simulation Results' chapter. These are expressed in terms of loss maps and efficiency maps, for each of the two software. Chapter five is reserved to the analysis of the results. It includes the loss evaluation and comparison between different operating conditions and the error maps. Last, the 'Conclusions and Future Work' chapter will sum up the main findings of this research activity and the possible continuation of this research activity.

Chapter 2

Literature review

2.1 Background of Electric Motors

Electric motors are devices that convert electrical energy into mechanical energy. They play a crucial role in various applications, ranging from industrial machinery and transportation systems to household appliances and electronics. Electric motors operate based on the principles of electromagnetism, utilizing the interaction between electric current and magnetic fields to generate rotational motion.

Electric motors offer numerous advantages over other forms of power generation and mechanical systems. They are highly efficient, converting a large portion of electrical energy into mechanical power. They are also capable of delivering high torque and are relatively compact in size. Additionally, electric motors provide precise control over speed and direction, making them versatile and adaptable for various tasks [1].

There are various types of electric motors, each designed for specific applications and operating conditions. When it comes to vehicle traction, alternate current (AC) machines are the preferred technology [2]. These motors are powered by alternating current to provide propulsion. AC drives can be classified as asynchronous and synchronous machines. Induction motors, which belongs to the first of these two categories, are widely used in industrial settings due to their simplicity, reliability, and cost-effectiveness. On the other hand, synchronous motors, as permanent magnets machines, are commonly employed in applications requiring precise speed control [3].

2.1.1 Permanent Magnet Synchronous Machines

Permanent magnet synchronous machines are a type of electric motors that utilizes permanent magnets in the rotor instead of electromagnets. These motors offer several advantages over other motor types, including high efficiency, compact size, and improved power-to-weight ratio. It is widely known that employing permanent magnets allows to achieve high constant torque capability, remarkable constant power capability and most importantly high efficiency [4]. Indeed, permanent magnets have the unique feature of delivering magnetic flux into the airgap without any continuous expenditure of energy. Furthermore, they are not affected by a reverse magnetic field acting in their same operational region and are capable of maintaining their field under different operating temperatures, if extreme conditions are not reached. If the opponent magnetic field is strong enough, a magnet can be demagnetized, which means that its magnetic domains will be re-oriented. On the other hand, if the Curie point is reached, the magnet would completely lose its magnetic properties. For the electric motors employed in automotive applications, it is reasonable to neglect these scenarios, since the operating temperature is much lower than the average Curie point and the small entity of the magnetic counter fields [5].

When it comes to PMSM, two categories can be identified: interior permanent magnet and surface permanent magnet (SPM) motors. The distinction between these two types lies in the placement and configuration of the permanent magnets within the motor's rotor. This distinction significantly affects the motor's performance characteristics, efficiency, and suitability for different applications. According to the findings presented by Pellegrino et al. [4] in their research paper, IPM electric motors exhibit excellent overload capability across the entire speed range, making them a highly efficient solution. These motors also offer the advantage of simpler control mechanisms. On the other hand, SPM electric motors, while providing comparable performance, may be less cost-effective due to the ease of magnet placement on the rotor. The performance of internal permanent magnet synchronous machines (IPMSMs) is significantly impacted by the design of the rotor and the permanent magnet distribution. By optimizing the rotor design, it is possible to enhance the performance of IPMSMs, as highlighted in [6].

Different techniques like chill casting and powder metallurgy can be employed to create anisotropic rare-earth (RE) magnets with aligned crystallographic grains. These methods result in larger grain sizes, typically in the range of a few micrometers, as opposed to the smaller grain sizes achieved through rapid solidification. The magnets produced through the sintered powder process are known as sintered magnets. In this process, the RE-magnet alloy is initially strip cast from the molten state, resulting in a material with a relatively fine-scale solidification microstructure and larger grains. The cast material is then fragmented through hydrogen decrepitation and milling, resulting in particles with the desired size, where each particle represents a single crystal grain. These particles are aligned using a magnetic field and pre-compacted before undergoing vacuum sintering, which leads to the formation of a fully dense sintered block [8, 9, 10].

Stator winding configuration is a key factor in the design of an electric motor. For three phase AC machines there are two configurations for stator windings: distributed windings and concentrated windings. In this specific case study, distributed windings, developed with the hairpin technology will be adopted. It is the ideal solution to achieve performance, while guaranteeing high efficiency. In the distributed winding configuration, the winding is always wound around a minimum of two teeth. At the top and bottom parts of the motor, the winding heads are located. Non-negligible ohmic losses are associated to the winding heads, particularly when the ratio between the motor's diameter and length is greater than one. A huge advantage of this configuration is that the resulting back electromotive force has a smooth sinusoidal shape. It implies that the magnitude of the second order voltage harmonics is very limited and that the core losses developed accordingly are minimal [11].

2.2 Electric Motor Losses

In any application, working in ideal conditions is unattainable because of the presence of losses. The correct estimation of the electric motor losses is of crucial importance for an accurate prediction of the motor efficiency in the design phase. Electric motor losses can arise from multiple sources, including resistive losses in the motor windings better known as Ohmic or Joule losses, mechanical friction and bearing losses, core losses in the magnetic circuit, and other auxiliary (stray) losses. An overview of each of these efficiency-reducing factors in an electric motor is provided in the following sections.

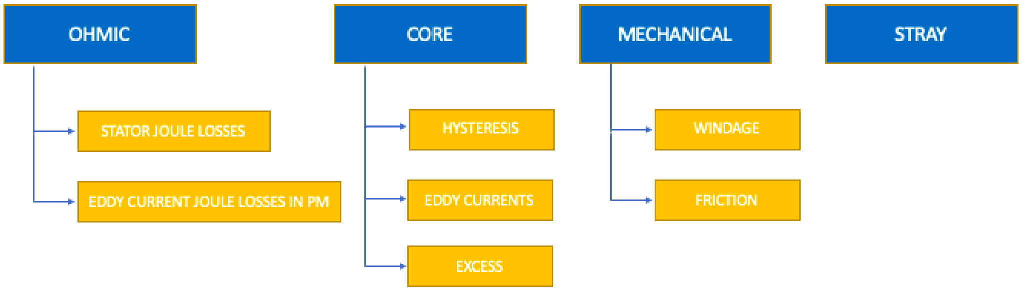

Figure 2.1: Electric motor losses

2.2.1 Joule Loss

An electrical current flowing through a wire conductor generates power losses, described by Joule's law. Neglecting the current displacements, this loss for a three-phase electric machine can be evaluated as [12]:

$$P_{DC} = 3 \cdot R_{stator} \cdot I_{ph}^2 \tag{2.2.1}$$

where R_{stator} is the ohmic phase resistance, I_{ph} is the phase current and 3 is a factor to account for all the motor phases in the computation.

The, so called, k_{AC} factor is introduced to consider the AC current displacement to the DC copper loss.

$$k_{AC} = \frac{P_{AC}}{P_{DC}} \tag{2.2.2}$$

whre P_{AC} and P_{DC} the alternate current ohmic loss and the direct current ohmic loss in an electric motor.

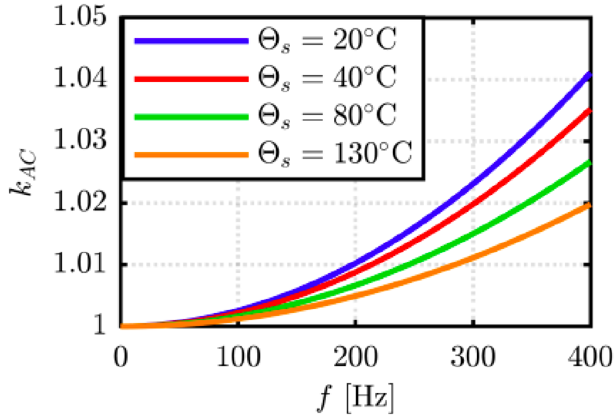

Figure 2.2: AC factor function of the frequency, for different winding temperature [13]

Increasing the operating frequency, skin effect and proximity effect phenomena would be enhanced. Skin effect is a phenomenon that occurs in conductive materials, especially in high frequency applications. It refers to the tendency of currents to flow along the surface of a conductor, rather than uniformly through the entire cross section. As the frequency of the current increases, the current flowing deep within the conductor experiences an increase in resistance which causes an exponential decrease in the current as the depth increases.

Two main approaches to determine the influence of the skin effect exist: analytical and experimental-based. In the following, the analytical approach will be explained in detail [14].

In case of numerous conductors, these are all series connected, such that the same current flows through them. Then the average increase in resistance, or field coefficient K_r, is given by the following relationship:

$$K_r = \phi(\xi) + \frac{N_n^2 - 1}{3} \cdot \psi(\xi) \tag{2.2.3}$$

where:

$$\xi = h \cdot \sqrt{\frac{f}{50}} \cdot \sqrt{\frac{b}{a}} \cdot \sqrt{\frac{\sigma}{50}} \tag{2.2.4}$$

$$\phi(\xi) = \xi \cdot \frac{sh(2\xi) + sin(2\xi)}{ch(2\xi) - cos(2\xi)} \tag{2.2.5}$$

$$\Psi(\xi) = \xi \cdot \frac{sh(\xi) - sin(\xi)}{ch(\xi) + cos(\xi)} \tag{2.2.6}$$

In equation (2.2.4) a is slot's width, whereas b and h are conductor's width and height. These are all expressed in $[cm]$. γ is the conductor's material conductivity, f is the power supply frequency and N_n is the number of conductors in the slot.

The skin effect phenomenom characterizes the end windings too however, the influence is smaller because of the distance from the stator iron core. Consequently, the average resistance increase in all the conductor geometry is lower than the field coefficient K_r, which refers to the conductors in the slots only.

$$K_r' = \frac{K_r + \lambda}{1 + \lambda} \tag{2.2.7}$$

where K_r' is the overall resistance increase for the windings, while λ can be computed using the given equation:

$$\lambda = l_s / l_i \tag{2.2.8}$$

where λ is the ratio between the length of the end windings l_s and the slot's length l_i.

Theoretical studies show the greater influence of conductor's height rather than width [15]. In an electric motor the skin effect can be reduced by employing the hairpin technology for the stator windings.

Proximity effect arises when multiple current-carrying conductors, which generate magnetic fields, are situated in close proximity to each other. The magnetic fields produced by the conductors interact inducing current in the conductors themselves. It has been shown that proximity effect and skin effect are orthogonal, thus they can be evaluated separately and then added [16, 17].

The proximity effect losses for a rectangular conductor can be expressed as:

$$P_{prox} = G \cdot H_e^2 \tag{2.2.9}$$

where H_e is the peak value of the external magnetic field caused by currents flowing in the surrounding conductors.

The factor G can be expressed as:

$$G = \frac{\frac{\sqrt{\pi}}{2} \cdot d(\xi)}{\sigma} \cdot \frac{sinh(\xi) - sin(\xi)}{cosh(\xi) + cos(\xi)} \tag{2.2.10}$$

where ξ is a parameter dependent on the conductor geometry, σ is the conductor conductivity.

The hairpin technology allows to arrange the conductors such that the magnetic field generated in adjacent conductors can be cancelled out, reducing the proximity effect.

2.2.2 Core Losses

Core losses, also known as iron losses, are generated by an alternating magnetic field acting on a ferromagnetic material, since any material does not exhibit perfectly efficient magnetic response. Core loss accounts for 15 - 25 % of the overall motor losses for an induction motor, and these percentages are even higher if we refer to permanent magnet machines [9, 18, 19, 20, 21].

The approach adopted to treat these losses is to decompose the average power loss as the sum of a dynamic and a hysteresis contribute.

$$P_{core} = P_{hyst} + P_{dyn} \tag{2.2.11}$$

Physically speaking, P_{hyst} is developed from the discontinuous character of the magnetization process at a microscopic scale, while P_{dyn} is related to the macroscopic behavior of the magnetic structures inside the material [22, 23]. The dynamic contribute can, in turn, be expressed as the sum of a so-called classical term and an excess term [18].

$$P_{dyn} = P_{class} + P_{exc} \tag{2.2.12}$$

Where P_{class} starts from the assumption of a perfectly homogeneous magnetization in space. On the other hand, P_{exc} accounts for the highly inhomogeneous local counter fields due to eddy currents and microstructural interactions [24].

Bertotti [12] proposed a model including one supplementary term of anomalous loss. Eventually, the expression of the core losses is:

$$P_{core} = P_{hyst} + P_{class} + P_{exc} \tag{2.2.13}$$

Thus, the core losses are distinguished in hysteresis, eddy current and excess loss. The engineering approach of treating them singularly is just empirical and finalized to separate the different influences due to frequency and flux density variations. In the subsequent paragraphs each constitutent of the iron loss is discussed individually, to provide a clearer undestanding of each of these components:

- *Hysteresis loss:* The hysteresis loss is determined on the area of the quasi-static hysteresis loop. A widely adopted assumption is to consider the hysteresis energy loss independent on frequency. It is valid at very low frequencies, since the magnetic field distribution would be uniform in the motor. However, increasing the operating frequency, the skin effect causes the peak magnetic field to vary non-uniformly in the material, thus minor hysteresis loops are developed [25, 26].

  The procedure to evaluate the magnetic field in every region of the motor, at high frequency, is computationally expensive. Hence, the solution applied in FEA software is to consider the total hysteresis loss dependent on the only peak magnetic field. Equation 2.2.14 shows the analytical model used for the hysteresis loss, accordingly to Steinmetz's equation [27].

  $$P_{hys} = K_h \cdot f \cdot \beta^{\alpha} \tag{2.2.14}$$

  where K_h is a coefficient evaluated fitting experimental data, f is the operating frequency and β is the peak magnetic induction. In literature, the most common approach is to set the exponent α equal to 2. Figure 2.3 shows the hysteresis loop at different operting frequencies and peak magnetuc induction reached.

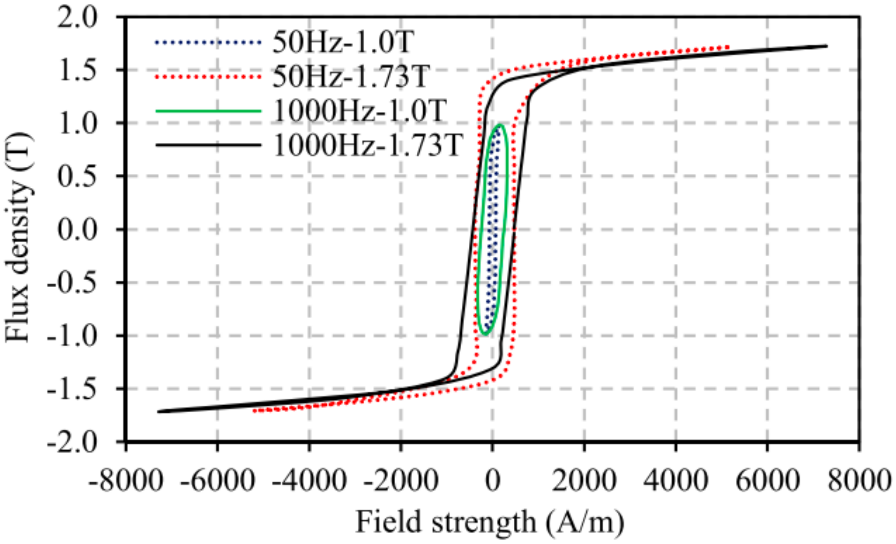

Figure 2.3: B-H loops at two different operating frequencies and peak magnetic fields [28].

- *Eddy current loss:* This loss arises from the fact that the core is made up of conductive material. Thus, the voltage generated by the variable magnetic field will induce circulating currents in the material. In the assumption of uniform magnetic field, the expression of the classical Eddy current loss is given starting from the Maxwell-Faraday equation:

  $$\vec{\nabla} \times E = \frac{d\beta}{dt} \tag{2.2.15}$$

  where E is the electric field, while β is the magnetic field.

  The instantaneous power loss due to Eddy currents can be defined for a magnetic lamination of thickness d and conductivity σ as:

  $$P_{class} = \frac{1}{12} \cdot \sigma \cdot d^2 \beta^2(t) \tag{2.2.16}$$

  Since the Eddy current loss depends upon the rate of change of flux as well as the resistance of the path, it is reasonable to expect this loss to vary as the square of both the maximum flux density and frequency [29]. For a sinusoidal excitation, the previous expression is simplified as:

  $$P_{class} = K_e \cdot f^2 \cdot \beta^2 \tag{2.2.17}$$

  where K_e is an experimental coefficient to be evaluated through fitting of the equation on measured loss data. f is the operating frequency and β is the peak magnetic induction.

- *Excess loss:* Steinmetz equation proposes a calculation of the core losses based on two terms, i.e. a hysteresis contribute and a Eddy current loss contribute. However, this formula is only applicable under the assumption of magnetic flux density lower than of 1.0 Tesla and hysteresis loop in static condition. This scenario is unattainable in electrical machines and the experimental results show a big discrepancy with respect to the analytical calculations with the Steinmetz equation.

  Several models have been proposed in [24, 26, 30] to close the gap to the experimental outcomes, however such models do not describe the excess loss in a real lamination specimen. In his paper, Bertotti proposes an explanation for the physical meaning of the excess loss [12]. He affirms that the excess loss can be identified as the result of the competition between the external magnetic field and the local counter fields due to eddy currents or other microstructural interactions. Under sinusoidal excitation, the expression to evaluate the excess loss is:

  $$P_{exc} = K_e \cdot f^{1.5} \cdot \beta^{1.5} \tag{2.2.18}$$

  f is the operating frequency and β is the peak magnetic induction. K_e is a coefficient evaluated fitting the experimental core loss for a specific material.

Manufacturing effects, saturation and rotational loss are the main aspects driving the difference between what are the actual core losses and the ones given by the modified Bertotti method. The subsequent list elaborates on the individual impact of each of these factors.

1. *Rotational loss:* Epstein frame tests are widely employed to retrieve the magnetic properties of materials and the coefficients for the loss models. Nevertheless, these tests are performed considering an alternating field and the extracted coefficients would give an accurate prediction of iron loss in transformers, in which the alternating magnetic field is predominant [10, 31]. In rotating machines, as electric motors currently employed for automotive propulsion, there exists a rotational flux component which is not negligible. The final trajectories of the flux vectors may be lines, ellipses depending on which region of the motor is under analysis. The greatest rotational variations of the flux vectors are found at the roots of the teeth [32, 33].

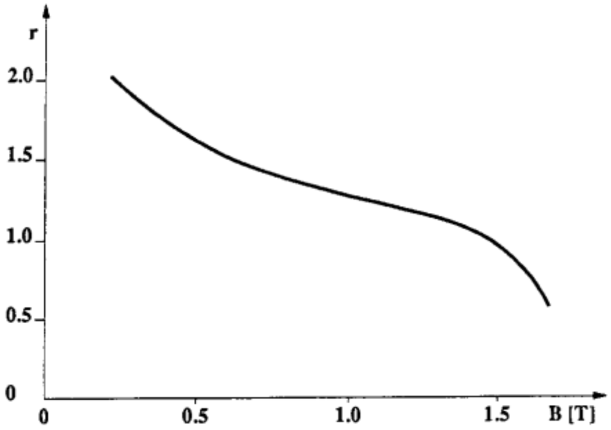

Figure 2.4: Dependence of r on induction in nonoriented SiFe laminations [15]

The model shown in the following equation is adopted to account for both flux vector rotation and flux density harmonics:

$$P_{core} = \sum_{j=1}^{n} \sum_{i=1}^{m} g_i \cdot [(K_h \cdot f \cdot \beta_{mji}^2 + K_c \cdot f^2 \cdot \beta_{mji}^2) \cdot (1 + \gamma_{lam} \cdot c_{ij}] \tag{2.2.19}$$

where g_i is the mass of the infinitesimal element, m is the total number of elements in the iron core and n is the maximum harmonic order considered. f is the operating frequency, β_{mij} is the peak magnetic field, γ is a factor that depends on the lamination material and c_{ij} is the short axis to long axis rate of the flux vector locus for the element i at the harmonic order j.

2. *Saturation loss:* At high operating frequencies and flux densities, the method proposed by Bertotti does not account for the saturation of some regions of the iron core. The most common approach is to consider a corrective factor as reported in equation (2.2.20) [34] :

   $$P_{core} = (1 + \alpha_3 \cdot \beta_m^{\alpha^4}) \cdot (P_{hys} + P_{class} + P_{exc}) \tag{2.2.20}$$

   where α_3 and α_4 are two experimental coefficients, obtained by fitting the experimental magnetic field versus magnetic induction curve in the non-linear region.

3. *Manufacturing effects:* During the manufacturing of an electric machine, electrical steel is subjected to different processes as cutting, interconnecting and clamping with screws. Each of these manufacturing techniques has significant impact on the material's properties. The typical processes for series production, as punching or laser cutting substancially deteriorate the characteristics of the electrical sheet. This modification is particularly severe getting close to the cutting edge; thus attention must be paid to the cutting technique adopted. This effect is more noticeable for small electric vehicles as the relative width of the impacted area is larger [35, 36, 37].

   Experimental measurements indicate a significant impact of the manufacturing processes on the stator core losses. Depending on the cutting technique and the setup of the cutting tool, different magnitudes of degradation are observed. A study revealed a core loss increase from 10 to 28 %, as a result of different cutting methods [18].

   Welding is the most common used technique for stacking the stator laminations. The heat produced in the process ends up generating thermal stresses and influencing the magnetic permeability of the electrical sheets. Furthermore, the welded area can be the path for the development of global Eddy currents. The latter would majorly increase the core losses in the material. As a consequence of the welding process, core losses experience an increase in the range of 5 to 20 % [18, 36, 38].

   The outer frame is shrink fitted to the welded stator stack. As a result, compressive stresses will be developed and these affect the magnetic properties of the material. A raise as high as 10 % in the iron loss was found as a consequence of the mechanical stress effects on the electrical machine [39].

2.2.3 Mechanical Losses

Mechanical losses in electric motors can be classified as friction and windage loss. Friction losses occur in the bearings housing the motor shaft. Swedish Ball Bearing Factory established an experimental relationship between the load acting in the bearings and the power loss:

$$P_b = 0.5 \cdot \mu_{fr} \cdot F_b \cdot D_b \cdot \omega \tag{2.2.21}$$

where μ_{fr} is the friction coefficient of the bearing, F_b is the equivalent dynamic bearing load, D_b is the bore diameter of the bearing and ω is the angular frequency, at which the motor is rotating [40].
On the other hand, windage loss are related to the friction between air and the rotor of an electric machine. This loss is strictly related to motor geometry, as a consequence a direct formulation for it is not available. Nevertheless, it is possible to rely on computation fluid dynamics (CFD) to compute a reasonable value of the windage loss.

2.2.4 Stray Losses

IEEE standard 112B classifies the stray losses as the portion of the total losses in a machine not accounted for by the sum of friction and windage, stator and rotor copper loss and no-load core loss. The standard says that if the measurement of all these quantities is not feasible, the stray losses are assumed as a fixed percentage between 0.9 and 1.8 % of the output power. In particular, stray losses in electric motors can be attributed to causes such as magnetic flux leakages or uneven distribution of the magnetic field in the rotor and stator, increased resistance in the end windings, and the presence of harmonic components in the electrical supply [41].

2.2.5 Temperature Impact on the Electric Machine Performance

The electromagnetic behavior, and consequently the power production of an electric motor is widely affected by temperature. Raising the temperature influences the electric winding and iron sheet resistivity, altering the magnets' properties, in terms of hysteresis curve and flux density and varying the viscosity of the lubricant in the bearings [42].

The copper loss would increase, since the winding resistance linearly increases with temperature. Any metallic material experiences a resistivity increment, given by the following relationship [43]:

$$R = R_0 \cdot (1 + \alpha \cdot (T - T_0)) \tag{2.2.22}$$

where R_0 is the resistivity at a reference temperature T_0. α is the temperature coefficient of the material and T is the operative temperature.

The iron losses have a decreasing trend with temperature increment. Less polarization energy is needed for the Weiss domains, since a higher temperature implies easier atomic motion. As a result, the remanence B_r and the magnetic coercivity H_c decreases in the iron core. The hysteresis loop contracts, resulting in lower hysteresis losses. The eddy currents depend on the induced voltage. However, a higher resistance of the sheet iron causes a lower current to flow in the sheet. The following expression clarifies the relationship between the classical loss and the operating temperature [43].

$$P_{class} \propto \frac{1}{R_{iron}} \propto \frac{1}{1 + \alpha_{iron} \cdot \Delta T} \tag{2.2.23}$$

The iron losses depend quadratically on the magnetic flux density. In permanent magnets electric motors, as the one considered in this research activity, the most dominant contribute to the magnetic field comes from the internal permanent magnets. A 100 Kelvin temperature increment induces a remanence as well as coercivity reduction for Neodymium-Iron-Bore magnets from 8 to 10 % [28]. A reduction of the peak magnetic flux leads to lower iron losses, however to obtain the required motor torque, current must rise at the same time.

Lastly, the friction losses originated in the bearings reduces with the increase of the operative temperature, since lubricant viscosity drops. Ventilation losses are assumed unaffected by the operating temperature.

In the thermal analysis of an electric motor, it must be taken into account that iron losses have a decreasing trend with the increase of temperature, while copper loss increments under the same temperature variation. This implies that it exists an energetically optimal motor temperature, that minimizes the losses. Figure 2.5 offers a visual representation of the optimal operating temperature for the motor model proposed in [42]. The thermal control in electric motors is aimed at reaching and maintaining this temperature.

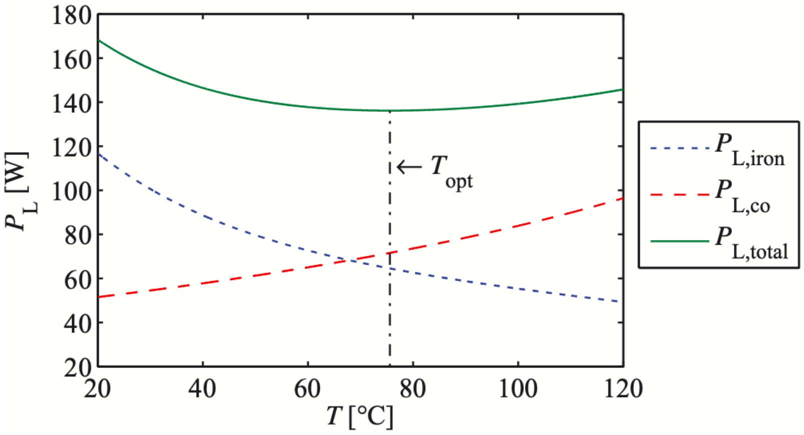

Figure 2.5: Optimal operating temperature from power loss balance [42]

2.3 Loss Modeling

2.3.1 Finite Element Analysis

Finite element analysis is a widely adopted tool to solve engineering problems arising from various physical fields as electromagnetic, thermal, structural or others. It can be described as a numerical technique, that allows to solve complex problems by reducing the solution domain into small parts called elements. The finite element method has a solid theoretical foundation. It is based on mathematical theorems that guarantee an asymptotic increase of the accuracy of the field calculation toward the exact solution as the size of the finite elements used in the solution process decreases.

To fully characterize the behavior of each element, it is needed to identify the basic unknowns or field variables. Finite element analysis has the huge advantage of being applicable to geometries that contain heterogeneous materials, which makes it the ideal solution for modeling and simulating the performance of electric motors. The electromagnetic field acting in the electric machine is assessed solving Maxwell's equations in a finite region of space with appropriate boundary conditions.

The transient solver is capable of assessing magnetic field, energy, torque and power loss over a specified period of time. As reported in [44], the time dependent magnetic equation is expressed as:

$$\nabla \times \upsilon \cdot \nabla \times A = J_s - \sigma \cdot \frac{dA}{dt} - \sigma \cdot \nabla V + \nabla \times H_c + \sigma \cdot V \times \nabla \times A \tag{2.3.1}$$

where H_c is the coercivity of the permanent magnets, A is the magnetic vector potential, V is the electric potential, υ is the reluctivity and J_s is the source current density.

The transient solver applies a reference frame, which is fixed with respect to the components in the model. All the moving components are analyzed in their own reference frame, which implies that the velocity is always considered zero. Thus, the magnetic equation becomes:

$$\nabla \times \upsilon \cdot \nabla \times A = J_s - \sigma \cdot \frac{dA}{dt} - \sigma \cdot \nabla V + \nabla \times H_c \tag{2.3.2}$$

An important aspect of electric motor design is the prediction of the losses over a wide speed and load range. It is highly desirable to assess with satisfactory precision iron, Joule and mechanical loss in order to make the proper layout modifications as early as the design stage. The most dominant loss components that determine the efficiency of an electric motors are the iron losses and the copper loss. Nevertheless, the contribution of the mechanical losses is not negligible and their value becomes relevant with the increase of the operating speed. In the following sections the modeling of each of the previously cited losses is proposed.

2.3.2 Joule Loss Modeling

The power dissipation in the windings of an electric motor results in Joule loss. When modeling stator coils in a virtual environment, stranded conductors can be used. They do not exhibit eddy current behavior and are considered to be filaments too thin to be practically modeled in a finite element grid, though. Consequently, to simulate hairpin technology windings, the solid conductor model is typically employed. Solid conductors are large enough to be modeled with finite elements and the skin effect will depend not only on the frequency, but also on the location of the other conductors.

The guide of the software ANSYS Maxwell [44], reports the total current density as shown in equation (1.2.3):

$$j_t = -\sigma \cdot \frac{dA}{dt} - \sigma \cdot \nabla \cdot V \tag{2.3.3}$$

where j_t is the total current density, A is the magnetic vector potential, σ is the conductivity and V is the electric potential.

In turn, the equation can be expressed as:

$$j_t = j_e + j_s \tag{2.3.4}$$

where j_e and j_s are the eddy current density and the source current density.

For solid conductors with a current source, as in the case study of this research project, the current source for the n^{th} conductor is given by the following equation:

$$\int \int_{\Omega_c} (-\sigma \cdot \frac{dA}{dt} + j_s) \cdot d\Omega_c = \int \int_{\Omega_c} j_t \cdot d\Omega_c = I_t \tag{2.3.5}$$

Ω_c is the width of the cross section of the n^{th} conductor , I_t is the known total current, j_s is the source component to be solved for and j_t is the total current density.

Two methods exist for modeling Joule losses: they can be integrated directly into the software environment and evaluated during each computed simulation, or they can be modeled during the post-processing phase. The second method is implemented in this thesis as it enables us to incorporate a frequency and temperature resistance model. Additionally, utilizing an adaptable post-processing code allows to analyze the performance of various models without sacrificing result accuracy. The coefficients can just be modified when transitioning from one model to another.

Temperature and Frequency Dependent Resistance Model

Stator winding resistance plays a crucial role in the performance and behavior of electrical machines. To accurately capture its temperature and frequency dependent behavior, a comprehensive model has been developed. This model takes into account the variations in resistance caused by changes in temperature and frequency, enabling more accurate predictions and analysis of the electrical machine's characteristics.

$$R_{stator} = A_1 \cdot \omega^2 + B_1 \cdot \omega + C_1 \tag{2.3.6}$$

where R_{stator} is the stator resistance, ω is the angular speed of the motor expressed in $[rpm]$. The coefficients A_1, B_1, and C_1 in the equation exhibit a linear dependence on temperature, as demonstrated below:

$$A_1 = A_0 \cdot [1 + \alpha \cdot (T - 20)] \tag{2.3.7}$$

$$B_1 = B_0 \cdot [1 + \alpha \cdot (T - 20)] \tag{2.3.8}$$

$$C_1 = C_0 \cdot [1 + \alpha \cdot (T - 20)] \tag{2.3.9}$$

the coefficients A_0, B_0, and C_0 are features of the windings and are measured at the reference temperature of 20 Celsius degrees. α is the temperature coefficient and for copper it is 0.393 %. Lastly, T is the operating temperature.

Figure 2.6 shows the experimental trend of the stator windings resistance at different operating temperatures and frequency.

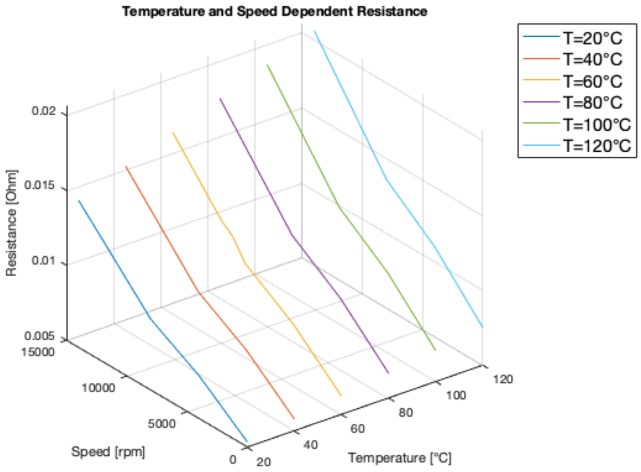

Figure 2.6: Stator winding resistance evaluated at different operating speeds and temperatures.

2.3.3 Core Loss Modeling

The prediction of the core losses is still a challenging aspect in the design of electric machines. While core loss computation in frequency domain is straightforward, more complex is the analysis in time domain. The most common approach adopted in FEA-based analysis is the total core loss separation into static hysteresis loss, classical eddy current loss and excess loss. This model is better known as 'modified Bertotti method' [12].

Under sinusoidal flux condition the modified Bertotti method has the following expression:

$$P_{core} = P_{hys} + P_{class} + P_{exc} \tag{2.3.10}$$

where P_{hys} is the hysteresis component of the core loss, P_{class} are the eddy current losses and P_{exc} are the excess losses.

$$P_{core} = K_1 \cdot \beta^2 + K_2 \cdot \beta^{1.5} \tag{2.3.11}$$

where K_1 and K_2 are two coefficients that can be evaluated respectively as:

$$K_1 = K_h \cdot f + K_c \cdot f^2 \tag{2.3.12}$$

$$K_2 = K_e \cdot f^{1.5} \tag{2.3.13}$$

where K_h and K_c reported in equation (2.3.10) are respectively the hysteresis and eddy current loss coefficients, while K_e reported in equation (2.3.13) is the excess loss coefficient. f is the operating frequency, whereas β is the peak magnetic field.

The manufacturing effects are taken into consideration with a cut edge effect model:

Cut-edge effects

The plastic deformation and residual stress are much larger in correspondence of the cut edge, causing material properties deterioration and consequently, higher core losses. It is possible to account for this effect with cut-edge loss model.

$$P_{core} = (p_0 + k_0 \cdot p_0) \cdot d_c \cdot S_c \tag{2.3.14}$$

p_0 are the core loss without considering cut-edge effects. k_0 is the cut-edge factor, while d_c and S_c are respectively the cut-edge deformation depth and the cut-edge area.

Thus, the core loss increase due to cut-edge effect is given by the equation (2.3.15):

$$\Delta P_{core} = p_0 \cdot k_0 \cdot d_c \cdot S_c \tag{2.3.15}$$

Since k_0 and d_c cannot be assessed singularly, it is possible to introduce an equivalent cut depth d_{eq}:

$$d_{eq} = k_0 \cdot d_c \tag{2.3.16}$$

The evaluation of the parameter d_{eq} is based on measurements of core loss of lamination sheets with variable width to consider the cut-edge effects.

2.3.4 Mechanical Loss Modeling

The kinematics of the model is defined by the core equations of dynamics that describe the motion of objects in translation or rotation. The mechanical loss modeling in a virtual environment is given by equation (2.3.17) [44]:

$$J_{mot} \cdot \ddot{\theta} = T_{EM} - T_R \tag{2.3.17}$$

where J_{mot} is the motor inertia, $\ddot{\theta}$ is the second order derivative of the angle swept by the motor. T_{EM} and T_R are respectively the electromagnetic and the resistance torque.

There are two potential approaches for developing a mechanical loss model. The first involves integrating the loss coefficients directly into the software environment. Alternatively, the model can be constructed during post-processing, while assuming ideal kinematic conditions in the software, meaning negligible friction.

The resistant mechanical torque can be integrated in the software, by introducing the following coefficients:

- *Constant coefficient:* it represents the friction in the bearings. Its unit is $[N \cdot m]$.
- *Viscous friction coefficient:* it accounts for the exceptional presence of oil in the air gap. In most of the cases, this contribute is considered null. Its unit is $[\frac{N \cdot m \cdot s}{deg}]$
- *Friction coefficient proportional to the square of the angular speed:* this coefficient accounts for the windage losses. Its unit is $[\frac{N \cdot m \cdot s^2}{deg^2}]$

Mechanical losses are usually difficult to estimate beforehand. Nevertheless, they can be expressed as a function of the speed, as in the model proposed by Ferrari et al. [13]. The same assumption will be adopted in this research activity and the mechanical losses will be described by a third order polynomial:

$$P_{mech} = c_0 \cdot \omega^3 + c_1 \cdot \omega^2 + c_2 \cdot \omega + c_3 \tag{2.3.18}$$

where c_0 , c_1 , c_2 and c_3 are coefficients obtained from the fitting of experimental curves. ω is the angular speed of the rotor, expressed in $[rpm]$.

2.4 Efficiency Map

In the automotive sector, the largest part of current research involves the study of the efficiency of powertrains. When considering the design of motor drives, the overall efficiency is affected by both the efficiency of the inverter and of the electric motor. Commonly, greater attention is paid to the electric motor efficiency, since it is normally lower and has a greater variability with respect to the operating conditions and the type of machine.

Improving the efficiency of electrical machines, applied to electric vehicles or hybrid electric vehicles, implies both energy savings and a wider driving range per charge. The adopted method for evaluating vehicle energy efficiency is to examine the performance over standard driving cycle.

An efficiency map for an electric motor can be described as a contour plot of the electrical machine efficiency on axes of torque and speed. For each operative point, i.e. torque/speed combination, it provides the ratio between the output power delivered by the motor and the input power supplied to the motor [45, 46, 47].

The most common approach to evaluate the efficiency map of an electric motor is to employ intensive FEA. However, FEA needs a benchmark for comparison, which should be the efficiency and loss maps, experimentally obtained with a dedicated test bench [48].

2.4.1 Experimental Evaluation of the Efficiency Map

The experimental tests to evaluate the efficiency map for an electric motor are conducted on a dedicated test rig. In the testing procedure proposed by Bojoi et al. [49], the motor under test (MUT) is fed by an inverter and a controller is used to implement a torque control strategy. The test rig must be embedded with temperature, speed and torque sensors, to accurately assess input and output power. The speed range of interest is divided into equal intervals. For each speed, torque will be varying between a minimum and a maximum values with a reasonable number of intermediate points. A driving machine fixes the speed for the operative point, while the MUT is torque controlled. For each operative point, the input electrical power is computed as:

$$P_{input,avg} = \frac{3}{2} \cdot \frac{1}{T} \cdot \int ((v_\alpha \cdot i_\alpha + v_\beta \cdot i_\beta) \cdot dT) \tag{2.4.1}$$

Where v_α is the α component of the stator winding voltage in $\alpha\beta$ reference frame, whereas v_β is the β component of the stator winding voltage in $\alpha\beta$ reference frame. i_α and i_β are respectively the α and β components of current in the α, β reference frame. The Clarke transformation is employed on the measured current and voltage values from each individual phase, to obtain the currents and voltage in $\alpha\beta$ frame.

$$P_{copper} = R_{stator,avg} \cdot \frac{1}{T} \cdot \int ((i_a^2 + i_b^2 + i_c^2) \cdot dT) \tag{2.4.2}$$

where $R_{stator,avg}$ is the average stator resistance, i_a, i_b and i_c are respectively the phase A, B and C currents of a three phase electric motor. T is the electrical period considered in the analysis.

A torque and a speed sensor allow the evaluation of the output mechanical power, as shown in equation (2.4.3):

$$P_{output,avg} = T_{m,avg} \cdot \omega \tag{2.4.3}$$

where $T_{m,avg}$ and ω_m are respectively the output torque and the operating speed of the MUT.

The mechanical losses are evaluated with a machine where the magnets are extracted, while the iron loss would be given from the difference between input power and output power and the losses previously evaluated.

$$P_{core} = P_{input} - P_{output} - P_{joule} - P_{mech} \tag{2.4.4}$$

where P_{input} is the input power, P_{output} is the output power , P_{joule} are the ohmic losses and P_{mech} are the mechanical losses. Finally, the efficiency for the each of the considered operative point, will be given by the following expression:

$$\eta_{mot} = \frac{P_{output,avg}}{P_{input,avg}} \tag{2.4.5}$$

where $P_{output,avg}$ and $P_{input,avg}$ are the output and the input power respectively.

2.4.2 Virtual Evaluation of the Efficiency Map

A crucial aspect of an electric motor design is the prediction of the efficiency map. A FEA-based time domain approach allow to simulate the performance of an electric motor and very accurately develop the motor efficiency map.

The procedure to evaluate the efficiency map resembles the experimental method in many respects. For each operating point of the torque/speed sweep considered, the ratio between input and output power gives the efficiency of the energy conversion $\eta_{mot,sim}$.

$$\eta_{mot,sim} = \frac{P_{output,sim}}{P_{input,sim}} \tag{2.4.6}$$

where $P_{output,sim}$ and $P_{input,sim}$ are the output and the input power respectively. The output power is given by the following equation:

$$P_{output,sim} = T_{output,sim} \cdot \omega \tag{2.4.7}$$

in the proposed expression, $T_{output,sim}$ is the electromagnetic torque, while ω is the angular speed of the motor.

The input power can be expressed as:

$$P_{input,sim} = P_{output,sim} + P_{core} + P_{mech} + P_{joule} \tag{2.4.8}$$

where P_{core} , P_{mech} and P_{joule} are the electric motor losses (iron, mechanical and core losses). The latter are calculated with the FEA software, on the basis of experimental models [49].

2.5 Research gap and how to address it

The literature reviewed for this research highlights several critical aspects related to the modeling and processing of motor losses. One significant difference between the model adopted in previous studies and the one used in this research is the approach to simulate stator resistance. While the analyzed literature relies on an average of experimental behavior at different frequencies, this research activity employs a model capable of accurately representing the stator windings resistance at varying speeds, aligning closely with experimental findings. This allows to account for the impact of temperature and AC effects, such as proximity and skin effects, not only on the current density distribution but also on the coil material's resistance.

Moreover, none of the reviewed articles and papers provide a comprehensive approach to address all motor losses in a simulation environment. Conversely, this project aims to model each motor loss component and develop an efficiency map for the electric motor by integrating virtual simulations with a post-processing MATLAB™ code.The adoption of an external code for post-processing plays a significant role in accomplishing the research objectives. The MATLAB™ script provides valuable contributions by incorporating a third-order polynomial model for mechanical loss and a resistance model that accounts for frequency and temperature dependencies. This enables a highly accurate representation of the motor's actual behavior.

From the company perspective, this work is aimed at speeding up the efficiency evaluation process, offering a tool that is capable of delivering the efficiency maps automatically, once the FEA simulation results are provided to the algorithm.

Chapter 3

Methodology

The methodology section provides a detailed explanation of the procedures and techniques employed to conduct the study, allowing readers to understand and evaluate the reliability and validity of the research. This section outlines the step-by-step approach taken to collect data, develop the motor and loss model and perform analyses.

3.1 Extraction of the Loss Model Coefficients

To optimize the design and performance of electric motors, it is essential to accurately quantify and characterize the mechanical, Joule and iron losses. One common approach is to extract loss coefficients that capture the relationship between the actual motor operating conditions and the corresponding losses. These loss coefficients provide valuable insights into the specific loss mechanisms. The extraction of loss coefficients plays a crucial role in the design optimization process.

Table 3.1: Electric motor loss models

Mechanical Loss Model	**Joule Loss Model**	**Core Loss Model**
$P_{\text{mech}} = c_0 \cdot \omega^3 + c_1 \cdot \omega^2 + c_2 \cdot \omega + c_3$	$P_{\text{joule}} = 3 \cdot R_{\text{stator}} \cdot I^2$	$P_{\text{core}} = K_h \cdot f \cdot \beta^\alpha + K_c \cdot (f \cdot \beta)^\gamma + K_e \cdot (f \cdot \beta)^\delta$

For this research activity the models reported in Table 3.1 have been adopted for simulating the electric motor losses. The coefficients of the mechanical, Joule and iron loss model have been obtained by fitting the experimental loss curves, with the MATLAB™ toolbox *CurveFitting*.

3.1.1 Mechanical Loss Model Coefficients

To extract the parameters of the mechanical loss model, the reference experimental curve comes from a 'Spin loss test' or 'No-load test'. This test aims to quantify the power losses that occur in the motor due to mechanical factors such as friction and windage. For this case study, the test has been conducted extracting the magnets from the rotor, to avoid flux generation that may induce unwanted currents in the stator windings.

The test data, provided by an original equipment manufacturer, includes the mechanical power loss at different operating speeds, as shown in Figure 3.1:

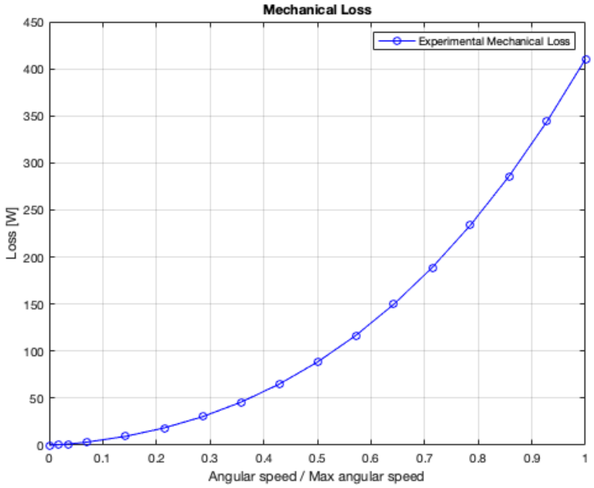

Figure 3.1: Variation of mechanical power loss with normalized operating speed

The motor underwent testing under no-load conditions, resulting in the extraction of data from sixteen operating points spanning the range between minimum and maximum speed.

The experimental mechanical loss curve has been then provided to the MATLAB™ *CurveFitting* toolbox, and a third-order polynomial has been used to approximate the curve. Figure 3.2 shows the outcomes of the approximation:

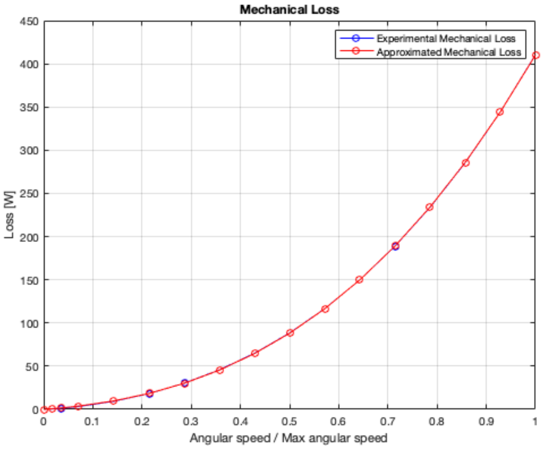

Figure 3.2: Comparison between experimental and approximated mechanical loss

The approximate curve, depicted in red in Figure 3.2, closely aligns with the experimental curve. However, a slight deviation can be observed specifically at very low speeds, where a slightly higher error is evident, as indicated by the error plot.

$$error = \frac{P_{experimental} - P_{model}}{P_{experimental}} \tag{3.1.1}$$

$P_{experimental}$ and P_{model} are respectively the experimental and the approximated mechanical loss. Figure 3.3 depicts the trend of the error with respect to the operating speed. The most significant deviation from the experimental behavior occurs at extremely low speeds. Although the peak per-

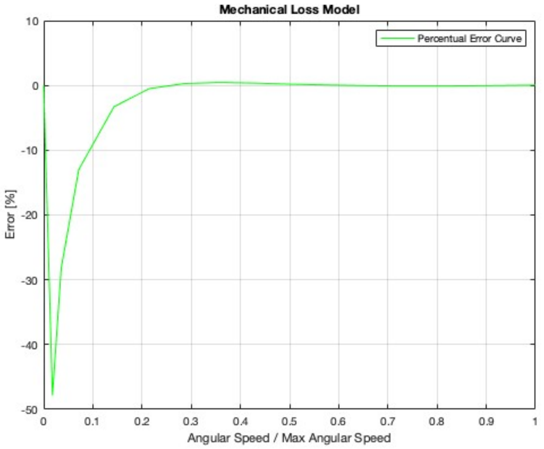

Figure 3.3: Estimation percentual error of the approximated mechanical loss

centage error reaches 47 %, the absolute value of the mechanical loss is very low, thus the error would be negligible. Consequently, the error can be considered negligible, affirming the model's accuracy in approximating the experimental behavior. Table 3.2 shows the coefficients adopted for the mechanical loss model.

Table 3.2: Mechanical loss model

Mechanical loss model
$P_{\text{mech}} = c_0 \cdot \omega^3 + c_1 \cdot \omega^2 + c_2 \cdot \omega + c_3$
$c_0 = 6.137 \times 10^{-8}$
$c_1 = 8.273 \times 10^{-5}$
$c_2 = 2.659 \times 10^{-2}$
$c_3 = 0$

3.1.2 Joule Loss Model Coefficients

The only parameter to be identified for Joule loss modeling is the winding resistance R_{stator}. From the experiments performed by the partner company, it has been observed a threefold increase of the resistance from the lowest operating speed to the peak speed condition. With respect to temperature, the resistance escalation follows a linear pattern, as indicated by a well-established experimental relationship.

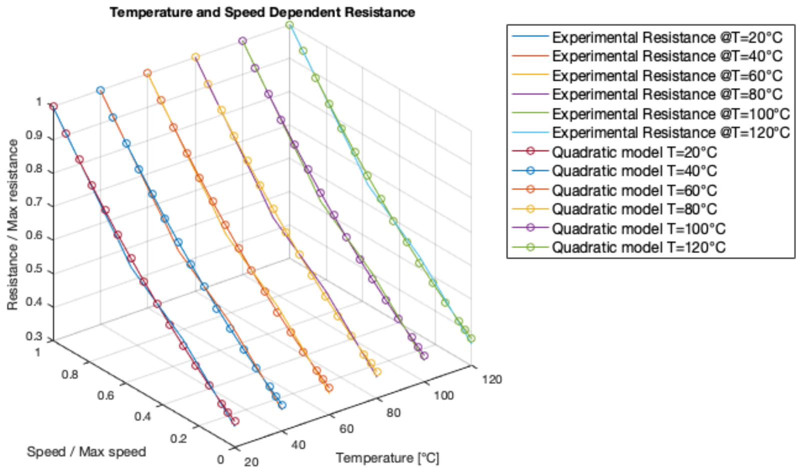

Figure 3.4: Comparison of experimental curve and approximated fitting function

As, shown in Figure 3.4, the most suitable modeling approach should incorporate dependencies on temperature and frequency to accurately capture the behavior of the system. In order to develop this model, it is necessary to conduct tests on the windings at various operating temperatures and excitation frequencies. The experimental procedure foresees to systematically increase the frequency of the applied current while measuring and documenting the corresponding values of winding resistance.

A speed-dependent second-order polynomial has been employed to approximate the stator winding resistance, whereas the polynomial coefficients are temperature-dependent.

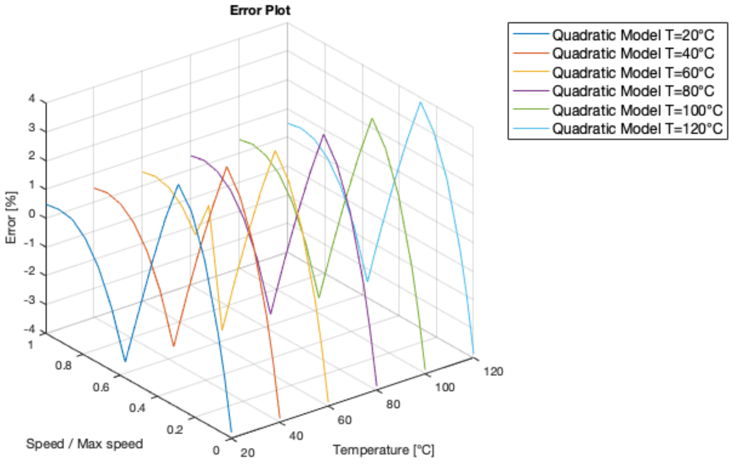

Figure 3.5: Estimation percentual error of the approximated stator resistance

The error in the approximation can be evaluated in percentage, as show in the following relationship:

$$error = \frac{R_{model} - R_{experimental}}{R_{experimental}} \tag{3.1.2}$$

where R_{model} is the modeled resistance, while $R_{experimental}$ is the experimental resistance.

The experimental data has been matched using the $CurveFitting$ toolbox, which allowed for the determination of the best-fitting mathematical function.

The stator resistance model approximation exhibits an error that is less than 4%, which, given that the absolute values are in the range of 10^{-4} Ohm, can be deemed negligible. Figure 3.5, the trend of the error is depicted in relation to speed and operating temperature. The model maintains a consistent level of accuracy almost independently on temperature. A slight variation is observed at a temperature of 60 Celsius degrees, where a more precise estimation is achieved and the error reduces to 0.61%. The coefficients used for the stator resistance model are presented in Table 3.3.

Table 3.3: Joule loss model

Joule loss model
$P_{\text{joule}} = 3 \cdot R_{\text{i}} \cdot I_{ph}^2$
$R_i = A_1 \cdot \omega^2 + B_1 \cdot \omega + C_1$
$A_1 = A_0 \cdot [1 + \alpha_e \cdot (T - 20)]$
$B_1 = B_0 \cdot [1 + \alpha_e \cdot (T - 20)]$
$C_1 = C_0 \cdot [1 + \alpha_e \cdot (T - 20)]$
$A_0 = 1.554 \times 10^{-11}$
$B_0 = 4.37 \times 10^{-7}$
$C_0 = 5.594 \times 10^{-3}$

3.1.3 Iron Loss Model Coefficients

The core losses test data, obtained from the steel manufacturer, includes information regarding the power loss per unit mass of material at various excitation frequencies and peak magnetic inductions. A specimen of the core material has been subjected to the Epstein frame test. It consists of four major phases. Firstly, the specimen is placed in an Epstein frame, which consist of a a laminated core with a primary and secondary winding. The frame allows for precise control of the magnetic field and measurement of the induced voltage. Subsequently, the excitation current is driven into the circuit and an alternated magnetic field is developed. The induced voltage in the secondary winding, resulting from the changing magnetic field, is measured using appropriate instrumentation. This voltage measurement provides information about the core losses in the material.

The testing frequencies encompass 50, 60, 100, 200, 400, 700, and 1000 Hz. For each frequency, the steel manufacturer has provided data on the magnetic induction, magnetic field, relative permeability, and core loss per unit mass. To these data are added some intermediate scenarios, at the operating frequencies of 66 , 133, 300 and 600 Hz. For each of these conditions, the value of the magnetic induction has been obtained averaging the experimental behavior.

Subsequently, the data is fitted using the previously mentioned *CurveFitting* toolbox. The adopted fitting function follows the modified Bertotti method. The performance of the iron loss model has been compared to the experimental results, and Figure 3.6 shows the error in the approximation. The error is evaluated in percentage, in accordance with the equation:

$$error = \frac{P_{model} - P_{experimental}}{P_{experimental}} \tag{3.1.3}$$

where P_{model} is the modeled iron loss, whereas $P_{experimental}$ is the core loss measured with the Epstein frame test. By analyzing the error distribution, it becomes apparent that the highest errors predominantly occur at lower frequencies, although their absolute values remain minimal. The most accurate estimation of iron loss occurs at higher frequency values, regardless of the magnetic field. In Table 3.4, the coefficients used for the iron loss model are reported.

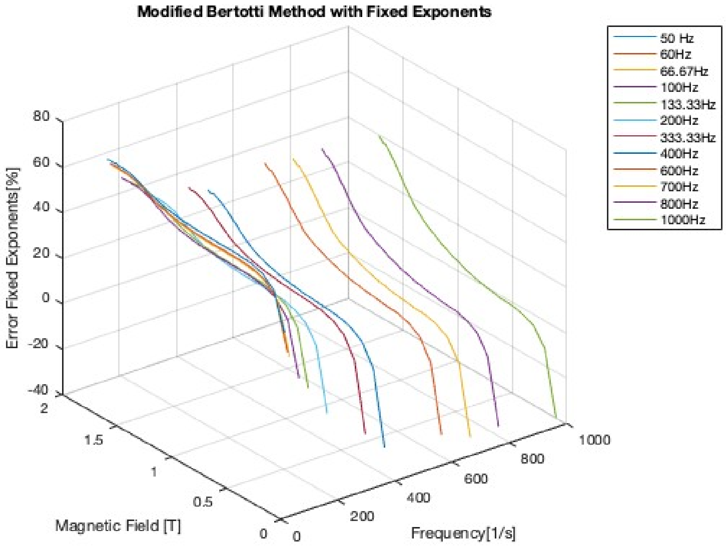

Figure 3.6: Percentual error of the iron loss model

Table 3.4: Iron loss model

Iron loss model
$P_{\text{core}} = K_h \cdot f \cdot \beta^2 + K_c \cdot (f \cdot \beta)^2 + K_e \cdot (f \cdot \beta)^{1.5}$
$K_h = 0.214$
$K_c = 0.1908$
$K_e = 5.095$

3.2 Electric Motor Model

The electric motor model analyzed in this research activity pertains to the Fiat 500 battery electric vehicle and is classified as an IPM synchronous machine. The rotor incorporates V-shaped internal permanent magnets made of sintered Neodymium Iron Boron material. As a consequence of their shape, the magnets can sustain a relatively high magnetic loading. In this case study, for the hairpin stator windings, a 2Y configuration has been implemented. Literature shows that this configuration allows to reduce the low-order space harmonics and consequently, significantly reduce the rotor core and magnet eddy-current losses.

Besides, the motor has eight poles, and the stator windings are organized into fourty eight stator slots with four conductors allocated per slot. The number poles is one of the factors impacting on the design on the motor and imposing limitation on size, maximum speed and torque envelop. Low torque ripple requirement for traction motors leads to an increase in the number of poles. On the other hand, having a too high number of poles induces an increase of the rotor geometry, in most of the cases incompatible with the current standards about motor sizing. The output torque shape and magnitude will be influenced by the number of pair poles.

3.2.1 Model Implementation in the Software Environment

Electric motors exhibit various dynamic aspects that impact their performance. These include spatial harmonics introduced by slotting, saturation variations, and cross-coupling resulting from different current pairs. Additionally, phenomena such as skin effect, switching effects, and the control strategy of power electronics converters further influence the electromagnetic behavior of the motor system. The thermal dynamics of the system are influenced by varying losses and cooling conditions at different operating points. Furthermore, the mechanical response is affected by factors such as torque, rotational speed, and electromagnetic forces.

Considering these complexities, it is necessary to model the dynamics of an electric motor drive in a manner that accounts for the interdependencies among these factors. Alternatively, decoupling the dynamics with reasonable assumptions can also be employed in the modeling process.

For this research activity, a 2D FEA model of the IPMSM was developed in Altair Flux™ and Ansys Maxwell™ to be used for the efficiency evaluation. By isolating a specific plane within the 3D model, important information about the motor's geometry, winding configurations, and magnetic field interactions can be captured in the resulting 2D representation. This simplified 2D model can then be utilized for electromagnetic simulations and analysis, allowing for a more focused and efficient evaluation of the motor's performance and behavior. Figure 3.7 and 3.8 dispaly the motor rispectively in isometric and side view.

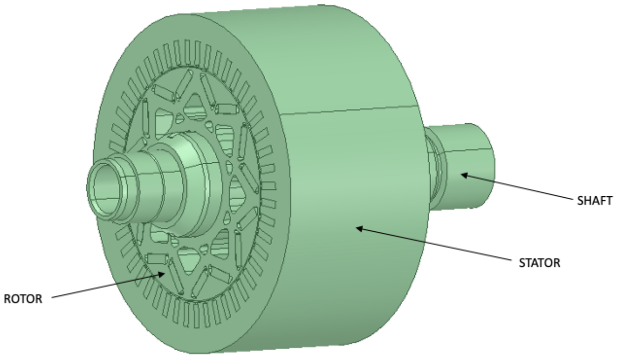

Figure 3.7: Isometric view of the electric motor, developed with ANSYS Maxwell™

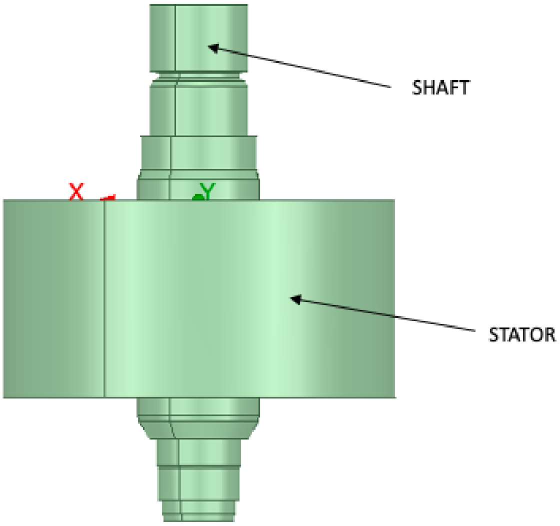

Figure 3.8: Side view of the electric motor, developed with ANSYS Maxwell™

The additional computational effort required to perform a more complex 3D simulation makes it an unfeasible option, considering that the resulting increase in accuracy would be only marginal in this regard. Figure 3.9 illustrates the bidimensional model of the motor used in the simulations. The rotor is characterized by a skewness of 6 degrees, which is taken into account by dividing it into five different sections and averaging the results across these sections. By leveraging the symmetries and periodicities within the model, the 2D geometry can be reduced to 1/8 of its original size.
The material properties for the copper wires, the magnets and the electrical steel are imported for the operating temperature of 100 °C.

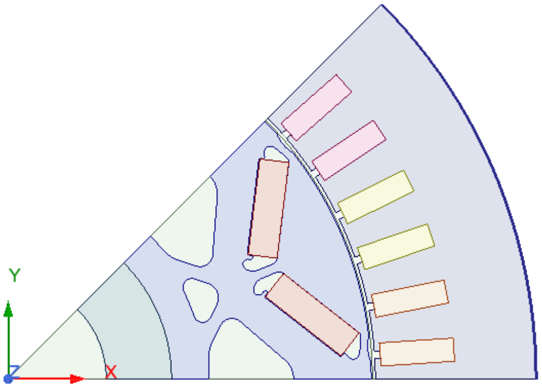

Figure 3.9: Electric motor model developed with ANSYS Maxwell™

3.2.2 Improvement in the Model Layout: Hairpin Technology for the Stator Windings

The starting model lacks information about the stator windings, making it impossible to implement the proper excitation circuit. Additionally, important phenomena such as the skin effect and proximity effect cannot be accounted for. This implies that there will be a significant error in determining the absolute value and distribution of current in the windings. As a result, accurate measurement of Joule loss would be compromised.

To address this problem and achieve a much more reliable model, certain modifications have been made to the design. The modifications have been applied to both the software. The shape of the stator slots has been altered to host the stator windings, and each slot now contains four rectangular conductors that simulate the implementation of hairpin technology coils.

Figure 3.10 illustrates the comparison between the initial model and the one which has been improved.

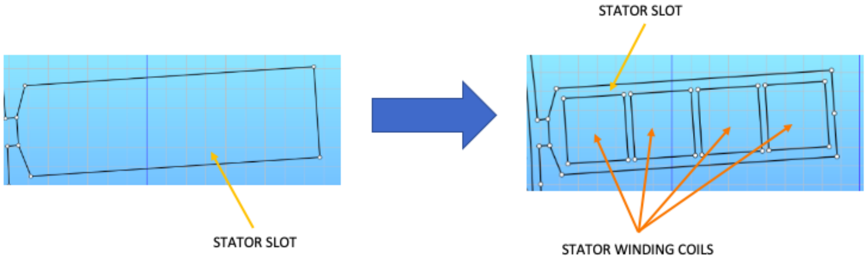

Figure 3.10: Comparison between the model without windings (left) and the one with windings (right)

The updated layout of the motor model enables the distinction of the excitation of the two parallel coils that form the windings.

This feature of the windings becomes particularly significant when non-sinusoidal excitation is applied to the coils. In a motor with 2Y windings, the parallel branches of the windings play a crucial role in mitigating second-order harmonics in the current. Thanks to the symmetry of the windings, the second-order harmonics in the current tend to cancel each other out. The magnetic fields generated by the parallel branches interact in a manner that reduces the second-order harmonic components, as well.

The model utilized for this research activity is excited by only sinusoidal currents. However, a potential future step is to expand the scope by incorporating a complete drive unit, which includes the battery and the inverter. When an inverter is introduced to the model, it becomes the source of second-order harmonics that alter the shape of the nominal sinusoidal current.

The improved model would be able to capture, analyze and most importantly mitigate the impact of these harmonics. This would enable the designer to develop appropriate control strategies to address them effectively.

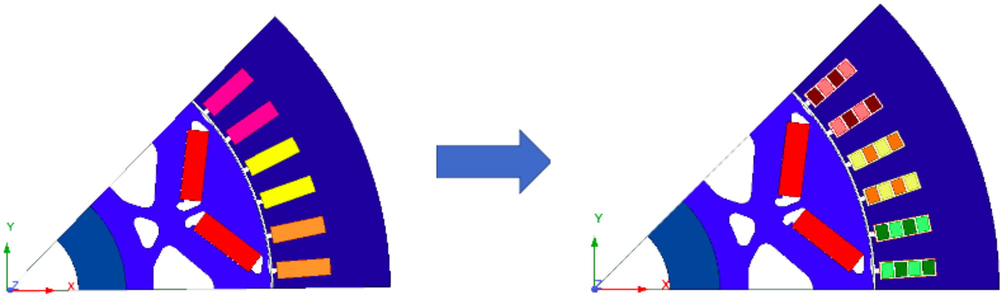

Figure 3.11: Comparison of starting motor layout (left) and improved motor layout (right)

3.3 Simulation setup

Running an electromagnetic simulation involves a series of steps to accurately model and analyze the behavior of electromagnetic fields in a device, as an electric motor. These steps ensure that the simulation captures the essential characteristics of the electromagnetic field variation in the overall system. The goal is to achieve the most accurate reproduction of the motor's actual behavior, so each stage of the simulation setup aims to closely mimic the real-world conditions.

The starting point is the description of the boundaries and of the material properties of the model.

Afterwards, the focus moves to the development of the external circuit that feeds the stator windings and the meshing procedure. Finally, the time settings are outlined and it is possible to proceed with the simulation. In the upcoming sections, each phase of the simulation setup will be analyzed in details. The two software implement the same steps, with a different order. For sake of simplicity, in the next sections, the procedure will be illustrated once.

3.3.1 Implementation of Boundary Conditions

Boundary conditions play a crucial role in determining how the electric or magnetic field behaves at the interfaces or edges of the problem region. They are always necessary in order to ensure the uniqueness of the electromagnetic field calculation.
In electric motors, the boundary conditions serve two main purposes:

- Set the electric or magnetic potential at a surface to a constant value or a function of position, in order to define the behavior of the electric or magnetic field on that surface.
- Simulate the field patterns that would exist in a structure, while modeling only part of it.

For this case study, the boundary conditions applied are:

1. *Vector potential:* It is also know as Dirichlet boundary and it is applied to the stator outer surface, to set a null magnetic potential in correspondence of it.

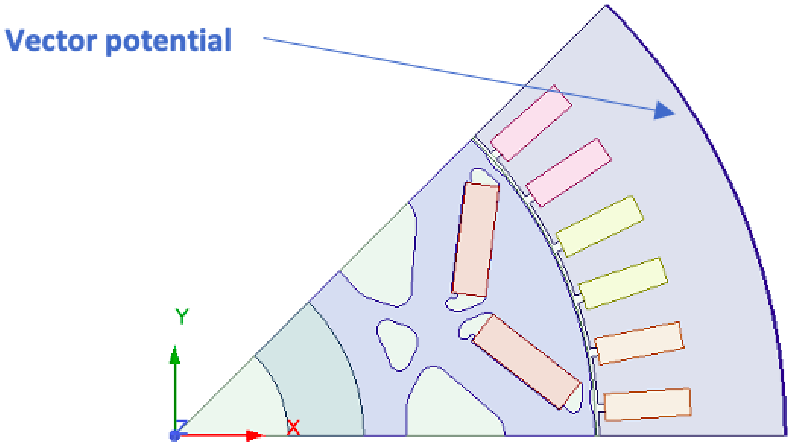

Figure 3.12: Dirichlet boundary

2. *Independent/Dependent Matching:* Matching boundaries force the magnetic field at each point on one boundary (the "dependent" boundary) to match the magnetic field at each corresponding point on the other surface (the "independent" boundary).

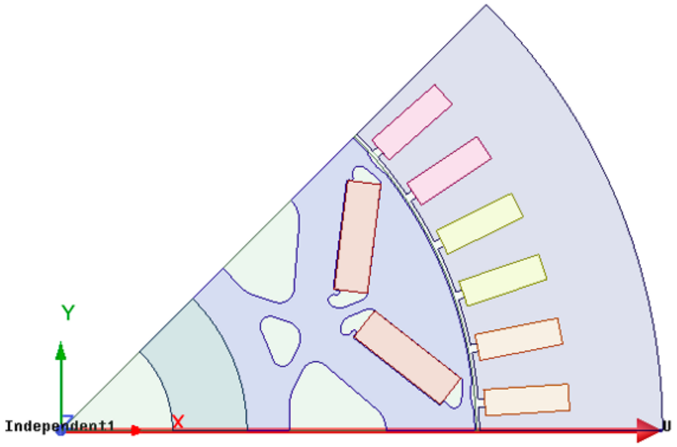

Figure 3.13: Independent boundary

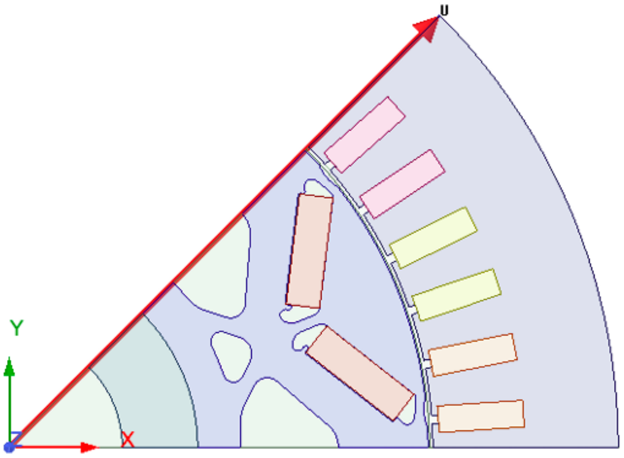

Figure 3.14: Dependent boundary

3.3.2 Definition of Material Properties

Assigning appropriate material properties is crucial for an accurate simulation. It is needed to define the electromagnetic properties of different materials present in your system, such as stator windings conductivity, magnetic permeability of stator and iron core, and dielectric constants of the insulating materials. These properties determine how materials interact with electromagnetic fields and the outcome of the electromagnetic simulation is strongly influenced by each of these parameters. Thus, the data collecting phase (from literature review and from the suppliers) is of significant importance to achieve correct results.

3.3.3 Development and Coupling of the External Circuit

The current flowing into the stator windings generates a rotating magnetic field, which interacts with the rotor magnetic field to develop the required torque in correspondence of the air gap. To have a proper replication in a virtual environment of the stator windings configuration, an external circuit must be added and coupled to the motor model. The external circuit consists of the three motor phases arranged together. The resistive effect given by the end windings can be modeled as a simple resistance, while the portion of the conductors located in the slots is modeled as a winding. Figure 3.15 depicts the details of the winding configuration.

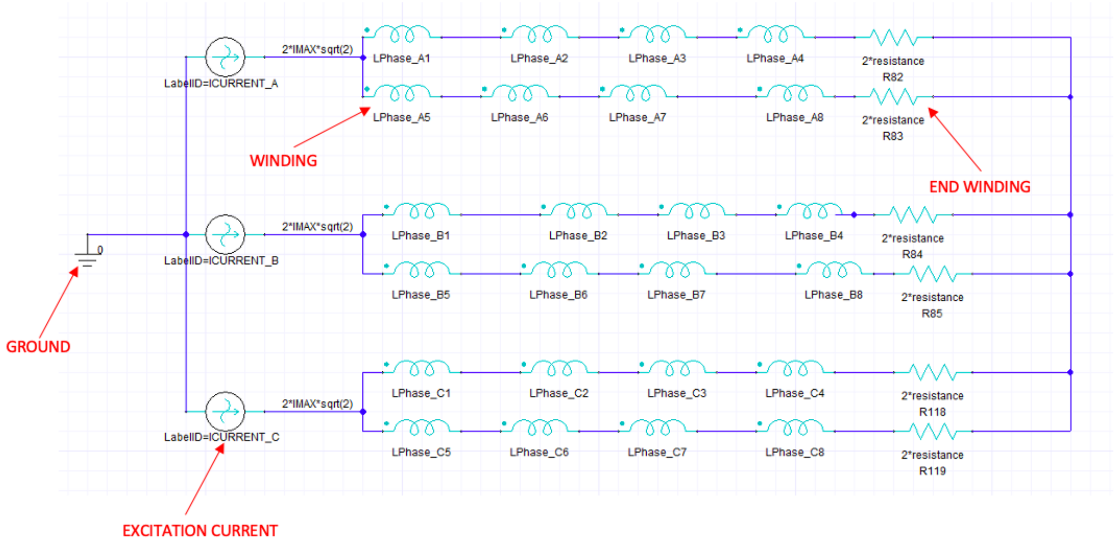

Figure 3.15: External excitation circuit, developed with ANSYS Maxwell™

$LPhase\_A1$ ... $LPhase\_C8$ represent the active part of the windings, whereas $R82$, $R83$, $R84$, $R85$, $R118$ and $R119$ are the end windings for each of the conductors. $LabelID = ICURRENT\_A$, $LabelID = ICURRENT\_B$ and $LabelID = ICURRENT\_C$ are the sinusoidal current sources for each phase.

3.3.4 Application of Meshes

The implementation of the motor model has been identical between the two software platforms up to the meshing phase. The primary objective is to evaluate the quantitative improvements in results achieved by utilizing denser meshes in Altair Flux™, compared to the lower mesh density utilized in ANSYS Maxwell™ . Additionally, the impact on computational time resulting from transitioning between the two meshing approaches will be assessed.

In both software platforms, an automatic meshing procedure has been employed. Second order meshes are utilized, with a particular focus on higher mesh density at interfaces between different materials, where significant variations in the magnetic field distribution are expected. Additionally, careful analysis is conducted on the stator slot and windings, as these regions are susceptible to Joule loss-induced overtemperature. The resulting meshing is characterized by some regions with a different meshing density in both softwares. Increasing the mesh density in Altair Flux™ leads to a noticeable slowdown in simulation time compared to using ANSYS Maxwell™. At peak speed, the software ANSYS Maxwell™ achieves simulation times within a few minutes, while simulations conducted in Altair Flux extend above 30 minutes.

In the upcoming figures, a representation of the motor geometry, which has been meshed using both software, is given.

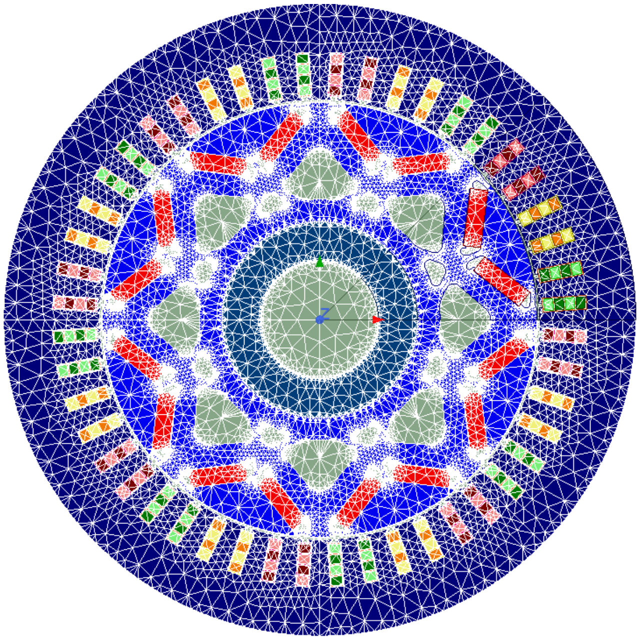

Figure 3.16: Complete motor geometry meshed in ANSYS Maxwell™

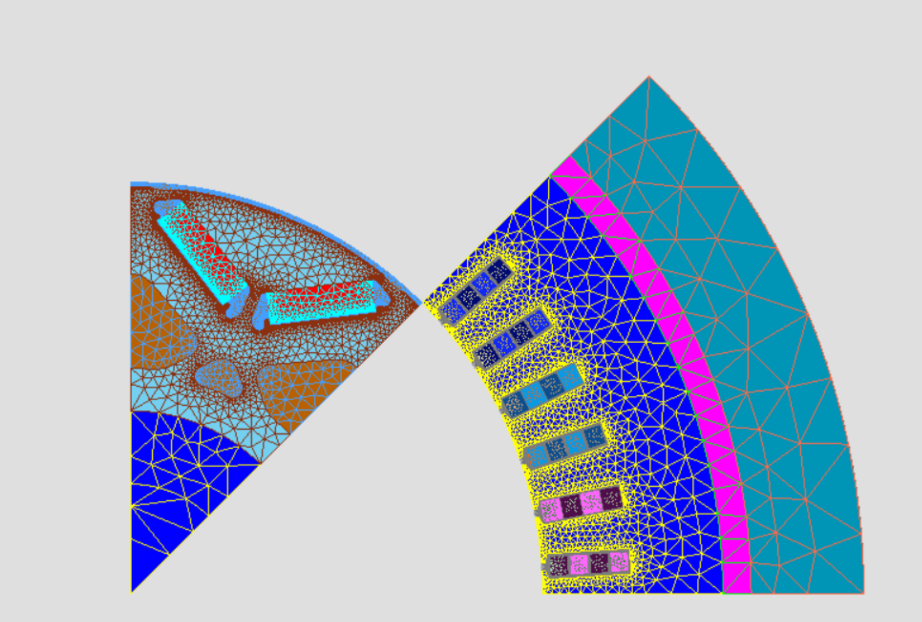

Figure 3.17: Partial motor geometry meshed in Altair Flux™

3.3.5 Loading and Time Setting

Before proceeding with the analysis, the loading conditions of the system and the time interval for the simulation need to be established. Selecting an appropriate time step is crucial as it enables the computation of the actual variations in the magnetic or electrical quantities within the system, resulting in accurate results.

In this particular case study, the choice of time step and stop time is dependent on the motor's speed. This ensures that the analysis reaches the steady-state conditions necessary for evaluating the losses in the electric motor and constructing the efficiency map.

3.4 Validation Test

To assess the model's compatibility with reality, a validation test has been proposed. It involves replicating a back electromotive force (b-emf) test in a virtual environment. The parameter under comparison with experimental results is the back-emf motor constant. In the simulations, the induced voltage at the stator windings is measured to determine this parameter.

3.4.1 Back Electromotive Force Test

Prior to conducting efficiency evaluation tests, a back electromotive force test was performed on the motor for validation. This test aims to detect issues related to the rotor, magnets, or any angle misalignments. It involves measuring the induced voltage generated between the motor's terminals while it is rotated by an external drive. By analyzing the voltage in the time domain for each phase, the b-emf constant K_e can be determined [51].

$$K_e = \frac{V_{ll,rms}}{\omega} \tag{3.4.1}$$

where $V_{ll,rms}$ is the line to line motor voltage, expressed as root mean square value. Whereas ω is the electric motor angular speed.

In experimental testing, the motor is rotated at a specific operating speed, and the voltage generated across the three phases is measured using a digitizer. Since the neutral point is typically inaccessible, the line-to-line voltage is often used. In a virtual environment, the test can be replicated by setting the excitation current to 0 and imposing the desired operating speed of the motor. This will induce a voltage that can be detected and plotted using software tools.

The test was conducted by setting the operating temperature of the magnets to 100 °C, while the temperature of the windings, rotor, and stator was maintained at standard conditions. The induced voltage was measured at various speeds. The experimental results were then compared to the simulated results in terms of root mean square of the line-to-line voltage and K_e constant.

3.5 Steady-State Performance Test

A fixed-speed performance test is an experimental test conducted on an electric motor to evaluate its performance under a specific constant operating condition. During the test, the motor is operated at specific torque and current values that are set as input parameters.

The main objective of a fixed-speed performance test is to characterize the performance of the electric motor in terms of variables such as rotational speed, generated torque, efficiency, and power losses. These parameters provide important information about the motor's ability to perform a particular task or specific application.

During the test, experimental data such as voltage, current, speed, and torque of the motor are collected. This data is then analyzed to determine the actual performance of the electric motor, including efficiency, power absorbed, output power, and other relevant quantities.

By replicating a steady-state performance test in a virtual environment, engineers can assess and analyze the motor's behavior without the need for physical prototypes or experimental setups. This approach provides a cost-effective and efficient way to study different operating conditions, optimize motor designs, and predict performance characteristics.

3.6 Post Processing

From the two software, it is possible to exctract three key output quantities: the distribution of current in the windings, core losses, and the output torque. The simulations delve into the variations of the magnetic field across the different motor components, enabling the calculation of iron losses in the core materials. By examining the current source defined in the excitation circuit, the extent of Joule losses can be determined. Additionally, the software ANSYS Maxwell™ allow for the quantification of the proximity effect between conductors and the impact of higher operating frequencies. The interaction between the magnetic field generated by the stator and the magnetic field produced by the rotor's permanent magnet results in the development of electromagnetic torque. Both software tools are capable of accurately quantifying this torque. With knowledge of the motor's operating speed, the output power produced by the motor can be calculated.

Some crucial information is still missing to accurately assess the efficiency of the motor under different operating conditions. The loss models for mechanical and ohmic power dissipation, described in the previous sections, cannot be directly employed in the software. This is due to the limitation of the software in assigning a fixed value to the copper resistance, whereas experimental findings have shown that the resistance is significantly influenced by the operating frequency of the current. To address this problem and calculate the efficiency map, a post-processing MATLAB code has been developed.

3.6.1 MATLAB code for post processing

A MATLAB™ code has been developed specifically for post-processing the simulation results [50]. This code facilitates the calculation of efficiency for each operating condition. Additionally, the code has been designed to quantify individual losses and map them accordingly, providing a comprehensive representation of the distribution of losses.

The algorithm can be divided into the following sections:

1. *Building the efficiency and loss maps:* This involves allocating the experimental and simulated results into the maps. A total of 660 combinations of torque/speed points are considered in the maps.

2. *Reading and extracting information from the Excel file:* The MATLAB™ code is designed to read and extract the simulation results from the provided Excel files. The extracted data is stored in tables, which will be used for computing the efficiency map.

3. *Processing the extracted data:* This section involves evaluating the efficiency for each operating point. The output power and core loss are summed with the joule loss and mechanical loss computed within the code to obtain the input torque. The ratio of input power to output power determines the efficiency for each operating point. Additionally, the algorithm evaluates the weight of each loss component for every operating point, allowing for identification and mitigation of the most influential loss on motor efficiency.

4. *Allocating the evaluated data to the appropriate positions in the maps:* The algorithm assigns each of the previously evaluated data to their corresponding positions in the efficiency and loss maps.

5. *Developing graphical representations of the efficiency and loss maps:* Once all the input data has been processed, the code automatically generates an efficiency plot as well as a plot showing the core and joule losses. These visual representations provide a clear visualization of the efficiency and loss distribution.

Figure 3.18 illustrates the step-by-step process for conducting a simulation. The input data, provided by an OEM, includes the motor's operating speed and the current magnitude expressed as a sum of direct and quadrature axis components. These data are inputted into the model developed within the virtual environment of the two software. The simulation is then executed, producing outputs such as current, electromagnetic torque, and core loss. These outputs are subsequently fed into the MATLAB™ program. Finally, the code generates the desired results, namely the efficiency and loss maps.

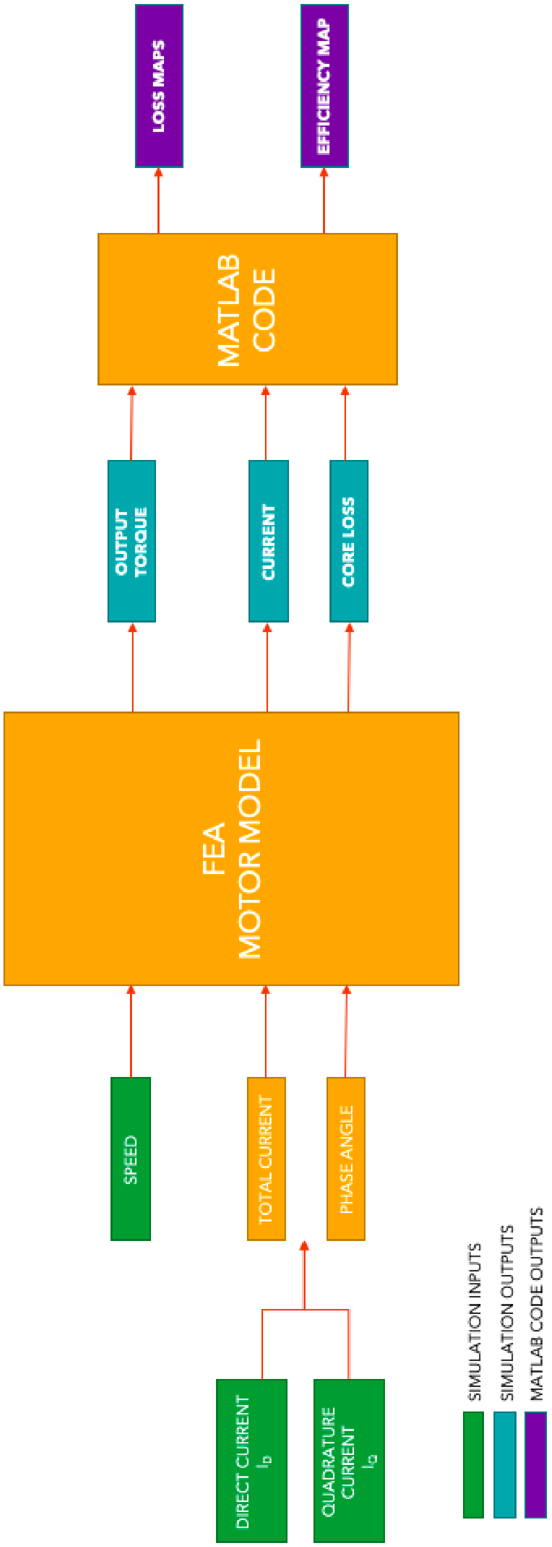

Figure 3.18: Illustrative representation of the simulation workflow

Chapter 4

Simulation Results

The primary objective of this research project is to recreate an electric motor in a virtual environment and explore the disparities between reality and simulations. Striking the right balance between model accuracy and computational efficiency is crucial, as excessively detailed analysis could significantly increase computational time. To achieve an appropriate motor model, a validation test was replicated in the virtual environment before proceeding to simulate the efficiency.

The subsequent chapter presents the simulation results, from the validation test outcomes to the evaluation of the motor losses and the efficiency map. These outputs, obtained from the simulations and processed using Matlab code, will then be compared to the experimental findings.

The data provided by the OEM does not exhibit any uncertainty analysis. Consequently, the simulated values capture details down to two decimal places.

4.1 Validation Test Outcomes

In this section, the outcomes of the back electromotive force test will be discussed. The focus will be the induced voltage in the stator windings. By examining the induced voltage, it is possible to determine the b-emf motor constant at different operating speeds and compare it with the correspondent experimental value.

4.1.1 Back Electromotive Force Test Outcomes

The b-emf test results are presented in relation to the voltage induced in the stator windings. Figure 4.1 illustrates the waveform generated at 0.0071 per unit (pu) speed, with an estimated peak value of 16.98 V.

The company has provided data regarding the root mean square value of the induced voltage curve. By analyzing the simulation results developed with ANSYS Maxwell™, it is possible to calculate the induced voltage and compare it with the experimental findings. Figure 4.2 proves that the simulated curve closely aligns with the experimental one, except for the operating point of 0.857 pu speed. At this particular point, the actual behavior exhibits an abnormal discrepancy compared to the simulation as well as all other experimental values.

Figure 4.1: Induced voltage at the stator windings.

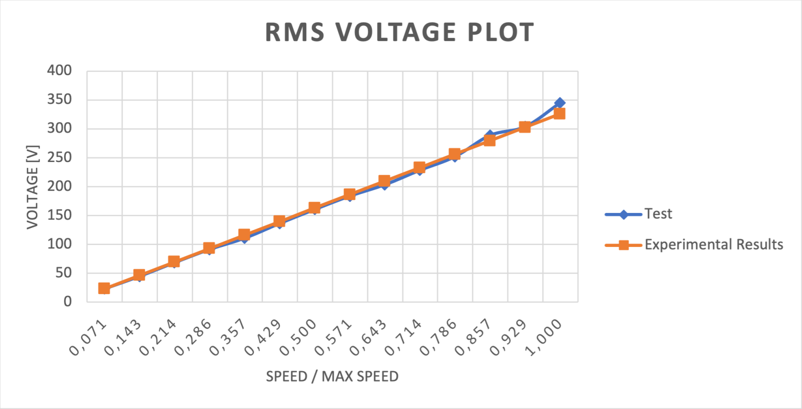

Figure 4.2: Variation of RMS induced voltage with different operating speeds.

Beyond this point, the trend shifts towards overestimating the experimental rms value of the induced voltage. The approximation error is confined to a maximum of 5 %, with the most significant deviation occurring at 0.357 pu speed. At this speed, the absolute difference between the experimental and simulated results amounts to 5 V, corresponding to a percentage error of -4.99 %. In Figure 4.3 plotting the error as a function of the operating speed, a clearer understanding of the simulated voltage trend relative to the actual behavior can be obtained. Table 4.1 presents the induced voltage values at different operating speeds and the percentage error in the approximation.

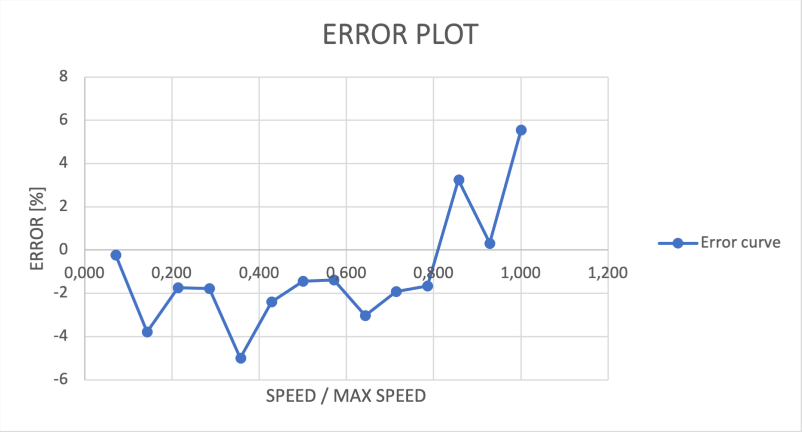

Figure 4.3: Error plot versus the normalized speed.

Table 4.1: Voltage and Error Data

Speed	$V_{\text{RMS\_simulation}}$	$V_{\text{LL\_RMS\_simulation}}$	$V_{\text{LL\_RMS\_experimental}}$	Error [%]	$K_{\text{e\_simulation}}$ [mV/rpm]
0.071	13.42	23.25	23.30	-0.22	23.25
0.143	25.92	44.90	46.60	-3.79	22.45
0.214	39.67	68.71	69.91	-1.74	22.90
0.286	52.87	91.58	93.21	-1.77	22.89
0.357	64.07	110.97	116.51	-4.99	22.19
0.429	78.83	136.54	139.82	-2.40	22.75
0.500	92.84	160.81	163.12	-1.43	22.97
0.571	106.15	183.87	186.42	-1.39	22.98
0.643	117.51	203.54	209.73	-3.03	22.61
0.714	132.00	228.64	233.03	-1.91	22.86
0.786	145.58	252.15	256.34	-1.66	22.92
0.857	166.85	288.99	279.64	3.23	24.08
0.929	175.45	303.90	302.94	0.31	23.37
1.000	199.40	345.38	326.25	5.53	24.67

4.2 Loss Maps

The next section focuses on evaluating the losses of the electric motors, specifically categorizing them as Joule, core and mechanical losses. The Joule and mechanical losses have been calculated in MATLAB™ using speed and current data obtained from the simulations conducted in both software programs. On the other hand, the core losses are directly assessed within the software environment and then assigned to specific torque/speed combinations in MATLAB™.

4.2.1 Joule Loss Map

Joule losses refer to the power dissipation in the stator windings when current flows through them. It is expected that Joule losses will increase with higher operative torque, as a higher current is required. Increasing operative speed, a variation in current distribution, thus an increment in stator winding resistance is induced. In this section, the evaluation of Joule losses in Altair Flux™ and ANSYS Maxwell™ will be discussed separately to highlight the differences in current distribution and loss evaluation between the two software programs.

Figures 4.4 and 4.5 illustrate the joule losses under various operating conditions. Distinct regions can be identified in the plot, distinguished by varying levels of losses, represented by different colors. The color scale ranges from dark blue, indicating very low Joule losses, to yellow, indicating higher losses. These regions exhibit an oblique extension, illustrating that as the speed increases, the Joule losses also increase. By examining the scale, it is possible to notice the significant disparities between the two software. For the software ANSYS Maxwell™, the peak value of the scale is 8000 W, whereas in Altair Flux, it is 3000 W higher.

ANSYS Maxwell™

The Joule loss map, generated through MATLAB™ by postprocessing ANSYS Maxwell™ results, is presented in Table 4.2.

In the constant torque region, the Joule loss exhibits a relatively low dependence on operating speed since the current supplied remains nearly constant at different operating speeds. The only parameter inducing variations in the loss is the frequency-dependent resistance. At peak torque and base speed, the Joule loss reaches its maximum value of 6792.11 W. In the constant power region, the Joule loss increases rapidly. This escalation is a result of both the increasing current magnitude and resistance, influenced by the frequency. For example, when considering the same torque request of 0.25 pu, the Joule losses evaluated at speeds of 0.571 pu, 0.643 pu, and 0.714 pu amount to 222.6 W, 365.85 W, and 673.76 W, respectively. This represents a 39% increase from the first to the second operating speed, and nearly doubles from the second to the third speed analyzed.

As anticipated, the loss increases significantly with higher currents, which holds true for each operating speed. The loss increases nearly 120-fold from the lowest torque to the peak torque at 0.071 pu speed. The Joule losses nearly double from the lowest analyzed speed to the maximum speed, referring to peak torque conditions. In absolute values, this increase ranges from 4780.17 W at peak torque and 0.018 pu speed to 8586.11 W at maximum speed and maximum torque. To illustrate the impact of frequency on Joule losses, the loss at 0.086 pu torque while increasing the speed can be analyzed. The Joule loss escalates from 37.5 W at the lowest considered speed to 1940.23 W at maximum speed.

Altair Flux™

The Joule loss map obtained through MATLAB™ postprocessing of Altair Flux™ outcomes is depicted in Table 4.3.

In the constant torque region, the joule loss escalates in proportion to the current. A notable difference from ANSYS Maxwell™ is observed in the base speed joule loss, where the registered value reaches 7543.59 W compared to ANSYS Maxwell's 6792.11 W. The variation of Joule loss at different speeds further contributes to the disparity between the two software programs. Table 4.3 demonstrates that at peak torque, there is an increase of nearly 1000 W in Joule losses when transitioning from 0.143 pu to 0.214 pu speed and from 0.214 pu to 0.286 pu speed. In contrast, ANSYS Maxwell™ exhibits a difference of approximately 600 W within the same speed interval. Moving to the constant power region, the Joule losses experience a significant increase. Values exceeding 8000 W are registered at peak torque conditions starting from 0.357 pu speed. In this region, the Joule loss escalates substantially with the increase in torque request. For instance, at 0.643 pu speed, the Joule losses increase from 224.47 W at a torque demand of 0.068 pu to 10639.08 W at a torque demand of 0.568 pu.

The software exhibits consistent behavior in line with experimental results: the loss increases with higher torque demand and operating speed. At low operating speeds, the operating current becomes the primary influencing factor, resulting in a more than 100-fold increase in loss at 0.036 pu speed. The peak loss is observed at maximum speed and peak power, amounting to 13390.13 W.

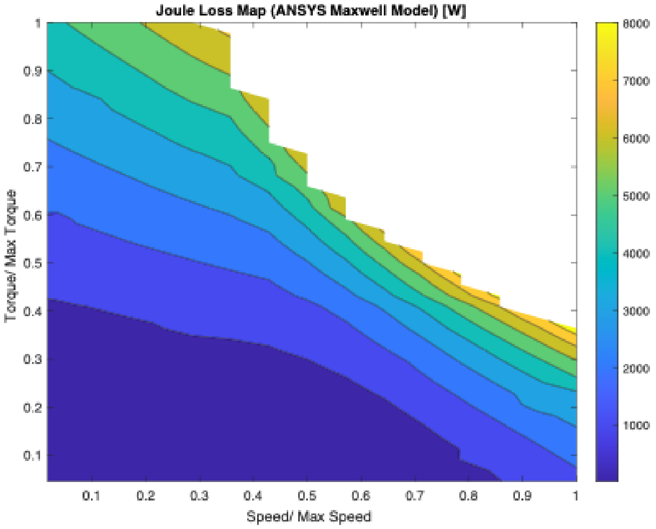

Figure 4.4: Graphic representation of the Joule loss map developed with MATLAB, postprocessing ANSYS Maxwell™ results.

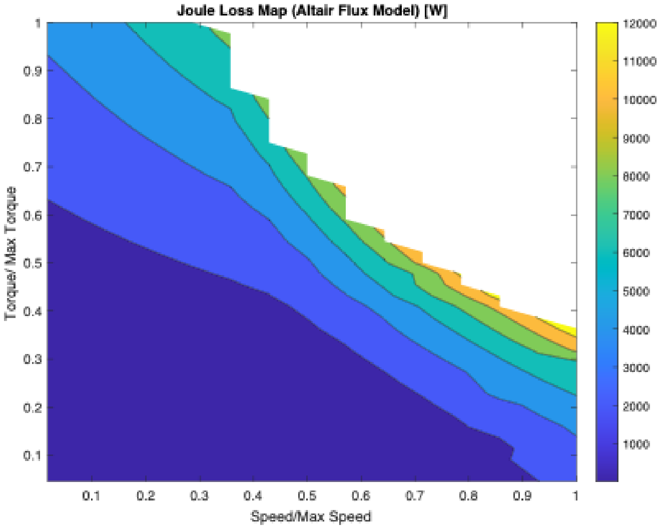

Figure 4.5: Graphic representation of the Joule loss map developed with MATLAB, postprocessing Altair Flux™ results.

JOULE LOSS MAP [W]																	
		Speed/ Max Speed															
		0,02	0,04	0,07	0,14	0,21	0,29	0,36	0,43	0,50	0,57	0,64	0,71	0,79	0,86	0,93	1,00
Torque/ Max Torque	1,00	4780,17	4895,88	5134,90	5643,92	6195,80	6792,11										
	0,98	4600,04	4711,71	4941,41	5430,98	5961,14	6532,71	7100,92									
	0,95	4421,59	4528,95	4749,67	5219,63	5728,26	6276,21	6795,29									
	0,93	4244,81	4347,77	4559,57	5010,31	5497,41	6022,40	6520,56									
	0,91	4069,70	4168,53	4371,46	4802,88	5268,55	5770,49	6236,39									
	0,89	3906,37	4000,97	4195,24	4607,91	5053,47	5316,15	5951,47									
	0,86	3755,43	3846,13	4032,53	4428,49	4855,74	5316,15	5686,71									
	0,84	3585,08	3671,73	3849,39	4226,47	4633,30	5071,58	5423,87	6992,72								
	0,82	3417,10	3499,49	3668,78	4027,41	4413,84	4824,30	5161,04	6576,46								
	0,80	3252,28	3330,62	3491,35	3831,84	4198,27	4592,38	4916,65	6185,59								
	0,77	3093,87	3168,19	3320,69	3643,15	3989,81	4362,49	4665,30	5854,37								
	0,75	2950,39	3021,17	3166,26	3472,98	3802,67	4157,32	4432,44	5437,34								
	0,73	2791,55	2858,44	2995,38	3284,83	3612,87	3929,27	4204,81	5146,75	6868,05							
	0,70	2636,34	2699,41	2828,54	3101,07	3333,17	3706,62	4026,09	4777,42	6357,39							
	0,68	2483,63	2542,81	2664,10	2919,90	3193,78	3487,81	3802,51	4777,43	5919,22							
	0,66	2348,28	2404,03	2518,22	2758,30	3016,54	3292,72	3587,85	4156,58	5463,78							
	0,64	2202,76	2254,92	2361,78	2586,41	2827,49	3085,48	3360,99	3871,91	5046,72	6886,98						
	0,61	2059,35	2108,13	2207,76	2416,76	2641,18	2881,07	3137,32	3576,42	4640,20	6886,98						
	0,59	1918,97	1827,23	2056,76	2250,71	2458,72	2680,91	2917,10	3315,52	4247,68	5748,16						
	0,57	1785,30	1827,08	1912,92	2092,48	2284,93	2490,23	2708,36	3042,75	3927,91	5219,10	7183,87					
	0,55	1660,94	1699,64	1779,24	1945,65	2123,86	2314,00	2515,94	2796,57	3576,94	4727,98	6449,58					
	0,52	1531,26	1566,80	1639,92	1792,64	1956,13	2130,43	2315,31	2550,12	3265,09	4290,82	5792,69	7865,37				
	0,50	1405,74	1440,38	1505,05	1644,58	1793,74	1953,24	2121,62	2329,27	2950,97	3865,22	5218,92	6990,81				
	0,48	1284,34	1314,10	1374,47	1501,78	1637,37	1781,86	1935,01	2109,40	2649,87	3477,21	4676,25	6184,03	8284,15			
	0,45	1175,36	1202,54	1257,62	1373,36	1496,95	1628,28	1767,82	1910,07	2396,45	3102,75	4170,79	5557,31	7290,67			
	0,43	1062,62	1087,00	1136,85	1240,75	1351,92	1470,03	1595,48	1717,14	2134,24	2755,26	3706,66	4948,21	6475,38	8360,58		
	0,41	829,59	881,23	975,31	1064,11	1158,76	1259,59	1366,32	1462,74	1802,42	2331,49	3132,77	4167,79	5474,90	6997,73		
	0,39	829,51	848,22	886,12	967,09	1052,94	1144,06	1318,80	1319,42	1613,21	2078,46	2792,49	3685,57	4901,51	6198,91	7780,28	
	0,36	748,08	764,91	798,88	871,66	948,79	1144,06	1105,48	1185,26	1441,45	1844,73	2485,49	3318,21	4364,56	5501,87	6856,92	8586,11
	0,34	669,43	684,24	714,56	779,32	847,83	920,71	997,99	1064,83	1271,10	1633,00	2196,83	2942,46	3850,57	4906,77	6099,47	7541,01
	0,32	526,07	611,42	638,32	695,85	755,07	821,48	887,15	955,06	1117,10	1433,07	1941,36	2598,19	3425,06	4356,12	5445,95	6687,59
	0,30	526,07	537,47	560,87	610,96	662,44	720,43	777,39	841,40	972,29	1239,97	1683,67	2217,98	3062,28	3904,53	4822,47	5934,52
	0,27	457,21	467,03	487,12	530,15	574,34	624,31	673,13	730,06	833,00	1071,43	1462,96	2032,78	2723,60	3440,29	4345,78	5246,00
	0,25	335,04	403,27	420,42	457,13	494,93	536,26	579,40	625,76	703,10	909,18	1261,76	1789,69	2400,00	3089,64	3854,01	4709,24
	0,23	335,04	342,03	356,37	387,03	418,71	453,32	489,37	528,31	587,03	756,44	1072,94	1550,04	2107,23	2745,27	3398,61	3773,58
	0,20	281,06	286,83	298,75	323,99	350,47	379,15	409,21	441,51	480,03	639,50	897,33	1330,14	1870,52	2410,79	3411,10	3758,18
	0,18	221,35	233,10	242,65	263,00	284,40	307,48	331,77	357,89	388,45	504,48	740,17	1125,47	1641,09	2132,48	2734,16	3341,15
	0,16	179,47	183,10	190,52	206,38	223,19	241,32	260,37	280,49	301,13	398,67	597,05	955,03	1406,18	1889,84	2424,67	3007,24
	0,14	135,65	138,39	143,85	155,96	168,71	182,46	196,90	212,15	229,28	302,69	473,42	800,88	1204,39	1660,63	2140,04	2683,34
	0,11	98,01	100,01	106,21	112,72	121,98	131,93	142,42	153,52	166,65	222,60	365,85	673,76	1019,64	1448,00	1907,35	2395,56
	0,09	65,73	67,06	69,82	75,65	81,93	88,67	95,82	103,35	111,38	144,93	279,07	545,25	880,35	1260,25	1694,13	2156,51
	0,07	37,50	38,45	39,85	43,24	46,89	50,83	55,00	59,41	65,46	86,49	205,73	441,20	742,93	1099,08	1504,22	1940,24

Table 4.2: Joule loss map developed with MATLAB™, postprocessing ANSYS Maxwell™ results.

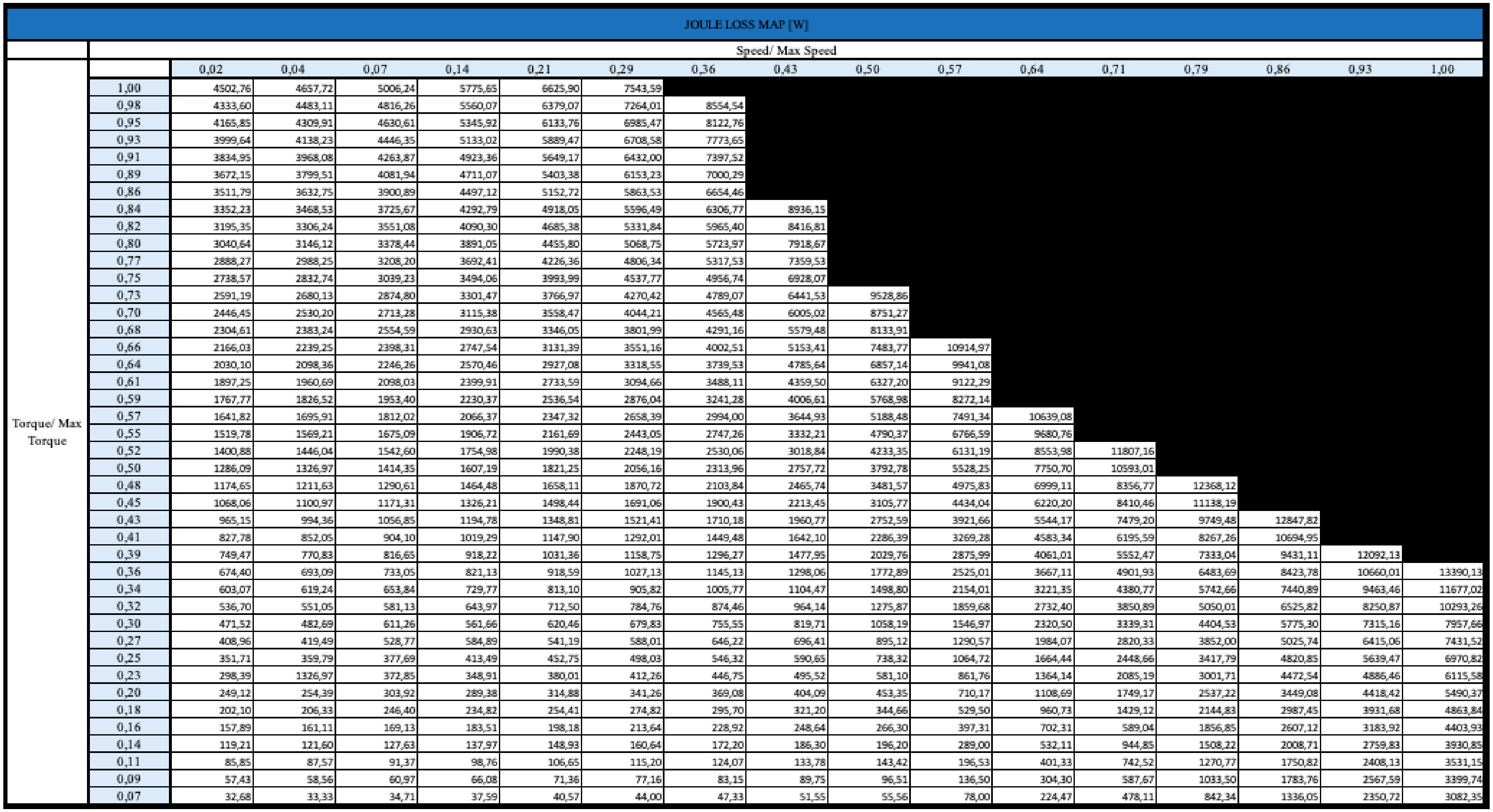

JOULE LOSS MAP [W]

		Speed/ Max Speed															
		0,02	0,04	0,07	0,14	0,21	0,29	0,36	0,43	0,50	0,57	0,64	0,71	0,79	0,86	0,93	1,00
Torque/ Max Torque	1,00	4502,76	4657,72	5006,24	5775,65	6625,90	7543,59										
	0,98	4333,60	4483,11	4816,26	5560,07	6379,07	7264,01	8554,54									
	0,95	4165,85	4309,91	4630,61	5345,92	6133,76	6985,47	8122,76									
	0,93	3999,64	4138,23	4446,35	5133,02	5889,47	6708,58	7773,65									
	0,91	3834,95	3968,08	4263,87	4923,36	5649,17	6432,00	7397,52									
	0,89	3672,15	3799,51	4081,94	4711,07	5403,38	6153,23	7000,29									
	0,86	3511,79	3632,75	3900,89	4497,12	5152,72	5863,53	6654,46									
	0,84	3352,23	3468,53	3725,67	4292,79	4918,05	5596,49	6306,77	8936,15								
	0,82	3195,35	3306,24	3551,08	4090,30	4685,38	5331,84	5965,40	8416,81								
	0,80	3040,64	3146,12	3378,44	3891,05	4455,80	5068,75	5723,97	7918,67								
	0,77	2888,27	2988,25	3208,20	3692,41	4226,36	4806,34	5317,53	7359,53								
	0,75	2738,57	2832,74	3039,23	3494,06	3993,99	4537,77	4956,74	6928,07								
	0,73	2591,19	2680,13	2874,80	3301,47	3766,97	4270,42	4789,07	6441,53	9528,86							
	0,70	2446,45	2530,20	2713,28	3115,38	3558,47	4044,21	4565,48	6005,02	8751,27							
	0,68	2304,61	2383,24	2554,59	2930,63	3346,05	3801,99	4291,16	5579,48	8133,91							
	0,66	2166,03	2239,25	2398,31	2747,54	3131,39	3551,16	4002,51	5153,41	7483,77	10914,97						
	0,64	2030,10	2098,36	2246,26	2570,46	2927,08	3318,55	3739,53	4785,64	6857,14	9941,08						
	0,61	1897,25	1960,69	2098,03	2399,91	2733,59	3094,66	3488,11	4359,50	6327,20	9122,29						
	0,59	1767,77	1826,52	1953,40	2230,37	2536,54	2876,04	3241,28	4006,61	5768,98	8272,14						
	0,57	1641,82	1695,91	1812,02	2066,37	2347,32	2658,39	2994,00	3644,93	5188,48	7491,34	10639,08					
	0,55	1519,78	1569,21	1675,09	1906,72	2161,69	2443,05	2747,26	3332,21	4790,37	6766,59	9680,76					
	0,52	1400,88	1446,04	1542,60	1754,98	1990,38	2248,19	2530,06	3018,84	4233,35	6131,19	8553,98	11807,16				
	0,50	1286,09	1326,97	1414,35	1607,19	1821,25	2056,16	2313,96	2757,72	3792,78	5528,25	7750,70	10593,01				
	0,48	1174,65	1211,63	1290,61	1464,48	1658,11	1870,72	2103,84	2465,74	3481,57	4975,83	6999,11	8356,77	12368,12			
	0,45	1068,06	1100,97	1171,31	1326,21	1498,44	1691,06	1900,43	2213,45	3105,77	4434,04	6220,20	8410,46	11138,19			
	0,43	965,15	994,36	1056,85	1194,78	1348,81	1521,41	1710,18	1960,77	2752,59	3921,66	5544,17	7479,20	9749,48	12847,82		
	0,41	827,78	852,05	904,10	1019,29	1147,90	1292,01	1449,48	1642,10	2286,39	3269,28	4583,34	6195,59	8267,26	10694,95		
	0,39	749,47	770,83	816,65	918,22	1031,36	1158,75	1296,27	1477,95	2029,76	2875,99	4061,01	5552,47	7333,04	9431,11	12092,13	
	0,36	674,40	693,09	733,05	821,13	918,59	1027,13	1145,13	1298,06	1772,89	2525,01	3667,11	4901,93	6483,69	8423,78	10660,01	13390,13
	0,34	603,07	619,24	653,84	729,77	813,10	905,82	1005,77	1104,47	1498,80	2154,01	3221,35	4380,77	5742,66	7440,89	9463,46	11677,02
	0,32	536,70	551,05	581,13	643,97	712,50	784,76	874,46	964,14	1275,87	1859,68	2732,40	3850,89	5050,01	6525,82	8250,87	10293,26
	0,30	471,52	482,69	611,26	561,66	620,46	679,83	755,55	819,71	1058,19	1546,97	2320,50	3339,31	4404,53	5775,30	7315,16	7957,66
	0,27	408,96	419,49	528,77	584,89	541,19	588,01	646,22	696,41	895,12	1290,57	1984,07	2820,33	3852,00	5025,74	6415,06	7431,52
	0,25	351,71	359,79	377,69	413,49	452,75	498,03	546,32	590,65	738,32	1064,72	1664,44	2448,66	3417,79	4820,85	5639,47	6970,82
	0,23	298,39	1326,97	372,85	348,91	380,01	412,26	446,75	495,52	581,10	861,76	1364,14	2085,19	3001,71	4472,54	4886,46	6115,58
	0,20	249,12	254,39	303,92	289,38	314,88	341,26	369,08	404,09	453,35	710,17	1108,69	1749,17	2537,22	3449,08	4418,42	5490,37
	0,18	202,10	206,33	246,40	234,82	254,41	274,82	295,70	321,20	344,66	529,50	960,73	1429,12	2144,83	2987,45	3931,68	4863,84
	0,16	157,89	161,11	169,13	183,51	198,18	213,64	228,92	248,64	266,30	397,31	702,31	589,04	1856,85	2607,12	3183,92	4403,93
	0,14	119,21	121,60	127,63	137,97	148,93	160,64	172,20	186,30	196,20	289,00	532,11	944,85	1508,22	2008,71	2759,83	3930,85
	0,11	85,85	87,57	91,37	98,76	106,65	115,20	124,07	133,78	143,42	196,53	401,33	742,52	1270,77	1750,82	2408,13	3531,15
	0,09	57,43	58,56	60,97	66,08	71,36	77,16	83,15	89,75	96,51	136,50	304,30	587,67	1033,50	1783,76	2567,59	3399,74
	0,07	32,68	33,33	34,71	37,59	40,57	44,00	47,33	51,55	55,56	78,00	224,47	478,11	842,34	1336,05	2350,72	3082,35

Table 4.3: Joule loss map developed with MATLAB™, postprocessing Altair Flux™ results.

4.2.2 Iron Loss Map

The iron losses in the motor are a result of hysteresis and eddy current losses. To simplify the analysis, these losses were measured in the active materials of the stator and rotor, excluding the contribution of the magnets. The results were compiled into two iron loss maps and depicted in Figures 4.6 and 4.7 for the ANSYS Maxwell™ and Altair Flux™ software, respectively. Distinct regions can be discerned in the plot, each associated with a specific color. The color scheme ranges from dark blue, representing operational points with core losses below 500 W, to yellow, indicating increasing core losses up to the maximum scale value of 3000 W. Tables 4.4 and 4.5 provide a breakdown of the core losses at each operational point for both software programs. The trend observed in the core losses is an increase with higher magnetic flux frequencies and greater torque demands. It is worth noting that the core loss evaluation will be addressed separately, despite employing the same model with identical coefficients, which yields nearly equivalent results.

ANSYS Maxwell™

In the constant torque region, Ansys Maxwell™ estimates minimal core losses. At an operating speed of 0.071 pu, the core losses remain below 35 W for any operating torque. When reaching base speed with peak torque conditions, the core losses amount to 358.95 W. As the operating speed increases, the core losses escalate. At 0.5 pu speed, the average core loss reaches 687.18 W, more than double the core losses at base speed, which average at 270.65 W. Approaching peak speed, the core losses experience a further increment. The losses increase, reaching 2448.48 W compared to the 39.66 W measured at base speed with the same torque demand. At maximum speed and maximum power, the core losses reach their peak value, estimated to be 3419.43 W.

Altair Flux™

Using the same model in Altair Flux™, practically equivalent results are obtained. The trend of the core losses also exhibits an increase with higher operating frequencies and torque requirements. To highlight the impact of the operating speed, the core losses can be compared with the same torque demand but different speed. The core loss estimation jumps from 55.45 W at base speed to 2668.49 W at maximum speed. The highest recorded value for core losses is 3386.22 W, which occurs at maximum speed and peak power. This value is lower than the corresponding value of 33.20 W achieved in ANSYS Maxwell™. These results serve as evidence that both software programs, utilizing the same core loss model, are capable of producing consistent and coherent results.

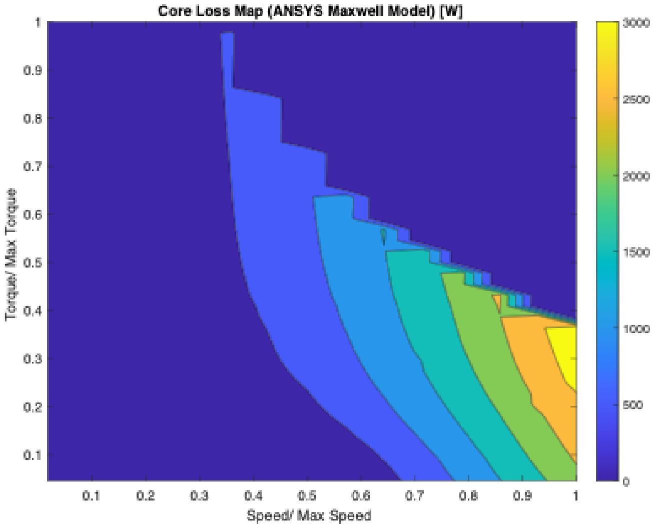

Figure 4.6: Graphic representation of the core loss map developed with ANSYS Maxwell™.

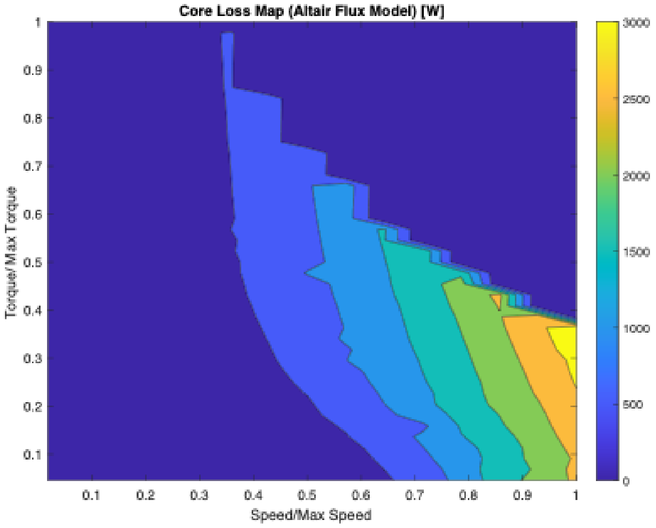

Figure 4.7: Graphic representation of the core loss map developed with Altair Flux™.

CORE LOSS MAP [W]

		Speed/ Max Speed															
		0,02	0,04	0,07	0,14	0,21	0,29	0,36	0,43	0,50	0,57	0,64	0,71	0,79	0,86	0,93	1,00
Torque/ Max Torque	1,00	3,31	10,24	32,53	106,24	215,62	358,95										
	0,98	3,29	10,20	32,39	105,91	214,94	357,89	551,33									
	0,95	3,28	10,16	32,26	105,47	213,95	357,08	545,01									
	0,93	3,27	10,12	32,13	105,04	213,08	355,99	542,27									
	0,91	3,25	10,07	32,00	104,61	212,22	354,96	538,82									
	0,89	3,24	10,02	31,82	104,02	211,14	350,65	535,59									
	0,86	3,22	9,95	31,60	103,26	209,53	350,65	533,13									
	0,84	3,20	9,90	31,45	102,78	208,69	349,14	528,82	753,63								
	0,82	3,19	9,86	31,30	102,28	207,69	347,28	525,54	748,53								
	0,80	3,17	9,81	31,13	101,74	206,77	345,98	520,68	743,25								
	0,77	3,15	9,75	30,94	101,10	205,45	343,73	516,42	739,73								
	0,75	3,13	9,67	30,70	100,28	203,46	340,83	512,85	734,72								
	0,73	3,11	9,61	30,50	99,62	201,76	338,90	507,75	730,94	988,19							
	0,70	3,09	9,55	30,29	98,90	199,74	337,02	503,59	722,45	974,86							
	0,68	3,07	9,48	30,06	98,13	199,11	333,98	500,95	722,45	970,64							
	0,66	3,04	9,39	29,76	97,07	197,05	330,79	495,42	708,54	963,10							
	0,64	3,01	9,30	29,49	96,15	195,22	327,21	490,17	702,27	957,13	1247,36						
	0,61	2,98	9,21	29,19	95,15	193,41	324,25	484,94	693,06	946,05	1247,36						
	0,59	2,95	9,00	28,87	94,04	191,21	320,84	478,21	684,21	936,67	1225,54						
	0,57	2,92	9,00	28,51	92,84	188,98	315,87	471,30	672,70	926,59	1211,64	1526,04					
	0,55	2,88	8,87	28,10	91,41	186,36	311,06	463,85	660,76	916,31	1199,43	1506,13					
	0,52	2,84	8,74	27,67	90,00	183,55	306,18	455,84	647,45	900,68	1188,22	1490,12	1858,97				
	0,50	2,79	8,60	27,21	88,52	180,47	300,53	447,16	632,99	884,95	1170,97	1475,28	1830,84				
	0,48	2,74	8,45	26,66	86,73	176,98	294,23	437,65	617,14	866,22	1151,72	1458,30	1806,56	2220,89			
	0,45	2,68	8,27	26,12	84,77	172,71	287,48	427,16	600,60	845,94	1131,46	1441,99	1778,79	2182,67			
	0,43	2,62	8,09	25,52	82,77	168,39	279,84	415,65	582,01	819,25	1108,56	1419,39	1755,65	2145,72	2591,24		
	0,41	2,46	7,65	24,50	79,55	161,47	267,71	397,35	553,00	783,49	1071,08	1384,50	1723,85	2103,57	2525,20		
	0,39	2,46	7,56	23,72	77,22	156,50	259,59	392,36	534,14	758,43	1043,75	1356,63	1703,83	2073,20	2489,28	2958,41	
	0,36	2,39	7,33	22,97	74,82	151,44	259,59	370,22	511,67	726,99	1011,64	1322,51	1666,78	2041,88	2453,33	2908,30	3419,43
	0,34	2,30	7,05	22,15	72,14	145,55	240,80	356,80	491,15	695,95	972,20	1284,02	1627,23	2011,17	2416,11	2861,28	3359,22
	0,32	2,12	6,79	21,27	69,17	138,05	230,29	337,67	470,09	659,75	934,49	1240,20	1587,67	1968,94	2374,91	2820,65	3299,57
	0,30	2,12	6,47	20,25	65,72	130,84	218,38	319,58	445,89	620,83	890,57	1197,25	1512,29	1915,71	2328,33	2772,03	3242,18
	0,27	1,99	6,12	19,10	61,95	122,91	205,16	299,58	418,78	577,02	842,60	1145,89	1487,10	1862,91	2270,99	2718,13	3186,67
	0,25	1,73	5,75	17,91	57,94	114,65	189,39	278,94	385,90	532,00	786,97	1088,81	1424,23	1798,47	2210,31	2658,42	3130,92
	0,23	1,73	5,31	16,51	53,41	105,29	173,83	255,71	353,68	485,81	725,40	1023,61	1360,18	1734,57	2144,63	2582,70	2984,30
	0,20	1,59	4,84	15,11	48,47	95,92	158,07	232,44	321,21	432,10	654,52	955,67	1291,96	1660,66	2071,32	2582,98	2983,06
	0,18	1,35	4,32	13,44	43,16	85,08	140,18	205,75	284,28	382,44	580,51	878,88	1213,32	1586,45	1991,74	2433,96	2899,70
	0,16	1,25	3,78	11,53	37,24	73,71	121,26	177,74	243,14	322,50	505,72	791,99	1125,79	1507,13	1913,03	2350,45	2816,31
	0,14	1,05	3,17	8,97	31,09	61,30	100,77	147,37	201,12	270,59	419,17	696,91	1039,56	1418,02	1829,88	2263,97	2729,08
	0,11	0,86	2,57	7,54	25,00	49,13	80,65	117,61	160,21	210,92	302,35	604,48	948,21	1329,93	1744,74	2182,47	2640,44
	0,09	0,66	1,96	5,99	18,93	37,03	60,65	88,22	119,89	156,61	205,53	515,22	849,68	1248,02	1658,08	2096,12	2546,26
	0,07	0,45	1,32	3,97	12,39	24,29	39,66	57,53	78,05	103,56	133,50	423,27	764,19	1156,72	1571,54	2001,80	2448,48

Table 4.4: Iron loss map developed with ANSYS Maxwell™.

CORE LOSS MAP [W]																	
		Speed/ Max Speed															
		0,02	0,04	0,07	0,14	0,21	0,29	0,36	0,43	0,50	0,57	0,64	0,71	0,79	0,86	0,93	1,00
Torque/ Max Torque	1,00	3,40	10,51	33,33	108,98	220,89	366,97										
	0,98	3,38	10,46	33,17	108,44	219,77	365,17	545,00									
	0,95	3,37	10,41	33,00	107,96	218,65	363,14	541,66									
	0,93	3,35	10,35	32,82	107,32	217,50	361,37	538,14									
	0,91	3,33	10,30	32,65	106,74	216,80	360,03	534,29									
	0,89	3,32	10,31	32,51	106,22	215,43	357,91	532,41									
	0,86	3,30	10,20	32,48	105,46	213,45	354,72	530,76									
	0,84	3,28	10,13	32,11	104,83	212,07	352,08	523,86	755,13								
	0,82	3,26	10,07	31,91	104,07	210,74	349,79	519,90	746,13								
	0,80	3,24	10,00	31,89	103,37	209,28	347,39	516,05	738,83								
	0,77	3,22	10,02	31,47	102,65	207,83	345,71	513,94	733,86								
	0,75	3,20	9,88	31,29	102,06	206,50	343,02	511,81	725,49								
	0,73	3,18	9,80	31,06	101,55	205,62	341,65	504,11	718,57	989,93							
	0,70	3,15	9,73	30,81	100,42	203,18	339,20	501,31	712,72	981,79							
	0,68	3,13	9,65	30,56	99,58	201,46	334,28	497,15	703,76	970,94							
	0,66	3,10	9,58	30,30	98,87	200,05	331,80	493,30	696,64	960,37	1278,67						
	0,64	3,08	9,50	30,07	97,95	198,12	328,71	488,95	688,23	949,68	1262,75						
	0,61	3,05	9,42	29,78	97,03	196,23	325,51	483,66	681,36	937,69	1245,51						
	0,59	3,02	9,32	29,50	59,05	118,46	322,27	478,68	672,93	924,52	1231,64						
	0,57	2,99	9,27	29,17	95,04	192,21	319,04	498,24	666,89	912,59	1210,38	1559,80					
	0,55	2,97	9,15	28,94	93,79	189,68	314,56	467,38	655,69	899,65	1190,98	1537,02					
	0,52	2,92	8,99	28,46	92,63	187,12	310,37	461,04	759,86	885,81	1173,40	1508,58	1896,42				
	0,50	2,88	8,88	28,07	91,32	184,55	306,08	454,60	634,82	871,77	1153,02	1483,60	1861,92				
	0,48	2,84	8,74	27,62	90,00	181,67	300,83	446,85	644,24	1031,27	1134,87	1458,46	1796,07	1887,52			
	0,45	2,79	8,59	27,15	88,20	178,13	295,31	438,51	610,37	841,30	1112,60	1433,81	1806,47	2204,37			
	0,43	2,74	8,42	26,57	86,25	174,15	288,71	428,60	595,92	822,28	1090,63	1406,24	1762,03	2157,34	2616,33		
	0,41	2,65	8,13	25,64	83,16	167,77	277,89	412,55	571,03	794,39	1060,64	1370,34	1707,34	2121,11	2527,30		
	0,39	2,58	7,91	24,89	80,65	162,52	269,16	399,29	551,35	773,98	1038,45	1340,98	1678,85	2058,37	2469,35	2945,27	
	0,36	2,50	7,67	24,11	78,00	157,10	259,82	385,42	529,32	747,62	1012,98	1314,13	1649,25	2017,68	2434,18	2889,04	3386,22
	0,34	2,41	7,38	23,20	74,89	150,77	249,30	369,34	509,72	715,23	1062,58	1302,23	1611,67	1976,89	2380,70	2838,36	3306,47
	0,32	2,32	7,10	22,29	71,76	144,57	238,98	353,26	486,63	677,58	951,31	1260,77	1578,39	1934,14	2325,65	2780,76	3238,02
	0,30	2,22	6,78	22,72	68,34	137,44	227,33	335,99	463,79	639,50	993,28	1212,79	1536,48	1892,85	2283,19	2707,48	3107,22
	0,27	2,11	6,44	69,47	21,58	130,45	214,07	316,79	439,25	590,96	864,17	1172,95	1503,13	1853,79	2234,51	2651,57	3080,21
	0,25	2,00	6,11	19,06	61,17	122,63	200,68	296,74	413,53	550,89	814,75	1114,67	1464,18	1801,45	2190,54	2601,58	3032,89
	0,23	1,88	8,88	19,00	56,91	113,93	187,03	276,35	400,45	510,00	745,56	1051,28	1398,76	1756,25	2174,16	2542,48	2971,92
	0,20	1,87	5,31	17,53	52,80	105,56	173,15	255,20	354,87	465,15	677,54	997,53	1340,35	1826,52	2078,96	2473,52	2893,10
	0,18	1,59	4,83	16,02	48,09	95,85	156,95	231,82	355,66	422,31	630,43	880,54	1246,43	1628,21	2007,56	2407,09	2829,91
	0,16	1,41	4,27	14,54	42,50	84,99	139,27	205,35	284,86	367,98	540,37	827,77	907,07	1548,86	1940,09	2351,84	2779,55
	0,14	3,70	3,70	11,71	36,69	73,29	120,33	177,32	245,85	318,14	476,05	751,41	1078,49	1474,06	1805,88	2284,88	2713,40
	0,11	1,04	3,11	9,78	30,23	60,46	99,24	146,90	203,24	266,02	360,60	660,95	987,90	1353,12	1698,59	2205,04	2639,75
	0,09	2,54	2,54	7,78	24,52	47,53	78,88	116,07	158,92	205,28	301,94	582,09	897,11	1289,15	1677,22	2183,81	2559,11
	0,07	0,61	1,83	5,57	17,27	33,51	55,45	81,53	115,84	154,41	204,53	499,21	809,67	1181,75	1838,13	2039,39	2668,49

Table 4.5: Iron loss map developed with Altair Flux™.

4.2.3 Mechanical Loss Map

The mechanical loss model was developed using MATLAB™ in a post-processing stage. The simulations were conducted under ideal conditions, while the losses were subsequently added for the efficiency calculations. The values of the mechanical losses were measured at each operating speed, and the same model was used for both software, resulting in identical results.

The trend observed for the mechanical loss is an increment as the speed increases. The highest value, amounting to 410.19 W, is recorded at the maximum speed. However, this loss remains unaffected by variations in the load, as it is not influenced by changes in friction within the bearings or ventilation losses in the motor.

The following table shows the numerical results, while in Figure 4.8 it is shown a more detailed description of the mechanical loss trend.

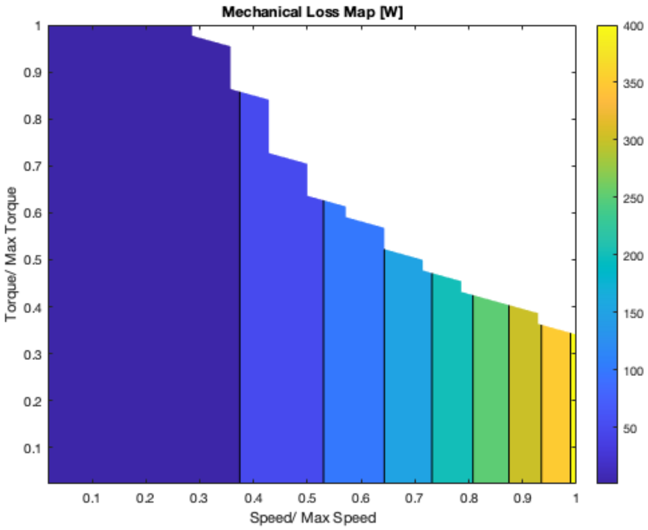

Figure 4.8: Graphic representation of the mechanical loss map developed with MATLAB™.

MECHANICAL LOSS MAP [W]																	
		Speed/ Max Speed															
		0,02	0,04	0,07	0,14	0,21	0,29	0,36	0,43	0,50	0,57	0,64	0,71	0,79	0,86	0,93	1,00
Torque/ Max Torque	1,00	0,75	1,63	3,76	9,76	18,42	30,16										
	0,98	0,75	1,63	3,76	9,76	18,42	30,16	45,41									
	0,95	0,75	1,63	3,76	9,76	18,42	30,16	45,41									
	0,93	0,75	1,63	3,76	9,76	18,42	30,16	45,41									
	0,91	0,75	1,63	3,76	9,76	18,42	30,16	45,41									
	0,89	0,75	1,63	3,76	9,76	18,42	30,16	45,41									
	0,86	0,75	1,63	3,76	9,76	18,42	30,16	45,41									
	0,84	0,75	1,63	3,76	9,76	18,42	30,16	45,41	64,59								
	0,82	0,75	1,63	3,76	9,76	18,42	30,16	45,41	64,59								
	0,80	0,75	1,63	3,76	9,76	18,42	30,16	45,41	64,59								
	0,77	0,75	1,63	3,76	9,76	18,42	30,16	45,41	64,59								
	0,75	0,75	1,63	3,76	9,76	18,42	30,16	45,41	64,59								
	0,73	0,75	1,63	3,76	9,76	18,42	30,16	45,41	64,59	88,12							
	0,70	0,75	1,63	3,76	9,76	18,42	30,16	45,41	64,59	88,12							
	0,68	0,75	1,63	3,76	9,76	18,42	30,16	45,41	64,59	88,12							
	0,66	0,75	1,63	3,76	9,76	18,42	30,16	45,41	64,59	88,12							
	0,64	0,75	1,63	3,76	9,76	18,42	30,16	45,41	64,59	88,12	116,42						
	0,61	0,75	1,63	3,76	9,76	18,42	30,16	45,41	64,59	88,12	116,42						
	0,59	0,75	1,63	3,76	9,76	18,42	30,16	45,41	64,59	88,12	116,42						
	0,57	0,75	1,63	3,76	9,76	18,42	30,16	45,41	64,59	88,12	116,42	149,92					
	0,55	0,75	1,63	3,76	9,76	18,42	30,16	45,41	64,59	88,12	116,42	149,92					
	0,52	0,75	1,63	3,76	9,76	18,42	30,16	45,41	64,59	88,12	116,42	149,92	189,05				
	0,50	0,75	1,63	3,76	9,76	18,42	30,16	45,41	64,59	88,12	116,42	149,92	189,05				
	0,48	0,75	1,63	3,76	9,76	18,42	30,16	45,41	64,59	88,12	116,42	149,92	189,05	234,81			
	0,45	0,75	1,63	3,76	9,76	18,42	30,16	45,41	64,59	88,12	116,42	149,92	189,05	234,81			
	0,43	0,75	1,63	3,76	9,76	18,42	30,16	45,41	64,59	88,12	116,42	149,92	189,05	234,81	285,84		
	0,41	0,75	1,63	3,76	9,76	18,42	30,16	45,41	64,59	88,12	116,42	149,92	189,05	234,81	285,84		
	0,39	0,75	1,63	3,76	9,76	18,42	30,16	45,41	64,59	88,12	116,42	149,92	189,05	234,81	285,84	344,45	
	0,36	0,75	1,63	3,76	9,76	18,42	30,16	45,41	64,59	88,12	116,42	149,92	189,05	234,81	285,84	344,45	410,19
	0,34	0,75	1,63	3,76	9,76	18,42	30,16	45,41	64,59	88,12	116,42	149,92	189,05	234,81	285,84	344,45	410,19
	0,32	0,75	1,63	3,76	9,76	18,42	30,16	45,41	64,59	88,12	116,42	149,92	189,05	234,81	285,84	344,45	410,19
	0,30	0,75	1,63	3,76	9,76	18,42	30,16	45,41	64,59	88,12	116,42	149,92	189,05	234,81	285,84	344,45	410,19
	0,27	0,75	1,63	3,76	9,76	18,42	30,16	45,41	64,59	88,12	116,42	149,92	189,05	234,81	285,84	344,45	410,19
	0,25	0,75	1,63	3,76	9,76	18,42	30,16	45,41	64,59	88,12	116,42	149,92	189,05	234,81	285,84	344,45	410,19
	0,23	0,75	1,63	3,76	9,76	18,42	30,16	45,41	64,59	88,12	116,42	149,92	189,05	234,81	285,84	344,45	410,19
	0,20	0,75	1,63	3,76	9,76	18,42	30,16	45,41	64,59	88,12	116,42	149,92	189,05	234,81	285,84	344,45	410,19
	0,18	0,75	1,63	3,76	9,76	18,42	30,16	45,41	64,59	88,12	116,42	149,92	189,05	234,81	285,84	344,45	410,19
	0,16	0,75	1,63	3,76	9,76	18,42	30,16	45,41	64,59	88,12	116,42	149,92	189,05	234,81	285,84	344,45	410,19
	0,14	0,75	1,63	3,76	9,76	18,42	30,16	45,41	64,59	88,12	116,42	149,92	189,05	234,81	285,84	344,45	410,19
	0,11	0,75	1,63	3,76	9,76	18,42	30,16	45,41	64,59	88,12	116,42	149,92	189,05	234,81	285,84	344,45	410,19
	0,09	0,75	1,63	3,76	9,76	18,42	30,16	45,41	64,59	88,12	116,42	149,92	189,05	234,81	285,84	344,45	410,19
	0,07	0,75	1,63	3,76	9,76	18,42	30,16	45,41	64,59	88,12	116,42	149,92	189,05	234,81	285,84	344,45	410,19

Table 4.6: Mechanical loss map developed with MATLAB™.

4.3 Efficiency Evaluation Test

The main aim of this research endeavor is to assess the efficiency map of the electric motor by utilizing two software programs: ANSYS Maxwell™ and Altair Flux™. A comprehensive set of 660 torque/speed combinations has been analyzed to measure the motor's efficiency. At each operating point, the iron losses, mechanical losses, and joule losses have been assessed. From the knowledge of these and of the output power, the evaluation of the efficiency is straightforward.

4.3.1 Experimental Efficiency Map

The measured efficiency of the electric motor, gathered at different torque and speed combinations by an OEM, is reported in Table 4.7. The experimental map can be analyzed distinguishing the constant torque region from the constant power region.

In the constant torque or linearly increasing power region, the efficiency is initially low (below 60%) at the minimum operating speed when peak torque performance is required. However, as the operating speed increases, the efficiency rapidly improves. At a speed of 0.214 pu, the efficiency exceeds 90% in all operating conditions. Moreover, at medium-low torque levels (below 0.545 pu torque), the efficiency remains above 95%. The average efficiency at base speed is 95.27%.

Moving to the constant power region, the efficiency reaches its peak value of 96.64% at 0.429 pu speed and 0.364 pu torque. Up to this operating speed, the efficiency shows an increasing trend with a fixed torque requirement. However, at higher speeds, the efficiency slightly decreases. The most significant difference can be observed at low torque requirements, where assessing efficiency experimentally becomes extremely challenging due to difficulties in evaluating iron losses.

Figure 4.9 depicts the efficiency map, illustrating various regions of efficiency. The peak efficiency region is represented in green, indicating the optimal efficiency values. Transitioning to yellow and red, lower efficiency regions are represented. These regions correspond to situations where peak torque is required at very low speeds and at maximum operating speeds with extremely low torque demands.

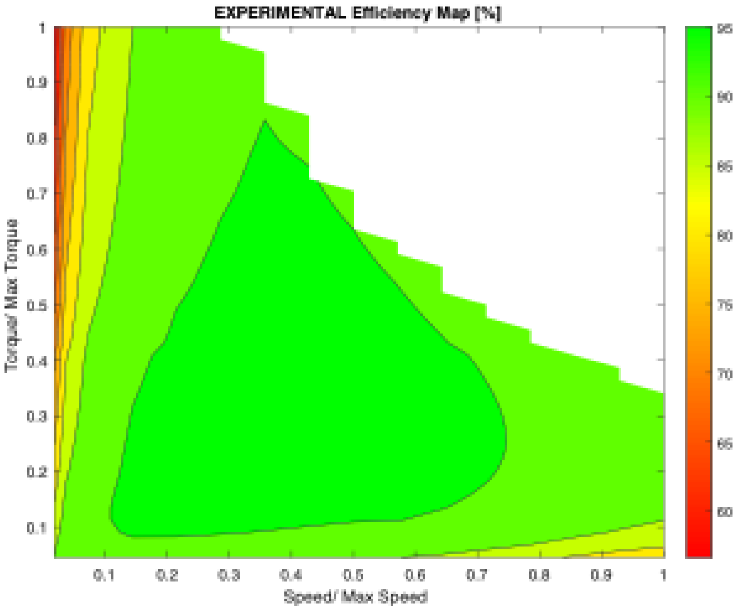

Figure 4.9: Graphic representaion of the experimental efficiency map.

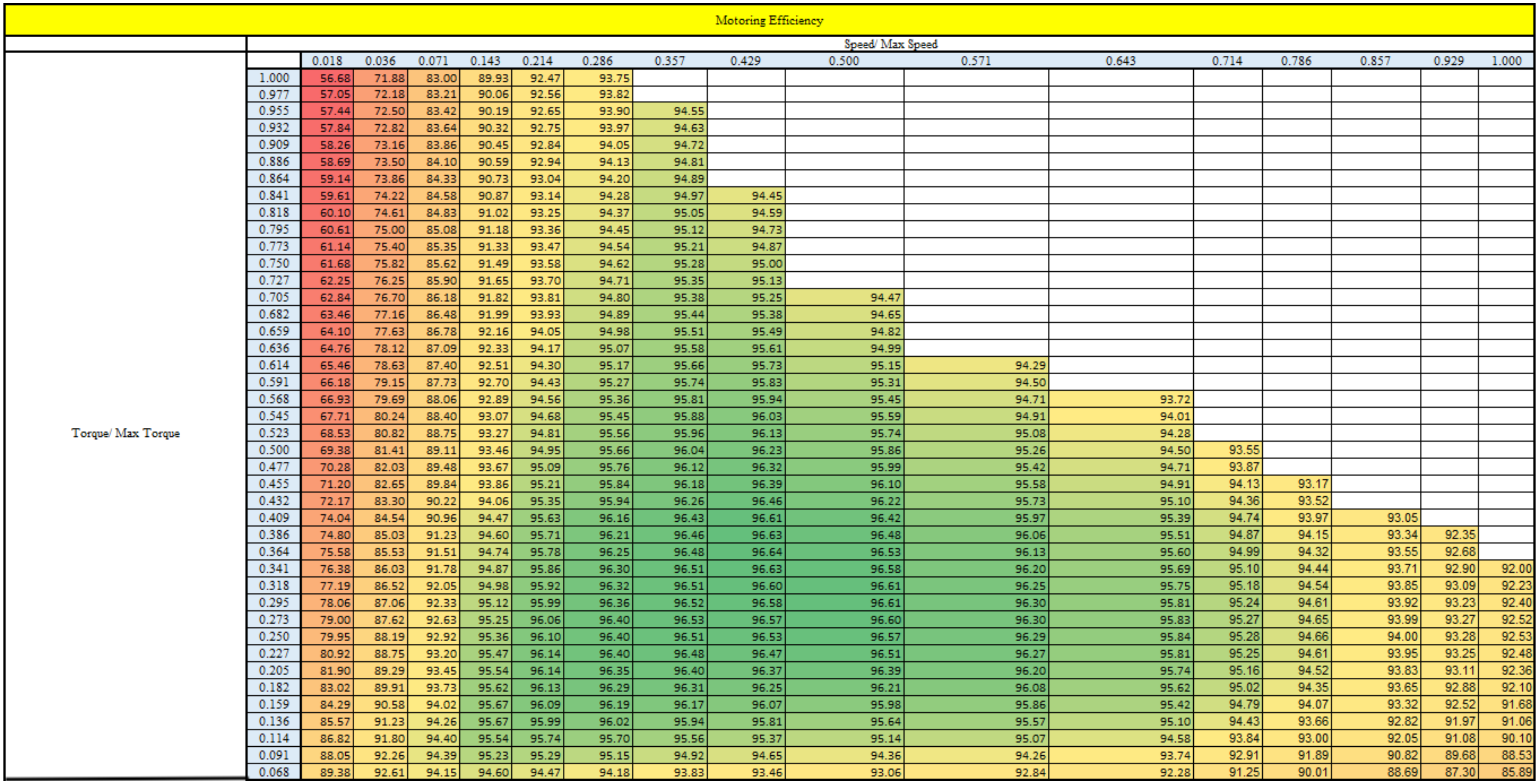

Motoring Efficiency																	
		Speed/ Max Speed															
		0.018	0.036	0.071	0.143	0.214	0.286	0.357	0.429	0.500	0.571	0.643	0.714	0.786	0.857	0.929	1.000
Torque/ Max Torque	1.000	56.68	71.88	83.00	89.93	92.47	93.75										
	0.977	57.05	72.18	83.21	90.06	92.56	93.82										
	0.955	57.44	72.50	83.42	90.19	92.65	93.90	94.55									
	0.932	57.84	72.82	83.64	90.32	92.75	93.97	94.63									
	0.909	58.26	73.16	83.86	90.45	92.84	94.05	94.72									
	0.886	58.69	73.50	84.10	90.59	92.94	94.13	94.81									
	0.864	59.14	73.86	84.33	90.73	93.04	94.20	94.89									
	0.841	59.61	74.22	84.58	90.87	93.14	94.28	94.97	94.45								
	0.818	60.10	74.61	84.83	91.02	93.25	94.37	95.05	94.59								
	0.795	60.61	75.00	85.08	91.18	93.36	94.45	95.12	94.73								
	0.773	61.14	75.40	85.35	91.33	93.47	94.54	95.21	94.87								
	0.750	61.68	75.82	85.62	91.49	93.58	94.62	95.28	95.00								
	0.727	62.25	76.25	85.90	91.65	93.70	94.71	95.35	95.13								
	0.705	62.84	76.70	86.18	91.82	93.81	94.80	95.38	95.25	94.47							
	0.682	63.46	77.16	86.48	91.99	93.93	94.89	95.44	95.38	94.65							
	0.659	64.10	77.63	86.78	92.16	94.05	94.98	95.51	95.49	94.82							
	0.636	64.76	78.12	87.09	92.33	94.17	95.07	95.58	95.61	94.99							
	0.614	65.46	78.63	87.40	92.51	94.30	95.17	95.66	95.73	95.15	94.29						
	0.591	66.18	79.15	87.73	92.70	94.43	95.27	95.74	95.83	95.31	94.50						
	0.568	66.93	79.69	88.06	92.89	94.56	95.36	95.81	95.94	95.45	94.71	93.72					
	0.545	67.71	80.24	88.40	93.07	94.68	95.45	95.88	96.03	95.59	94.91	94.01					
	0.523	68.53	80.82	88.75	93.27	94.81	95.56	95.96	96.13	95.74	95.08	94.28					
	0.500	69.38	81.41	89.11	93.46	94.95	95.66	96.04	96.23	95.86	95.26	94.50	93.55				
	0.477	70.28	82.03	89.48	93.67	95.09	95.76	96.12	96.32	95.99	95.42	94.71	93.87				
	0.455	71.20	82.65	89.84	93.86	95.21	95.84	96.18	96.39	96.10	95.58	94.91	94.13	93.17			
	0.432	72.17	83.30	90.22	94.06	95.35	95.94	96.26	96.46	96.22	95.73	95.10	94.36	93.52			
	0.409	74.04	84.54	90.96	94.47	95.63	96.16	96.43	96.61	96.42	95.97	95.39	94.74	93.97	93.05		
	0.386	74.80	85.03	91.23	94.60	95.71	96.21	96.46	96.63	96.48	96.06	95.51	94.87	94.15	93.34	92.35	
	0.364	75.58	85.53	91.51	94.74	95.78	96.25	96.48	96.64	96.53	96.13	95.60	94.99	94.32	93.55	92.68	
	0.341	76.38	86.03	91.78	94.87	95.86	96.30	96.51	96.63	96.58	96.20	95.69	95.10	94.44	93.71	92.90	92.00
	0.318	77.19	86.52	92.05	94.98	95.92	96.32	96.51	96.60	96.61	96.25	95.75	95.18	94.54	93.85	93.09	92.23
	0.295	78.06	87.06	92.33	95.12	95.99	96.36	96.52	96.58	96.61	96.30	95.81	95.24	94.61	93.92	93.23	92.40
	0.273	79.00	87.62	92.63	95.25	96.06	96.40	96.53	96.57	96.60	96.30	95.83	95.27	94.65	93.99	93.27	92.52
	0.250	79.95	88.19	92.92	95.36	96.10	96.40	96.51	96.53	96.57	96.29	95.84	95.28	94.66	94.00	93.28	92.53
	0.227	80.92	88.75	93.20	95.47	96.14	96.40	96.48	96.47	96.51	96.27	95.81	95.25	94.61	93.95	93.25	92.48
	0.205	81.90	89.29	93.45	95.54	96.14	96.35	96.40	96.37	96.39	96.20	95.74	95.16	94.52	93.83	93.11	92.36
	0.182	83.02	89.91	93.73	95.62	96.13	96.29	96.31	96.25	96.21	96.08	95.62	95.02	94.35	93.65	92.88	92.10
	0.159	84.29	90.58	94.02	95.67	96.09	96.19	96.17	96.07	95.98	95.86	95.42	94.79	94.07	93.32	92.52	91.68
	0.136	85.57	91.23	94.26	95.67	95.99	96.02	95.94	95.81	95.64	95.57	95.10	94.43	93.66	92.82	91.97	91.06
	0.114	86.82	91.80	94.40	95.54	95.74	95.70	95.56	95.37	95.14	95.07	94.58	93.84	93.00	92.05	91.08	90.10
	0.091	88.05	92.26	94.39	95.23	95.29	95.15	94.92	94.65	94.36	94.26	93.74	92.91	91.89	90.82	89.68	88.53
	0.068	89.38	92.61	94.15	94.60	94.47	94.18	93.83	93.46	93.06	92.84	92.28	91.25	90.01	88.69	87.30	85.89

Table 4.7: Experimental efficiency map

4.3.2 Simulated Efficiency Map

The efficiency map serves as a valuable tool for evaluating the effectiveness of power conversion in the motor. This section delves into the specifics of the efficiency maps obtained using the two software packages.

Figure 4.10 and 4.11 illustrate the efficiency map developed with the two software, providing a visual representation of the data. The green region is highlighted to indicate the highest efficiency region, which is observed to extend even to very low torque requirements in either software programs. On the maps, areas colored in yellow denote intermediate efficiency conditions, indicating that power requests can be achieved with an efficiency conversion ranging from 85% to 75%. The region with speeds below 0.1 pu have even lower efficiency. It is depicted in red to signify values below 60%.

ANSYS Maxwell™

Table 4.8 presents the efficiency data for each operating point obtained with ANSYS Maxwell™. The analysis differentiates between the constant torque region and the constant power region.

Within the constant torque region, a relatively low-efficiency region is observed at 0.018 pu speed. The lowest efficiency is recorded at peak torque, measuring 55.2%, compared to the experimental map's value of 56.6%. Increasing the operating speed, the efficiency will escalate. Notably, the efficiency remains high in the low torque region, where the contribution of core losses is underestimated by the adopted loss model. The peak efficiency occurs at 0.357 pu speed and 0.182 pu torque, reaching 97.1%, slightly higher than the experimental map's value of 96.64% obtained at the same operating speed. In the constant power region, the simulations follow the experimental trend, albeit with a slight tendency to overestimate efficiency as the motor approaches maximum speed. In the interval ranging from 0.357 to 0.571 pu speed, the average efficiency of the motor is 95.81%. Approaching maximum speed, the motor maintains a relatively high level of efficiency, reaching a maximum value of 91.60%.

Altair Flux™

Table 4.9 presents the efficiency map developed using Altair Flux™. Within the constant torque region, efficiency increases with speed, reaching its maximum at 0.214 pu speed. The simulation results show a transition from 55.2% efficiency at the point of peak torque but minimum speed, to extremely high efficiency values observed at minimum torque demand. The peak efficiency is of 97.94% , over 1% higher than the actual value. As operating speeds increase, the efficiency experiences a notable reduction compared to the experimental values. Within the constant power region, the efficiency initially exceeds 92% across all operating torques when considering a speed of 0.5 pu. However, as the speed increases, a higher current is required to generate the necessary torque, leading to increased joule dissipation. Joule losses significantly impact the efficiency, causing it to gradually decrease. At peak operating speed, the average efficiency is 86.70%.

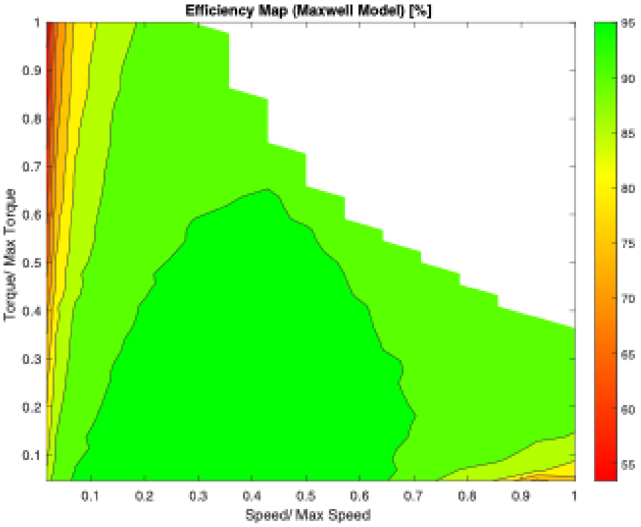

Figure 4.10: Graphic representation of the efficiency map developed with ANSYS Maxwell™.

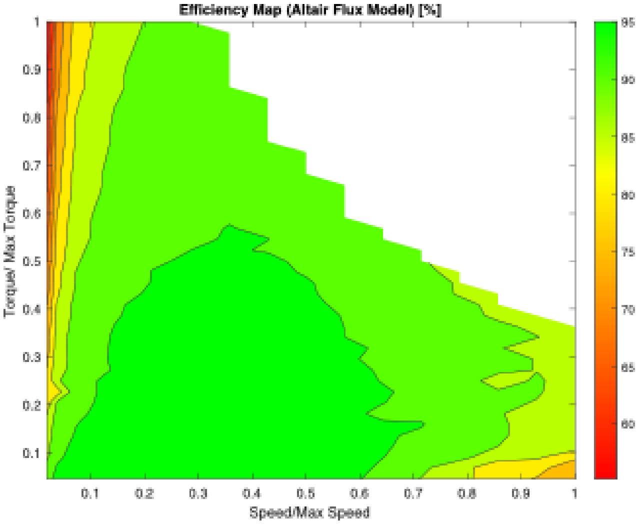

Figure 4.11: Graphic representation of the joule loss map developed with Altair Flux™.

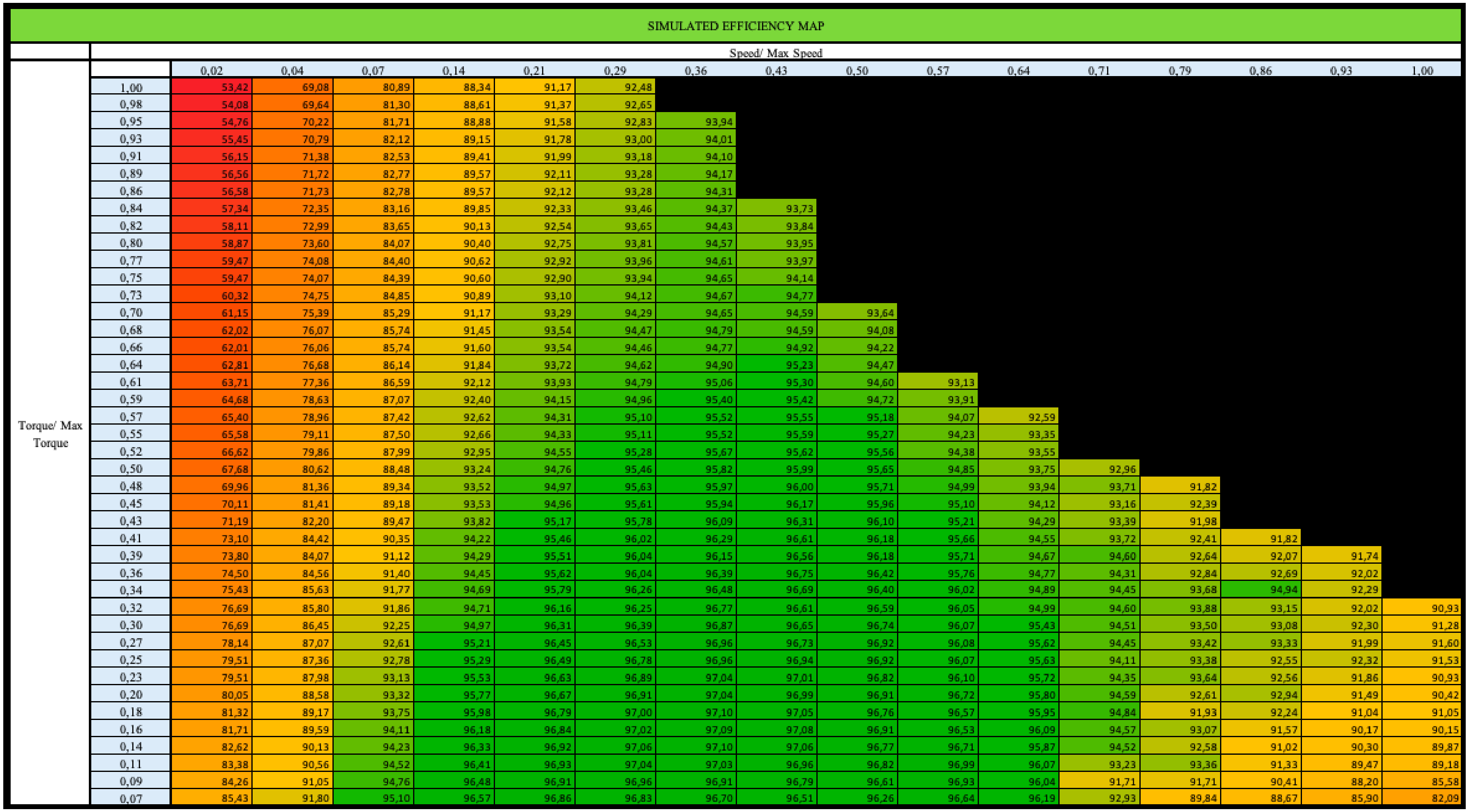

SIMULATED EFFICIENCY MAP																
	Speed/ Max Speed															
Torque/ Max Torque	0,02	0,04	0,07	0,14	0,21	0,29	0,36	0,43	0,50	0,57	0,64	0,71	0,79	0,86	0,93	1,00
1,00	53,42	69,08	80,89	88,34	91,17	92,48										
0,98	54,08	69,64	81,30	88,61	91,37	92,65										
0,95	54,76	70,22	81,71	88,88	91,58	92,83	93,94									
0,93	55,45	70,79	82,12	89,15	91,78	93,00	94,01									
0,91	56,15	71,38	82,53	89,41	91,99	93,18	94,10									
0,89	56,56	71,72	82,77	89,57	92,11	93,28	94,17									
0,86	56,58	71,73	82,78	89,57	92,12	93,28	94,31									
0,84	57,34	72,35	83,16	89,85	92,33	93,46	94,37	93,73								
0,82	58,11	72,99	83,65	90,13	92,54	93,65	94,43	93,84								
0,80	58,87	73,60	84,07	90,40	92,75	93,81	94,57	93,95								
0,77	59,47	74,08	84,40	90,62	92,92	93,96	94,61	93,97								
0,75	59,47	74,07	84,39	90,60	92,90	93,94	94,65	94,14								
0,73	60,32	74,75	84,85	90,89	93,10	94,12	94,67	94,77								
0,70	61,15	75,39	85,29	91,17	93,29	94,29	94,65	94,59	93,64							
0,68	62,02	76,07	85,74	91,45	93,54	94,47	94,79	94,59	94,08							
0,66	62,01	76,06	85,74	91,60	93,54	94,46	94,77	94,92	94,22							
0,64	62,81	76,68	86,14	91,84	93,72	94,62	94,90	95,23	94,47							
0,61	63,71	77,36	86,59	92,12	93,93	94,79	95,06	95,30	94,60	93,13						
0,59	64,68	78,63	87,07	92,40	94,15	94,96	95,40	95,42	94,72	93,91						
0,57	65,40	78,96	87,42	92,62	94,31	95,10	95,52	95,55	95,18	94,07	92,59					
0,55	65,58	79,11	87,50	92,66	94,33	95,11	95,52	95,59	95,27	94,23	93,35					
0,52	66,62	79,86	87,99	92,95	94,55	95,28	95,67	95,62	95,56	94,38	93,55					
0,50	67,68	80,62	88,48	93,24	94,76	95,46	95,82	95,99	95,65	94,85	93,75	92,96				
0,48	69,96	81,36	89,34	93,52	94,97	95,63	95,97	96,00	95,71	94,99	93,94	93,71	91,82			
0,45	70,11	81,41	89,18	93,53	94,96	95,61	95,94	96,17	95,96	95,10	94,12	93,16	92,39			
0,43	71,19	82,20	89,47	93,82	95,17	95,78	96,09	96,31	96,10	95,21	94,29	93,39	91,98			
0,41	73,10	84,42	90,35	94,22	95,46	96,02	96,29	96,61	96,18	95,66	94,55	93,72	92,41	91,82		
0,39	73,80	84,07	91,12	94,29	95,51	96,04	96,15	96,56	96,18	95,71	94,67	94,60	92,64	92,07	91,74	
0,36	74,50	84,56	91,40	94,45	95,62	96,04	96,39	96,75	96,42	95,76	94,77	94,31	92,84	92,69	92,02	
0,34	75,43	85,63	91,77	94,69	95,79	96,26	96,48	96,69	96,40	96,02	94,89	94,45	93,68	94,94	92,29	
0,32	76,69	85,80	91,86	94,71	96,16	96,25	96,77	96,61	96,59	96,05	94,99	94,60	93,88	93,15	92,02	90,93
0,30	76,69	86,45	92,25	94,97	96,31	96,39	96,87	96,65	96,74	96,07	95,43	94,51	93,50	93,08	92,30	91,28
0,27	78,14	87,07	92,61	95,21	96,45	96,53	96,96	96,73	96,92	96,08	95,62	94,45	93,42	93,33	91,99	91,60
0,25	79,51	87,36	92,78	95,29	96,49	96,78	96,96	96,94	96,92	96,07	95,63	94,11	93,38	92,55	92,32	91,53
0,23	79,51	87,98	93,13	95,53	96,63	96,89	97,04	97,01	96,82	96,10	95,72	94,35	93,64	92,56	91,86	90,93
0,20	80,05	88,58	93,32	95,77	96,67	96,91	97,04	96,99	96,91	96,72	95,80	94,59	92,61	92,94	91,49	90,42
0,18	81,32	89,17	93,75	95,98	96,79	97,00	97,10	97,05	96,76	96,57	95,95	94,84	91,93	92,24	91,04	91,05
0,16	81,71	89,59	94,11	96,18	96,84	97,02	97,09	97,08	96,91	96,53	96,09	94,57	93,07	91,57	90,17	90,15
0,14	82,62	90,13	94,23	96,33	96,92	97,06	97,10	97,06	96,77	96,71	95,87	94,52	92,58	91,02	90,30	89,87
0,11	83,38	90,56	94,52	96,41	96,93	97,04	97,03	96,96	96,82	96,99	96,07	93,23	93,36	91,33	89,47	89,18
0,09	84,26	91,05	94,76	96,48	96,91	96,96	96,91	96,79	96,61	96,93	96,04	91,71	91,71	90,41	88,20	85,58
0,07	85,43	91,80	95,10	96,57	96,86	96,83	96,70	96,51	96,26	96,64	96,19	92,93	89,84	88,67	85,90	82,09

Table 4.8: Efficiency map simuated with ANSYS Maxell™.

SIMULATED EFFICIENCY MAP

Torque/ Max Torque	Speed/ Max Speed															
	0,02	0,04	0,07	0,14	0,21	0,29	0,36	0,43	0,50	0,57	0,64	0,71	0,79	0,86	0,93	1,00
1,00	55,20	70,37	82,11	88,21	90,57	91,71										
0,98	55,86	70,92	82,18	88,47	90,79	91,90	92,96									
0,95	56,54	71,48	82,57	88,75	91,01	92,09	92,93									
0,93	57,23	72,05	82,97	89,02	91,23	92,27	93,13									
0,91	57,95	72,64	83,38	89,29	91,44	92,47	93,23									
0,89	58,33	72,95	83,60	89,45	91,57	92,58	93,17									
0,86	57,67	72,91	83,59	89,43	91,56	92,56	93,23									
0,84	59,64	74,00	84,33	89,72	91,79	92,77	93,30	92,22								
0,82	60,43	74,63	84,76	90,02	92,03	92,97	93,36	92,59								
0,80	61,21	75,24	85,17	90,30	92,26	93,17	94,05	92,89								
0,77	61,81	75,71	85,50	90,53	92,44	93,34	93,44	92,88								
0,75	61,79	75,69	85,50	90,51	92,42	93,31	92,32	93,32								
0,73	62,67	76,38	85,96	90,80	92,66	93,53	94,20	93,46	92,40							
0,70	63,53	77,04	86,40	91,12	92,91	93,74	94,16	93,73	92,22							
0,68	64,45	77,74	86,86	91,44	93,17	93,95	94,36	94,00	92,80							
0,66	64,42	77,72	86,87	91,43	93,16	93,96	94,36	94,12	92,99	91,05						
0,64	65,27	78,36	87,29	91,71	93,38	94,14	94,53	94,49	92,79	91,32						
0,61	66,24	79,08	87,76	92,22	93,78	94,35	94,72	94,49	93,34	92,06						
0,59	67,27	79,84	88,25	92,47	94,05	94,58	94,92	94,72	93,71	91,85						
0,57	68,04	80,40	88,35	92,61	94,09	94,76	95,05	94,82	93,35	92,10	90,59					
0,55	68,26	80,56	88,45	92,67	94,14	94,78	95,10	95,03	94,02	92,37	91,98					
0,52	69,40	81,38	88,98	93,18	94,54	95,00	95,29	94,80	94,08	92,85	91,28	90,01				
0,50	69,96	81,78	89,50	93,51	94,80	95,23	95,50	95,72	94,25	92,81	91,54	90,33				
0,48	71,73	83,02	90,03	93,84	95,05	95,46	95,70	95,75	94,75	93,27	92,37	91,11	88,61			
0,45	71,86	83,11	90,33	93,87	95,07	95,57	95,80	96,02	95,33	93,71	92,67	91,71	89,59			
0,43	73,14	84,00	90,65	94,22	95,34	95,80	96,00	96,07	95,44	93,92	93,19	91,76	89,64	88,60		
0,41	74,97	85,24	91,42	94,70	95,71	96,12	96,29	96,27	95,66	94,48	94,30	92,07	91,06	88,93		
0,39	75,41	85,54	91,61	94,82	95,80	96,20	96,36	96,66	96,16	94,83	93,21	92,35	91,12	89,39	88,22	
0,36	76,28	86,12	91,96	95,03	95,97	96,35	96,49	96,82	96,23	94,97	94,10	92,97	91,49	90,67	89,31	87,41
0,34	77,46	86,89	92,44	95,33	96,21	96,55	96,69	96,69	96,34	95,05	92,80	92,93	91,87	90,64	90,13	88,21
0,32	77,67	87,02	92,51	95,40	96,25	96,60	96,72	96,84	96,76	95,60	94,63	93,48	91,70	90,33	87,90	88,57
0,30	78,93	87,92	91,57	95,71	96,50	96,80	96,91	96,79	96,83	95,34	94,43	93,01	91,57	90,82	89,90	89,71
0,27	80,31	88,63	91,33	95,36	96,68	96,99	97,08	96,53	97,37	95,92	94,66	93,40	92,01	90,88	89,90	86,50
0,25	80,72	88,98	93,65	96,08	96,75	97,17	97,23	96,91	97,37	96,38	94,82	93,69	92,02	88,28	90,48	88,39
0,23	81,84	81,78	93,36	96,31	96,94	97,31	97,37	96,99	97,34	96,49	95,39	94,07	92,26	90,40	90,31	88,50
0,20	82,43	90,04	93,72	96,41	97,00	97,32	97,36	97,03	97,46	97,14	95,15	93,34	91,59	90,60	89,86	88,26
0,18	84,81	91,47	94,24	96,64	97,16	97,44	97,46	97,01	97,32	96,83	93,57	93,89	92,60	90,25	88,73	88,19
0,16	86,44	92,43	94,88	96,99	97,42	97,54	97,54	97,15	97,52	97,48	95,74	95,32	91,41	90,59	88,45	87,61
0,14	87,24	93,01	95,29	97,16	97,52	97,60	97,56	97,23	97,36	96,63	95,55	94,27	92,85	90,42	88,85	87,53
0,11	88,30	93,48	95,92	97,45	97,72	97,75	97,67	97,37	97,22	97,79	95,66	93,21	90,33	90,05	87,69	87,59
0,09	89,19	94,11	96,51	97,56	97,77	97,74	97,63	97,61	97,45	97,56	95,07	92,74	91,56	86,84	85,80	81,30
0,07	91,61	95,29	97,13	97,88	97,97	97,87	97,72	97,20	96,93	97,50	94,08	90,98	86,87	81,56	82,05	76,11

Table 4.9: Efficiency map simuated with Altair Flux™.

Chapter 5

Analysis of the Results

5.1 Performance Analysis of the Electric Motor Model

In the upcoming sections, the attention will be shifted to the analysis of the simulation results. The focus will be on assessing the performance of the two software tools by investigating more in details the motor losses and by evaluating the percentual differences between the experimental and simulated efficiency maps. To determine the accuracy of the forecasting method, the mean absolute percentage error is the metric selected.

5.1.1 Loss Comparison

This section focuses on the assessment of each motor loss in the overall power loss analysis. This evaluation was conducted by considering combinations of three operating speeds (low, medium, and high) and two torque points (low and high). Figures 5.1 and 5.2 depict the separation of losses evaluated using the two software tools. Both software packages indicate that the most significant factor contributing to reduced efficiency is the joule loss.

The escalation of joule loss is directly linked to an augmented current demand. One key factor behind the higher current requirement is the back electromotive force generated by the motor. As the speed increases, the back electromotive force also increases. However, to maintain the required torque output, the applied voltage needs to overcome this b-emf, resulting in higher current draw. Additionally, the motor's internal resistance and winding inductance play a role. At higher speeds, the internal resistance causes more voltage drop, leading to a higher voltage requirement to compensate for this drop.

The simulation results demonstrate that frequency has the most significant impact on core losses. In fact, transitioning from the intermediate to the high-speed scenario leads to an approximately six-fold increase in core losses. The most significant aspect of frequency's impact on core losses is its influence on magnetic flux density. The magnitude of hysteresis losses increases with higher magnetic flux density, leading to greater energy dissipation in the form of heat within the core material. The magnitude of eddy current losses is proportional to the square of the magnetic flux density. Higher magnetic flux density increases the intensity of eddy currents, resulting in increased energy losses.

The mechanical losses make a relatively small but significant contribution, which should not be disregarded. At the maximum speed examined, they account for up to 5 % of the total losses, for the software ANSYS Maxwell™.

The primary disparity observed between the two software programs in the analyzed data lies in the calculation of joule loss. Specifically, as both software employ the same resistance model, the discrepancy arises from the evaluation of current. Ansys Maxwell demonstrates a more precise modeling of current distribution and AC effects, resulting in a lower Joule loss value and consequently higher efficiency. Given that the mechanical and core losses are equivalent between the two software programs, the assessment of Joule loss becomes the key factor that characterizes the accuracy of efficiency evaluation.

ANSYS Maxwell™

The results obtained from ANSYS Maxwell™ reveal that the joule loss has the highest contribution across all six operating conditions. When the torque request is increased from 0.25 pu to 0.909 pu, the Joule loss in all analyzed operating speeds significantly intensifies. For example, at a speed of 0.07 pu, the joule loss increases from 420.42 W to 4371.46 W. Similarly, at an intermediate speed of 0.429 pu, the joule loss rises from 625.76 W to 6992.72 W. At a speed of 0.928 pu, the Joule loss nearly doubles, going from 3854 W to 7780.28 W when transitioning from the low torque to the peak torque scenario. The previous results show how moving to higher operating speed, the Joule losses increase significantly.

Core losses rank as the second most impactful loss, but their relative weight decreases as torque increases. The core losses in the motor are influenced by both speed and torque request. At a speed of 0.07 pu, the core losses increase from 17.9 W with a torque request of 0.25 pu to 32 W with a torque request of 0.909 pu. Moving to a speed of 0.429 pu, the core losses escalate from 385.9 W at a low torque requirement to 753.63 W at a high torque demand. Finally, at the highest analyzed speed, the core losses amount to 2658.41 W with a torque request of 0.25 pu and 2958.41 W.

Notably, mechanical losses consistently represent the lowest contribution in all cases. As mentioned in the preceding section, the mechanical losses are independent of the operating torque and are characterized by the following values: 3.76 W, 64.6 W, and 344.36 W at speeds of 0.07 pu, 0.429 pu, and 0.928 pu, respectively.

Table 5.1 and 5.2 show the mechanical, Joule and Core loss split respectively at low and high torque, for the software ANSYS Maxwell™.

Altair Flux™

Similar findings are observed in the simulation outcomes obtained from Altair Flux. The joule loss dominates as the major contributor by a significant margin. At a low speed, the joule loss is 377.69 W at 0.25 pu torque and increases to 4263.87 W at 0.909 pu torque. Moving to an intermediate speed of 0.429 pu, the joule loss surges by nearly 15 times, rising from 590.65 W to 8936.15 W. At the peak speed, the joule loss reaches 12092.13 W, significantly surpassing the 7780.28 W achieved in Ansys Maxwell under identical operating conditions.

The relative weight of core losses decreases with increasing speed, although their absolute value tends to increase. The core losses model employed in Altair Flux™ is identical to that of ANSYS Maxwell™, resulting in nearly identical loss calculations. This indicates that both software programs generate magnetic flux density in the motor that is virtually indistinguishable under similar operating conditions. For example, when analyzing the peak operating speed and torque, the absolute difference between the two software is 13.14 W, corresponding to a percentage difference of 0.446%.

The mechanical losses have the same absolute value as they are determined through post-processing. However, their relative weight is lower due to the considerably larger joule losses evaluated using Altair Flux.

Table 5.1 and 5.2 show the mechanical, Joule and Core loss split respectively at low and high torque, for the software Altair Flux™.

Table 5.1: Motor losses developed with Altair Flux™, combining low torque with three operating speeds

	Mechanical Loss [W]	**Joule Loss [W]**	**Core Loss [W]**
Low Speed	3.76	377.69	19.05
Medium Speed	64.59	590.563	413.53
High Speed	344.38	5639.47	2601.59

Table 5.2: Motor losses developed with Altair Flux™, combining high torque with three operating speeds

	Mechanical Loss [W]	**Joule Loss [W]**	**Core Loss [W]**
Low Speed	3.76	4263.87	32.65
Medium Speed	64.59	8936.15	755.13
High Speed	344.38	12092.13	2945.27

Table 5.3: Motor losses developed with ANSYS Maxwell™, combining low torque with three operating speeds

	Mechanical Loss [W]	**Joule Loss [W]**	**Core Loss [W]**
Low Speed	3.76	420.42	17.905
Medium Speed	64.59	625.76	385.90
High Speed	344.38	3854.01	2658.42

Table 5.4: Motor losses developed with ANSYS Maxwell™, combining high torque with three operating speeds

	Mechanical Loss [W]	**Joule Loss [W]**	**Core Loss [W]**
Low Speed	3.76	4371.46	31.98
Medium Speed	64.59	6992.72	753.63
High Speed	344.38	7780.28	2958.41

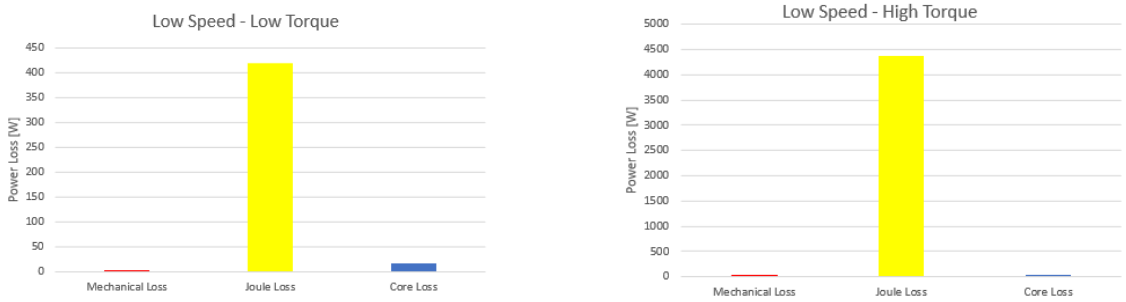

(a) Loss separation at low speed and low torque **(b)** Loss separation at low speed and high torque

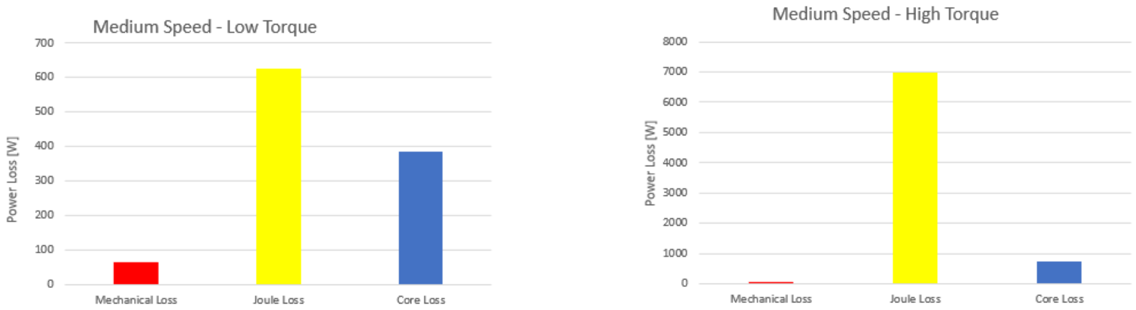

(c) Loss separation at medium speed and low torque **(d)** Loss separation at medium speed and high torque

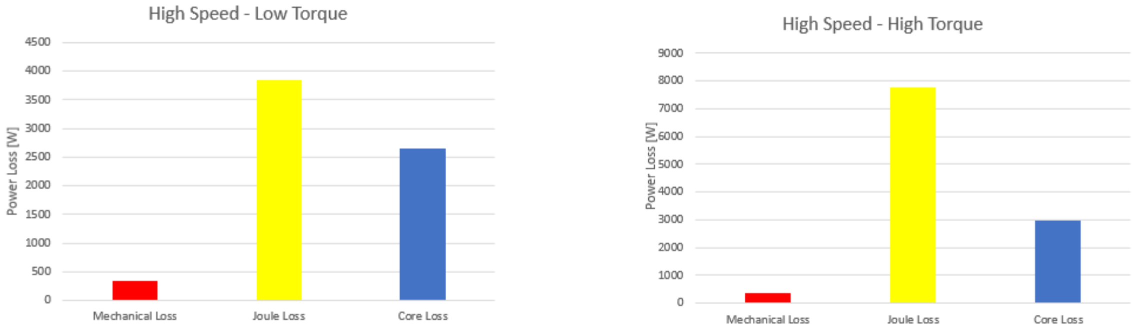

(e) Loss separation at high speed and low torque **(f)** Loss separation at high speed and high torque

Figure 5.1: Core, Joule and Mechanical loss evaluated at three operating speeds and two torque configurations, with ANSYS Maxwell™.

(a) Loss separation at low speed and low torque

(b) Loss separation at low speed and high torque

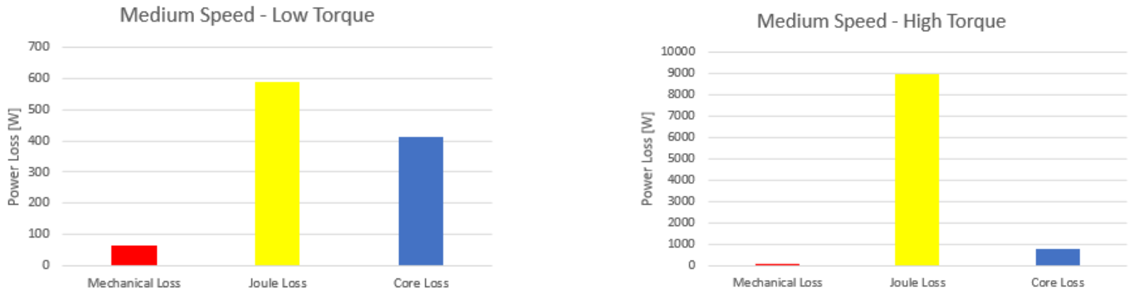

(c) Loss separation at medium speed and low torque

(d) Loss separation at medium speed and high torque

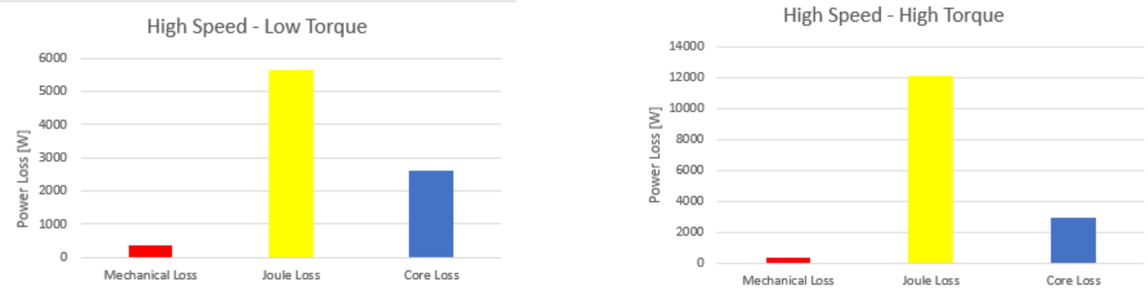

(e) Loss separation at high speed and low torque

(f) Loss separation at high speed and high torque

Figure 5.2: Core, Joule and Mechanical loss evaluated at three operating speeds and two torque configurations, with Altair Flux™.

5.1.2 Error Map

”Error” maps, which illustrate the differences between the experimental and simulated efficiency values, are used to assess the precision of the two software tools. Figure 5.3 and 5.4 present separate plots for the ANSYS Maxwell™ model and the Altair Flux™ model. The positive side of the scale refers to the model’s overestimation of efficiency, while the negative side indicates the model’s underestimation of efficiency.

ANSYS Maxwell™

Table 5.5 provides insight into the error in efficiency estimation for the ANSYS Maxwell™ software. It is possible to differentiate the analysis of the constant torque region from that of the constant power region.

The highest overestimation of efficiency occurs at points with minimum torque up to 0.714 pu speed. This overestimation at low speeds can be attributed to the adopted model for core losses, which tends to underestimate them in such scenarios.

However, the model exhibits improved accuracy at higher speeds, aligning with the observed trend in the experimental data fitted using the ’Modified Bertotti Method’ developed in MATLAB™. At higher torque demands, the ANSYS Maxwell™ software demonstrates precise efficiency predictions. This accuracy stems from its consideration of proximity and skin effects on current distribution, resulting in a reliable evaluation of joule losses.

Conversely, efficiency tends to be underestimated when max speed conditions are reached, leading to the largest error of 3.80% observed at maximum speed and minimum torque. The mean absolute percentage error for the ANSYS Maxwell™ software is 0.71%. Notably, the software deviates from the experimental behavior in working conditions involving a combination of maximum speed, minimum torque, or maximum torque, which represent challenging scenarios to simulate due to the interaction of multiple effects.

Figure 5.3 provides a clearer understanding of the findings presented in Table 5.5. Different regions of the field are differentiated using a color spectrum, ranging from green (indicating efficiency overestimation) to red (indicating efficiency underestimation), to represent the areas where the motor operates with varying degrees of efficiency. The region of the map, characterized by operating torque lower than 0.2 pu torque and operating speed between 0.1 and 0.8 pu speed, is highlighted in green, since in these operational points efficiency is overestimated. The regions highlighted in yellow and light orange represent conditions that closely approach null error, indicating relatively accurate efficiency. These regions span a wide range of torque and speed values, with a requests beyond 0.1

pu torque. On the other hand, the regions highlighted in red or dark orange signify areas where the efficiency is significantly underestimated. These regions align with extreme scenarios, such as peak torque at very low speed and minimal torque requests at peak speed.

Altair Flux

Table 5.6 presents the error observed in Altair Flux™ software. In the constant torque region, Altair Flux™ tends to overestimate efficiency at low torque levels. Indeed, the modeled core losses demonstrate a relatively low magnitude at very low torque requests and speeds, emphasizing their strong dependence on frequency. As the operative speed increases, there is a shift in the trend, and the software underestimates efficiency. Moreover, Altair Flux™ tends to overestimate Joule losses under high torque conditions. Within the constant power region, the core loss model in Altair Flux™ demonstrates greater precision. However, the estimation of Joule loss remains imprecise, leading to deviations in efficiency from the experimental values. At 0.786 pu speed, the software underestimates efficiency with an average error of 2.59%. The peak error of 9.78% occurs at 0.068 pu torque and maximum speed. The mean absolute percentage error for the Altair Flux™ model is 1.13%, indicating that the software accurately reflects the experimental behavior. Although the approximation exhibits a relatively high error at high speeds, the very limited error in the constant torque region helps to compensate for this imbalance.

Figure 5.4 provides a clear understanding of the efficiency assessment error in Altair Flux™ software. The green-colored region, situated in the lower part of the map, illustrates an overestimation of the efficiency. As the operating torque increases, the error gradually decreases. The yellow-coloured region indicates a nearly negligible error. The plot highlights that higher operating speeds in Altair Flux™ result in a higher error. Specifically, above 0.7 pu speed, the map demonstrates estimations with poor precision, exhibiting an error range of 3-5%.

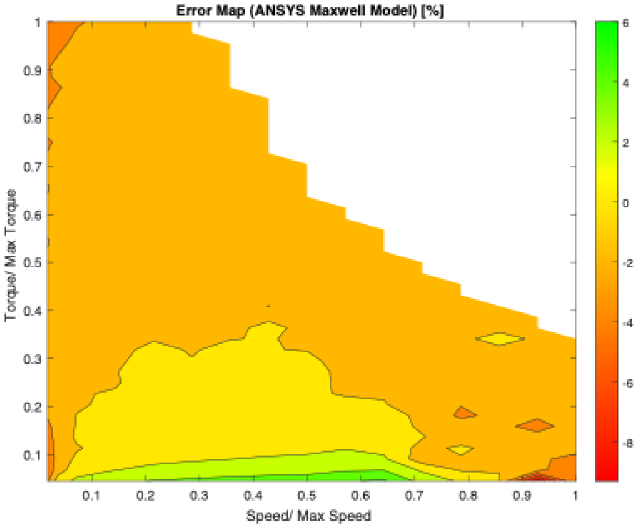

Figure 5.3: Graphic representation of the error map developed in ANSYS Maxwell

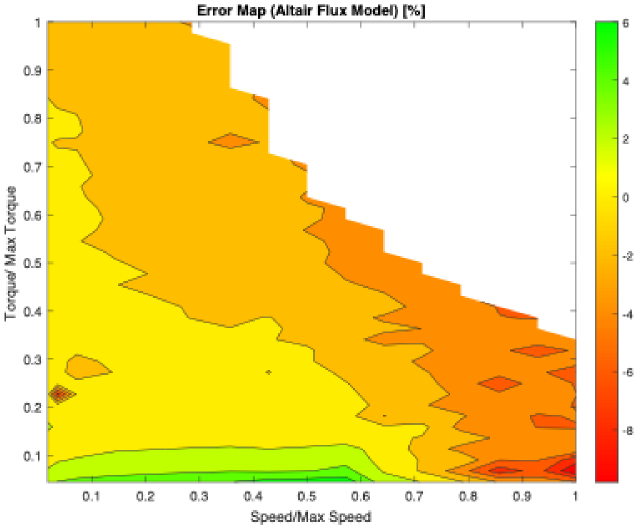

Figure 5.4: Graphic representation of the error map developed in Altair Flux

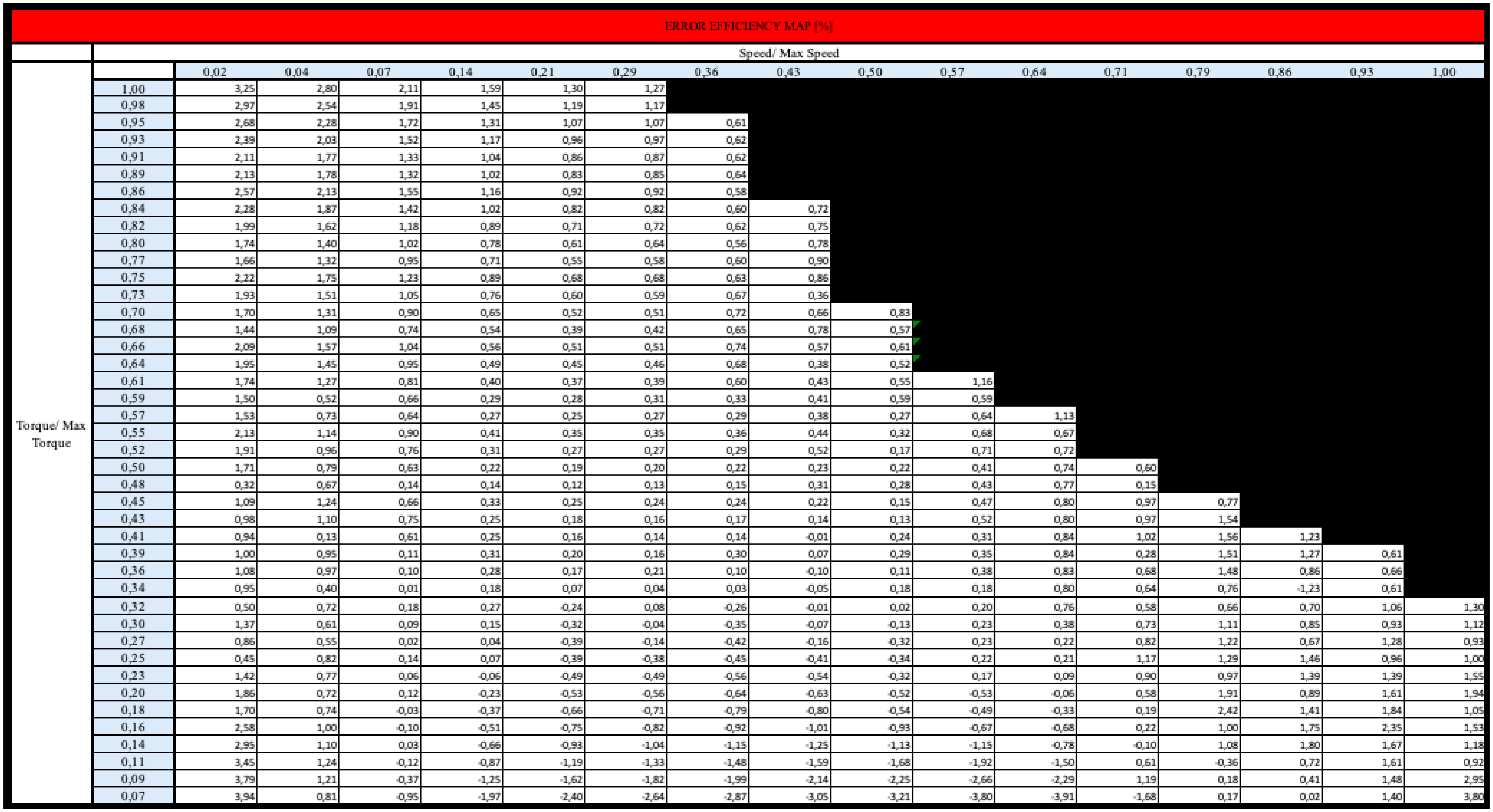

ERROR EFFICIENCY MAP [%]

		Speed/ Max Speed															
		0,02	0,04	0,07	0,14	0,21	0,29	0,36	0,43	0,50	0,57	0,64	0,71	0,79	0,86	0,93	1,00
Torque/ Max Torque	1,00	3,25	2,80	2,11	1,59	1,30	1,27										
	0,98	2,97	2,54	1,91	1,45	1,19	1,17										
	0,95	2,68	2,28	1,72	1,31	1,07	1,07	0,61									
	0,93	2,39	2,03	1,52	1,17	0,96	0,97	0,62									
	0,91	2,11	1,77	1,33	1,04	0,86	0,87	0,62									
	0,89	2,13	1,78	1,32	1,02	0,83	0,85	0,64									
	0,86	2,57	2,13	1,55	1,16	0,92	0,92	0,58									
	0,84	2,28	1,87	1,42	1,02	0,82	0,82	0,60	0,72								
	0,82	1,99	1,62	1,18	0,89	0,71	0,72	0,62	0,75								
	0,80	1,74	1,40	1,02	0,78	0,61	0,64	0,56	0,78								
	0,77	1,66	1,32	0,95	0,71	0,55	0,58	0,60	0,90								
	0,75	2,22	1,75	1,23	0,89	0,68	0,68	0,63	0,86								
	0,73	1,93	1,51	1,05	0,76	0,60	0,59	0,67	0,36								
	0,70	1,70	1,31	0,90	0,65	0,52	0,51	0,72	0,66	0,83							
	0,68	1,44	1,09	0,74	0,54	0,39	0,42	0,65	0,78	0,57							
	0,66	2,09	1,57	1,04	0,56	0,51	0,51	0,74	0,57	0,61							
	0,64	1,95	1,45	0,95	0,49	0,45	0,46	0,68	0,38	0,52							
	0,61	1,74	1,27	0,81	0,40	0,37	0,39	0,60	0,43	0,55	1,16						
	0,59	1,50	0,52	0,66	0,29	0,28	0,31	0,33	0,41	0,59	0,59						
	0,57	1,53	0,73	0,64	0,27	0,25	0,27	0,29	0,38	0,27	0,64	1,13					
	0,55	2,13	1,14	0,90	0,41	0,35	0,35	0,36	0,44	0,32	0,68	0,67					
	0,52	1,91	0,96	0,76	0,31	0,27	0,27	0,29	0,52	0,17	0,71	0,72					
	0,50	1,71	0,79	0,63	0,22	0,19	0,20	0,22	0,23	0,22	0,41	0,74	0,60				
	0,48	0,32	0,67	0,14	0,14	0,12	0,13	0,15	0,31	0,28	0,43	0,77	0,15				
	0,45	1,09	1,24	0,66	0,33	0,25	0,24	0,24	0,22	0,15	0,47	0,80	0,97	0,77			
	0,43	0,98	1,10	0,75	0,25	0,18	0,16	0,17	0,14	0,13	0,52	0,80	0,97	1,54			
	0,41	0,94	0,13	0,61	0,25	0,16	0,14	0,14	-0,01	0,24	0,31	0,84	1,02	1,56	1,23		
	0,39	1,00	0,95	0,11	0,31	0,20	0,16	0,30	0,07	0,29	0,35	0,84	0,28	1,51	1,27	0,61	
	0,36	1,08	0,97	0,10	0,28	0,17	0,21	0,10	-0,10	0,11	0,38	0,83	0,68	1,48	0,86	0,66	
	0,34	0,95	0,40	0,01	0,18	0,07	0,04	0,03	-0,05	0,18	0,18	0,80	0,64	0,76	-1,23	0,61	
	0,32	0,50	0,72	0,18	0,27	-0,24	0,08	-0,26	-0,01	0,02	0,20	0,76	0,58	0,66	0,70	1,06	1,30
	0,30	1,37	0,61	0,09	0,15	-0,32	-0,04	-0,35	-0,07	-0,13	0,23	0,38	0,73	1,11	0,85	0,93	1,12
	0,27	0,86	0,55	0,02	0,04	-0,39	-0,14	-0,42	-0,16	-0,32	0,23	0,22	0,82	1,22	0,67	1,28	0,93
	0,25	0,45	0,82	0,14	0,07	-0,39	-0,38	-0,45	-0,41	-0,34	0,22	0,21	1,17	1,29	1,46	0,96	1,00
	0,23	1,42	0,77	0,06	-0,06	-0,49	-0,49	-0,56	-0,54	-0,32	0,17	0,09	0,90	0,97	1,39	1,39	1,55
	0,20	1,86	0,72	0,12	-0,23	-0,53	-0,56	-0,64	-0,63	-0,52	-0,53	-0,06	0,58	1,91	0,89	1,61	1,94
	0,18	1,70	0,74	-0,03	-0,37	-0,66	-0,71	-0,79	-0,80	-0,54	-0,49	-0,33	0,19	2,42	1,41	1,84	1,05
	0,16	2,58	1,00	-0,10	-0,51	-0,75	-0,82	-0,92	-1,01	-0,93	-0,67	-0,68	0,22	1,00	1,75	2,35	1,53
	0,14	2,95	1,10	0,03	-0,66	-0,93	-1,04	-1,15	-1,25	-1,13	-1,15	-0,78	-0,10	1,08	1,80	1,67	1,18
	0,11	3,45	1,24	-0,12	-0,87	-1,19	-1,33	-1,48	-1,59	-1,68	-1,92	-1,50	0,61	-0,36	0,72	1,61	0,92
	0,09	3,79	1,21	-0,37	-1,25	-1,62	-1,82	-1,99	-2,14	-2,25	-2,66	-2,29	1,19	0,18	0,41	1,48	2,95
	0,07	3,94	0,81	-0,95	-1,97	-2,40	-2,64	-2,87	-3,05	-3,21	-3,80	-3,91	-1,68	0,17	0,02	1,40	3,80

Table 5.5: Difference between the experimental efficiency map and the efficiency map developed using ANSYS Maxwell™

ERROR EFFICIENCY MAP [%]

	Speed/ Max Speed															
Torque/ Max Torque	0,02	0,04	0,07	0,14	0,21	0,29	0,36	0,43	0,50	0,57	0,64	0,71	0,79	0,86	0,93	1,00
1,00	1,48	1,51	0,90	1,73	1,89	2,04										
0,98	1,19	1,26	1,03	1,58	1,77	1,93										
0,95	0,90	1,01	0,85	1,44	1,64	1,81	1,62									
0,93	0,61	0,77	0,67	1,30	1,52	1,70	1,50									
0,91	0,31	0,52	0,49	1,16	1,40	1,58	1,49									
0,89	0,36	0,55	0,49	1,14	1,37	1,55	1,64									
0,86	1,48	0,95	0,74	1,30	1,48	1,64	1,66									
0,84	-0,03	0,22	0,25	1,15	1,35	1,52	1,67	2,23								
0,82	-0,33	-0,02	0,07	1,01	1,22	1,39	1,70	2,00								
0,80	-0,60	-0,24	-0,08	0,87	1,10	1,28	1,08	1,84								
0,77	-0,68	-0,31	-0,15	0,80	1,03	1,20	1,76	1,98								
0,75	-0,10	0,13	0,12	0,98	1,16	1,31	2,96	1,68								
0,73	-0,42	-0,13	-0,06	0,86	1,03	1,18	1,15	1,67								
0,70	-0,69	-0,34	-0,21	0,70	0,90	1,06	1,21	1,53	2,25							
0,68	-0,99	-0,58	-0,38	0,55	0,77	0,94	1,08	1,38	1,85							
0,66	-0,32	-0,09	-0,09	0,72	0,89	1,02	1,15	1,37	1,83							
0,64	-0,51	-0,24	-0,20	0,62	0,79	0,93	1,06	1,12	2,20	-91,32						
0,61	-0,78	-0,45	-0,35	0,30	0,52	0,82	0,94	1,23	1,81	2,24						
0,59	-1,09	-0,68	-0,52	0,23	0,37	0,69	0,82	1,12	1,60	2,66						
0,57	-1,11	-0,71	-0,29	0,28	0,46	0,61	0,77	1,12	2,10	2,61	3,14					
0,55	-0,55	-0,32	-0,05	0,41	0,54	0,67	0,78	1,00	1,57	2,55	2,03					
0,52	-0,87	-0,56	-0,23	0,08	0,27	0,55	0,67	1,34	1,66	2,23	2,99					
0,50	-0,57	-0,37	-0,40	-0,05	0,15	0,43	0,55	0,51	1,62	2,46	2,95	3,22				
0,48	-1,45	-0,99	-0,55	-0,18	0,03	0,30	0,42	0,57	1,25	2,15	2,34	2,76				
0,45	-0,66	-0,46	-0,49	-0,01	0,14	0,27	0,38	0,36	0,77	1,87	2,24	2,42	3,58			
0,43	-0,97	-0,70	-0,42	-0,16	0,01	0,14	0,25	0,39	0,78	1,81	1,91	2,60	3,87			
0,41	-0,93	-0,70	-0,46	-0,23	-0,09	0,03	0,13	0,34	0,76	1,49	1,10	2,67	2,91	4,12		
0,39	-0,62	-0,51	-0,38	-0,21	-0,09	0,01	0,10	-0,03	0,31	1,23	2,30	2,52	3,03	3,95	4,13	
0,36	-0,70	-0,59	-0,46	-0,30	-0,19	-0,09	-0,01	-0,17	0,31	1,16	1,51	2,02	2,83	2,88	3,37	
0,34	-1,08	-0,86	-0,66	-0,46	-0,34	-0,25	-0,18	-0,06	0,23	1,15	2,89	2,17	2,57	3,07	2,77	3,79
0,32	-0,48	-0,50	-0,47	-0,42	-0,33	-0,28	-0,21	-0,24	-0,15	0,65	1,12	1,70	2,83	3,52	5,19	3,67
0,30	-0,87	-0,87	0,76	-0,60	-0,51	-0,44	-0,39	-0,20	-0,22	0,96	1,38	2,23	3,04	3,10	3,32	2,69
0,27	-1,31	-1,00	1,31	-0,11	-0,62	-0,59	-0,54	0,04	-0,77	0,39	1,17	1,87	2,63	3,11	3,37	6,02
0,25	-0,77	-0,79	-0,73	-0,71	-0,65	-0,77	-0,72	-0,38	-0,79	-0,09	1,02	1,59	2,64	5,72	2,80	4,13
0,23	-0,91	6,97	-0,17	-0,84	-0,80	-0,91	-0,89	-0,51	-0,83	-0,22	0,42	1,17	2,35	3,55	2,94	3,98
0,20	-0,53	-0,75	-0,27	-0,87	-0,86	-0,97	-0,96	-0,66	-1,07	-0,94	0,59	1,83	2,93	3,23	3,25	4,10
0,18	-1,79	-1,57	-0,51	-1,02	-1,03	-1,15	-1,15	-0,76	-1,10	-0,75	2,04	1,13	1,75	3,40	4,15	3,91
0,16	-2,15	-1,85	-0,86	-1,32	-1,33	-1,35	-1,37	-1,08	-1,54	-1,62	-0,32	-0,53	2,66	2,73	4,08	4,07
0,14	-1,67	-1,78	-1,03	-1,49	-1,53	-1,57	-1,61	-1,42	-1,73	-1,06	-0,45	0,15	0,81	2,39	3,13	3,53
0,11	-1,48	-1,68	-1,52	-1,91	-1,98	-2,05	-2,11	-2,01	-2,07	-2,72	-1,08	0,64	2,67	2,00	3,39	2,51
0,09	-1,14	-1,85	-2,12	-2,33	-2,48	-2,59	-2,71	-2,95	-3,09	-3,30	-1,32	0,16	0,33	3,98	3,88	7,23
0,07	-2,23	-2,67	-2,98	-3,28	-3,51	-3,69	-3,89	-3,75	-3,87	-4,65	-1,80	0,28	3,14	7,13	5,25	9,78

Table 5.6: Difference between the experimental efficiency map and the efficiency map developed using Altair Flux™

Chapter 6

Conclusions and Future Work

In the analysis of electric motors, one of the most crucial parameters to evaluate is efficiency. It quantifies the amount of energy required by the motor to produce a certain torque relative to the energy retrieved from the battery. Efficiency directly impacts the battery's state of charge, state of health, and the overall range that the motor can cover without requiring recharging. Developing a virtual model that closely resembles the actual motor behavior is essential for various reasons:

1. To investigate the effects of model changes in a virtual environment.
2. Analyzing and mitigating the motor losses.
3. To evaluate motor performance during the design stage.

6.1 Conclusions

This section will highlight the key discoveries of this research activity:

Joule Loss

The developed model demonstrates accurate tracking of the expected trend of joule loss, which represents the most significant contribution among all the losses and increases with higher current magnitudes and frequencies.

In contrast to the existing literature, a temperature and frequency-dependent stator resistance model has been developed to account for the skin and proximity effect in evaluating motor losses. This approach eliminates the need to modify the winding material in the two software tools based on operating temperature and avoids the inclusion of additional corrective coefficients to account for AC effects. Since the proposed model operates in post-processing, it relies on appropriate input data obtained from the simulation. Consequently, the accuracy of the two software tools in evaluating the current generated in the stator windings becomes a crucial aspect to consider.

Core Loss

The fixed coefficient model adopted in the two software tools presents a limitation compared to alternative approaches, such as a variable coefficient model. The variable coefficient model allows the coefficients of each loss component (hysteresis, eddy current, and excess) to vary with operating torque and frequency, offering greater adaptability. However, this research activity did not have sufficient input data to develop the variable coefficient model, and the Altair Flux software did not support this approach.

Nonetheless, the fixed coefficient model remains a valid alternative. The model's precision has been sacrificed at low speeds to ensure reliability in conditions where core losses are higher. Indeed, as the core loss becomes more significant, the model accurately predicts them. The model has been implemented in both software environments by adding the appropriate coefficients, and the accuracy of the results turned out to be dependent on how well the software predicts the distribution of the magnetic field at specific operating frequencies.

Mechanical Loss

To account for the mechanical losses, a post-processing approach was adopted, where the simulations were computed under ideal conditions. A third order polynomial expression, dependent on speed, was utilized to capture various mechanical effects, including ventilation, internal friction, and external friction. While this approach is not innovative compared to the existing literature, it demonstrates excellent accuracy in aligning with the experimental trend used to develop the model.

Although the mechanical loss contributes relatively less compared to Joule and core losses, it cannot be disregarded, particularly at higher operating speeds. By considering all the mechanical effects collectively, the model effectively captures the overall mechanical loss behavior in the motor.

Efficiency Assessment

For each operating point, the predicted losses are combined with the output power to evaluate the motor efficiency. The most significant error for both software tools is observed at low operating speeds, primarily due to the underestimation of core losses resulting from the adopted model. The evaluation of experimental efficiency becomes more challenging in boundary scenarios, such as peak speed combined with peak torque or peak torque combined with minimum speed. Similar considerations can be extended to the software environment, although both software tools are still capable of replicating the experimental behavior with reasonable accuracy.

The models employed in both software tools demonstrate a satisfactory level of precision in assessing motor efficiency, yielding comparable results. This can be attributed to the adoption of identical models. In the case of mechanical loss, since it is considered in post-processing and is not influenced by simulation results, the exact same results are considered. For core losses, similar outcomes are achieved in the two software tools, indicating the fidelity of the model and the similarity in the magnetic field distribution developed by the software. However, differences are more apparent in the evaluation of joule loss. Although the frequency-dependent model is considered in post-processing and is therefore the same for both software tools, discrepancies arise from the differing modeling of frequency effects, particularly in the distribution of current. It is noteworthy that the magnitude of current input is identical for both software tools. As the disparity between the two software tools becomes more pronounced at higher operating speeds, it can be concluded that they model frequency effects differently. Upon analyzing the error map and the mean absolute percentage error, it is reasonable to assert that ANSYS Maxwell™ provides a more accurate representation of Joule loss and better aligns with the trend of experimental results.

6.1.1 Software Performance Comparison

The electric motor simulation was performed using two software tools, ANSYS Maxwell™ and Altair Flux™, in order to assess their performance and compare their capabilities. Each software was analyzed individually throughout the different phases of motor modeling, followed by a comparison between the two.

In ANSYS Maxwell™, the motor modeling process was found to be intuitive, allowing for easy association of design components and materials. Electric and magnetic properties could be defined, taking into account temperature effects and spatial anisotropy. Multiple meshing options were available, with the ability to improve the basic meshing using length-based meshing or surface approximation.

The software provided visual tools for analyzing meshing precision. The modified Bertotti method is available to predict the core losses. Mechanical losses are modeled with experimentally-obtained coefficients. In the post-processing phase, various plots could be generated, including current density, magnetic field, electromagnetic torque, and losses breakdown.

In Altair Flux™, modifying the motor geometry is straightforward, with guidelines provided during the model development process. Material association allowed for consideration of spatial anisotropy and temperature dependence, as well as the use of non-linear models. Thermal properties can be added for thermal coupling analysis, and material behavior could be described using parametric equations. Meshing options included second-order meshing and the ability to focus on specific regions of the model. The software provided information on meshing accuracy. Joule losses can be modeled for both solid and stranded conductors, while iron losses were modeled with adjustable coefficients and exponents. Mechanical losses can be described with friction and ventilation coefficients.

In comparing the two software tools, it was found that the implementation of the motor model was identical in both. Altair Flux offered the advantage of modeling more complex material properties, such as spatial conductivity and temperature dependency. The meshing procedure played a critical role, with a higher number of meshes resulting in slower simulation times, and overly dense meshing did not significantly improve result accuracy. ANSYS Maxwell™, despite using a less dense mesh, provided more accurate results. The largest errors were observed at low torque demands, which is a common challenge even in experimental tests. Both software tools demonstrated exceptional accuracy in evaluating efficiency and similar results, as they employed equivalent loss models.

In conclusion, both ANSYS Maxwell™ and Altair Flux™ proved to be capable software tools for simulating electric motors. The choice between them may depend on specific requirements, such as the need for complex material modeling.

6.1.2 Conclusion Summary

The main findings of this research work are summarized in the following list:

- The Joule loss model accurately tracks the expected trend of the loss, and the temperature and frequency stator resistance model effectively simulates AC effects on windings.
- The core loss model prioritizes the precision at high operating speeds, i.e. above the base speed, where core losses are more significant. On the other hand, the prediction at low operating speed is not accurate.

- The mechanical loss is modeled using a third-order polynomial, which is a well-established approach in the literature. Nevertheless, it aligns well with the experimental trend.
- The two software tools show the most significant error in estimating efficiency at low operating speeds due to the underestimation of core losses resulting from the adopted model. However, beyond this region, both tools provide very accurate efficiency predictions.
- Altair Flux model employs a higher density of meshes, but this does not noticeably improve loss evaluation. However, it significantly increases computational time, making simulations much more time-consuming compared to ANSYS Maxwell. For instance at high operating speeds, simulations that take a few minutes in ANSYS Maxwell can take up to 30 minutes in Altair Flux.
- Based on the error map and MAPE analysis, ANSYS Maxwell has proven to be the most accurate of the two software in simulating the electromagnetic behavior of the electric motor.
- The post-processing MATLAB™ algorithm surpasses the efficiency map evaluation precision offered by the built-in tools of the two software packages. Furthermore, the code can be adapted to different motor models, provided that the data to build the loss models are available.

6.2 Future Work

Although this research activity focused on applying the losses estimation method to interior permanent magnet synchronous motors, the same technique could be extended to other electric machine topologies. It would be intriguing to apply and validate the model on different motors, such as surface-mounted permanent magnet and induction motors. The virtual environment only requires a two-dimensional replication of the motor, while in MATLAB, the coefficients can be adjusted to accommodate the new motor under test, allowing for post-processing of the results and the development of efficiency and loss maps.

The accuracy of the presented models justifies their implementation for estimating losses and efficiency in electric motors. However, adjustments can be made to the models if a greater amount of data is available. One potential improvement would be to consider a variable coefficient model for the core losses, which would retain information about the core losses at low angular speeds. Another possibility is to directly implement the mechanical friction coefficients in the software, enabling visualization of their effects on motor performance, such as torque distribution. A future research direction could involve investigating the coupling between electromagnetic behavior and thermal behavior in the motor. This would entail studying the dissipation of losses within the motor and understanding how it affects temperature distribution and overall thermal performance.

Bibliography

[1] Ehsani, M., Gao, Y., and Gay, S. (2003, November). Characterization of electric motor drives for traction applications. In IECON'03. 29th Annual Conference of the IEEE Industrial Electronics Society (IEEE Cat. No. 03CH37468) (Vol. 1, pp. 891-896). IEEE.

[2] Zhu, Z. Q., and Chan, C. C. (2008, September). Electrical machine topologies and technologies for electric, hybrid, and fuel cell vehicles. In 2008 IEEE vehicle power and propulsion conference (pp. 1-6). IEEE.

[3] Kim, S. H. (2017). Electric motor control: DC, AC, and BLDC motors. Elsevier.

[4] Pellegrino, G., Vagati, A., Guglielmi, P., and Boazzo, B. (2011). Performance comparison between surface-mounted and interior PM motor drives for electric vehicle application. IEEE Transactions on Industrial Electronics, 59(2), 803-811.

[5] Ma, B. M., and Narasimhan, K. S. V. L. (1986). NdFeB magnets with higher Curie temperature. IEEE transactions on magnetics, 22(5), 916-918.

[6] Liu, X., Chen, H., Zhao, J., and Belahcen, A. (2016). Research on the performances and parameters of interior PMSM used for electric vehicles. IEEE Transactions on Industrial Electronics, 63(6), 3533-3545.

[7] Soong, W. L., and Ertugrul, N. (2002). Field-weakening performance of interior permanent-magnet motors. IEEE Transactions on Industry Applications, 38(5), 1251-1258.

[8] Alberti, L., Barcaro, M., Bianchi, N., Bolognani, S., Bon, D., Castiello, M., Faggion, A., Fornasiero, E., & Sgarbossa, L. (2011). Interior permanent magnet integrated starter-alternator. *COMPEL-The International Journal for Computation and Mathematics in Electrical and Electronic Engineering*, 30(1), 117–136.

[9] Kamiya, M. (2006). Development of traction drive motors for the Toyota hybrid system. *IEEJ Transactions on Industry Applications*, 126(4), 473–479.

[10] Pang, Y., Zhu, Z., Howe, D., Iwasaki, S., Deodhar, R., & Pride, A. (2007). Comparative study of flux-switching and interior permanent magnet machines. *2007 International Conference on Electrical Machines and Systems (ICEMS)*, 757–762.

[11] Azar, Z., Zhu, Z., & Ombach, G. (2012). Influence of electric loading and magnetic saturation on cogging torque, back-EMF and torque ripple of PM machines. *IEEE Transactions on Magnetics*, 48(10), 2650–2658.

[12] Bertotti, Giorgio. (1985). Physical interpretation of eddy current losses in ferromagnetic materials. I. Theoretical considerations. *Journal of Applied Physics*, 57(6), 2110–2117.

[13] Ferrari, S., Ragazzo, P., Dilevrano, G., & Pellegrino, G. (2021). Flux-Map based FEA evaluation of synchronous machine efficiency maps. *2021 IEEE Workshop on Electrical Machines Design, Control and Diagnosis (WEMDCD)*, 76–81.

[14] Yuan, L., Zhu, Z., & Lin, X. (2015). Improved eddy current loss modeling considering electric loading and magnetic saturation for permanent magnet machines. *IEEE Transactions on Magnetics*, 51(11), 1–10.

[15] STOYANOV, L., LAZAROV, V., ZARKOV, Z., & POPOV, E. (2019). Influence of skin effect on stator windings resistance of AC machines for electric drives. *2019 16th Conference on Electrical Machines, Drives and Power Systems (ELMA)*, 1–6.

[16] Ferreira, J. A. (1994). Improved analytical modeling of conductive losses in magnetic components. *IEEE Transactions on Power Electronics*, 9(1), 127–131.

[17] Mellor, P. H., Wrobel, R., & McNeill, N. (2006). Investigation of proximity losses in a high-speed brushless permanent magnet motor. *Conference Record of the 2006 IEEE Industry Applications Conference Forty-First IAS Annual Meeting*, 3, 1514–1518.

[18] Boubaker, N., Matt, D., Enrici, P., Nierlich, F., & Durand, G. (2018). Measurements of iron loss in PMSM stator cores based on CoFe and SiFe lamination sheets and stemmed from different manufacturing processes. *IEEE Transactions on Magnetics*, 55(1), 1–9.

[19] Ibrahim, M., & Pillay, P. (2013). Core Loss Prediction in Electrical Machine Laminations Considering Skin Effect and Minor Hysteresis Loops. *IEEE Transactions on Industry Applications*, 49(5), 2061–2068.

[20] Jacobs, S., Hectors, D., Henrotte, F., Hafner, M., Gracia, M. H., Hameyer, K., & Goes, P. (2009). Magnetic material optimization for hybrid vehicle PMSM drives. *World Electric Vehicle Journal*, 3(4), 875–883.

[21] Yin, X., Jiang, Y., & Howe, D. (2012). Performance analysis of flux-switching permanent magnet machines with different stator slot combinations. *IEEE Transactions on Energy Conversion*, 27(3), 724–731.

[22] Zhang, H., Guo, H., & Luo, H. (2020). Prediction of iron losses in the stator core of electrical machines using a novel simplified energy loss model. *IEEE Transactions on Industrial Electronics*, 68(1), 390–400.

[23] Zhou, Z., Liu, J., Wang, J., Liu, Y., Yang, X., Yang, Y., & Gao, J. (2017). Core losses prediction of electrical machines under nonsinusoidal power supply conditions. *IEEE Transactions on Power Electronics*, 32(3), 2447–2458.

[24] Bertotti, G. (1984). A general statistical approach to the problem of eddy current losses. *Journal of Magnetism and Magnetic Materials*, 41(1), 253–260.

[25] Ioniţă, V., Petrescu, L., Cazacu, E., Pătroi, E.-A., & Manta, E. (2017). Improved prediction of hysteresis losses in electrical machine cores. *2017 International Conference on Modern Power Systems (MPS)*, 1–4.

[26] Petrescu, L.-G., Petrescu, M.-C., Cazacu, E., & Constantinescu, C.-D. (2021). Estimation of Energy Losses in Nanocrystalline FINEMET Alloys Working at High Frequency. *Materials*, 14(24), 7745.

[27] Zhou, Z., Liu, J., Wang, J., & Zhao, Y. (2016). Fast prediction method for iron loss in electrical machines based on a combination of vector fitting and stochastic modeling. *IEEE Transactions on Power Electronics*, 31(11), 7772–7785.

[28] Xue, S., Feng, J., Guo, S., Peng, J., Chu, W., & Zhu, Z. (2017). A new iron loss model for temperature dependencies of hysteresis and eddy current losses in electrical machines. *IEEE Transactions on Magnetics*, 54(1), 1–10.

[29] Parthasaradhy, P., & Ranganayakulu, S. (2014). Hysteresis and eddy current losses of magnetic material by Epstein frame method - novel approach. *The International Journal of Engineering and Science*, 85–93.

[30] Amar, M., & Protat, F. (1994). A simple method for the estimation of power losses in silicon iron sheets under alternating pulse voltage excitation. *IEEE Transactions on Magnetics*, 30(2), 942–944.

[31] Ma, L., Sanada, M., Morimoto, S., & Takeda, Y. (2003). Prediction of iron loss in rotating machines with rotational loss included. *IEEE Transactions on Magnetics*, 39(4), 2036–2041.

[32] Moses, A. (1992). Importance of rotational losses in rotating machines and transformers. *Journal of Materials Engineering and Performance*, 1(2), 235–244.

[33] Zhu, Z., Chen, L., & Lin, X. (2010). Modeling and measurement of core loss in iron core synchronous machines using space phasor. *IEEE Transactions on Energy Conversion*, 25(4), 1124–1131.

[34] Tekgun, B., Sozer, Y., & Tsukerman, I. (2016). Measurement of core losses in electrical steel in the saturation region under DC bias conditions. *IEEE Transactions on Industry Applications*, 53(1), 88–96.

[35] Boglietti, A., Cavagnino, A., Lazzari, M., & Pastorelli, M. (2001). Effects of punch process on the magnetic and energetic properties of soft magnetic material. *IEMDC 2001. IEEE International Electric Machines and Drives Conference (Cat. No. 01EX485)*, 396–399.

[36] Bramerdorfer, G. (2020). Effect of the manufacturing impact on the optimal electric machine design and performance. *IEEE Transactions on Energy Conversion*, 35(4), 1935–1943.

[37] Elfgen, S., Steentjes, S., Böhmer, S., Franck, D., & Hameyer, K. (2017). Influences of material degradation due to laser cutting on the operating behavior of PMSM using a continuous local material model. *IEEE Transactions on Industry Applications*, 53(3), 1978–1984.

[38] Wang, H., Zhang, Y., & Li, S. (2016). Laser welding of laminated electrical steels. *Journal of Materials Processing Technology*, 230, 99–108.

[39] Yamazaki, K., & Fukushima, W. (2015). Loss analysis of induction motors by considering shrink fitting of stator core. *2015 IEEE International Electric Machines & Drives Conference (IEMDC)*, 322–328.

[40] Andreas Krings, "Iron Losses in Electrical Machines – Influence of Material Properties, Manufacturing Processes and Inverter Operation", PhD thesis, KTH School of Electrical Engineering, Stockholm, 2014

[41] Kumar, R., Kumar, P., Kanekawa, T., & Oishi, K. (2020). Stray loss model for induction motors with using equivalent circuit parameters. *IEEE Transactions on Energy Conversion*, 35(2), 1036–1045.

[42] Schützhold, J., & Hofmann, W. (2013). Analysis of the temperature dependence of losses in electrical machines. *2013 IEEE Energy Conversion Congress and Exposition*, 3159–3165.

[43] Dellinger, J. H. (1911). The temperature coefficient of resistance of copper (No. 147). US Department of Commerce and Labor, Bureau of Standards.

[44] Ansys® Maxwell, Help System, Maxwell 3D Guide, ANSYS, Inc.

[45] Mahmoudi, A., Soong, W. L., Pellegrino, G., & Armando, E. (2015). Efficiency maps of electrical machines. *2015 IEEE Energy Conversion Congress and Exposition (ECCE)*, 2791–2799.

[46] Motors, P. I. (n.d.). IEEE Test Procedure for Polyphase Induction Motors Having Liquid in the Magnetic Gap.

[47] Williamson, S., Lukic, M., & Emadi, A. (2006). Comprehensive drivetrain efficiency analysis of hybrid electric and fuel cell vehicles based on motor-controller efficiency modeling. *IEEE Transactions on Power Electronics*, 21(3), 730–740.

[48] Bojoi, R., Armando, E., Pastorelli, M., & Lang, K. (2016). Efficiency and loss mapping of AC motors using advanced testing tools. *2016 XXII International Conference on Electrical Machines (ICEM)*, 1043–1049.

[49] Dlala, E., Solveson, M., Stanton, S., Tang, Z., Christini, M., Ong, R., & Peaslee, B. (2013). Efficiency map simulations for an interior PM motor with experimental comparison and investigation of magnet size reduction. *2013 International Electric Machines & Drives Conference*, 23–29.

[50] The MathWorks Inc. (2022). MATLAB version: 9.13.0 (R2022b), Natick, Massachusetts: The MathWorks Inc. https://www.mathworks.com

[51] Y. S. Jeon, H. S. Mok, G. H. Choe, D. K. Kim and J. S. Ryu, "A new simulation model of BLDC motor with real back EMF waveform," COMPEL 2000. 7th Workshop on Computers in Power Electronics. Proceedings (Cat. No.00TH8535), Blacksburg, VA, USA, 2000, pp. 217-220, doi: 10.1109/CIPE.2000.904719.

Vita Auctoris

NAME: Giovanni Ricciardi
PLACE OF BIRTH: Avellino, Italy
YEAR OF BIRTH: 1999
EDUCATION: Liceo delle Scienze Applicate, IISS F. De Sanctis, Sant'Angelo dei Lombardi, AV, Italia, 2013-2018
Politecnico di Torino, B.Sc. in Automotive Engineering, Turin, Italy, 2018-2021
Politecnico di Torino, M.Sc. in Automotive Engineering, Turin, Italy, 2021-2023
University of Windsor, M.A.Sc. in Automotive Engineering, Windsor, ON, 2021-2023